A 140 GHz Gyro-amplifier using a Confocal Waveguide: Theory and Experimental Results

by

Alexander Visotsky Soane

M.S. (EECS), Massachusetts Institute of Technology (2011)
B.S. (Physics), Massachusetts Institute of Technology (2009)

Submitted to the Department of Electrical Engineering and Computer Science
in partial fulfillment of the requirements for the degree of

Doctor of Philosophy

at the

MASSACHUSETTS INSTITUTE OF TECHNOLOGY

September 2017

Author .....
Department of Electrical Engineering and Computer Science
August 8, 2017

Certified by .....
Richard J. Temkin
Senior Research Scientist, Department of Physics
Thesis Supervisor

Accepted by .....
Professor Leslie A. Kolodziejski
Chair, Committee on Graduate Students
Department of Electrical Engineering and Computer Science

A 140 GHz Gyro-amplifier using a Confocal Waveguide: Theory and Experimental Results

by

Alexander Visotsky Soane

Submitted to the Department of Electrical Engineering and Computer Science
on August 8, 2017, in partial fulfillment of the
requirements for the degree of
Doctor of Philosophy

Abstract

This thesis reports on the theory, design, and experimental investigation of a gyrotron travelling-wave-tube (TWT) amplifier at 140 GHz. The gyro-TWT uses the HE_{06} mode of a confocal geometry as its operating mode. The linear and nonlinear theory of the confocal waveguide is presented, along with a quasi-optical approach for describing the modes of a confocal waveguide. Both the equations of motion and the mode excitation equation are derived in detail. A beamlet code is introduced as a tool for calculating the linear and nonlinear gain of the azimuthally asymmetric confocal modes that interact with the electron beam with an annular distribution of electron guiding centers. This code has been successfully benchmarked against the code MAGY for azimuthally symmetric cases, and extends the capabilities of nonlinear gyroamplifier theory to configurations that lack azimuthal symmetry. The gyro-TWT experimental setup is presented in detail. Quasi-optical mode converters were designed, fabricated, and tested, ultimately achieving a coupling of -3 dB into the HE_{06} mode. The source of competing, parasitic oscillations was identified and addressed by the addition of dielectric loading attached to the side of the open geometry of the confocal waveguide. The improvements to the gyro-TWT system allowed for zero-drive stable operation at currents up to 3 A. The design frequency of 140.0 GHz was successfully amplified with 35 dB circuit gain and a -3 dB bandwidth of 1.2 GHz from a 48 kV, 3 A electron beam with a beam pitch factor of 0.64 and a perpendicular velocity spread of 6%. The gyro-TWT produced 550 W at 140.0 GHz under the same operating conditions. During experimental testing, the pulse length used was 2 microseconds. The performance of the confocal gyro-TWT suggests that it may be a candidate for application to Dynamic Nuclear Polarization (DNP) Nuclear Magnetic Resonance (NMR) experiments.

Thesis Supervisor: Richard J. Temkin
Title: Senior Research Scientist, Department of Physics

Acknowledgments

This thesis is the culmination of over a decade of being part of MIT. I could never have known that when I first arrived at MIT as an eager freshman that I would end my student career with such a wonderful group of supportive friends and family. Many people are owed significant gratitude for their direct and indirect contributions to the work that went into this thesis. It may be impossible to properly list everyone, but I am confident that everyone will recognise my appreciation for all that they have done.

I would like to thank my thesis adviser Dr. Richard J. Temkin, who in 2011 took a chance on offering me a position in his research group. Throughout the years of my PhD, Rick has been a source of guidance and support that leads me to owe a deep debt of gratitude. Likewise, I thank Dr. Michael Shapiro for the many hours of answering any questions I have had, scientific or cultural, in English, Russian, and French. To Ivan Mastovsky I am indebted for the countless times he has helped me in lab with the experiment. This includes the countless times he has fixed and saved me from mistakes I made in lab, so I would like to say dakuj vam to Ivan. Dr. Sudheer Jawla also spent many hours working with me on the gyroamplifier, offering his advice and help whenever possible.

My labmates and colleagues are also due a special thanks. They brought me much joy when things were frustrating in lab, and sober reflection when I became excited. To my current labmates, Julian Picard, Samuel Schaub, Haoran Xu, XueYing Lu, and Hannah Hoffmann, a big thank you. The camaraderie we shared was one of the highlights of my workday. I wish all of you success and happiness in your ventures after graduate school, and I am confident that you will do well. Likewise, to Dr. Jacob Stephens and Dr. Guy Rosenzweig, thank you and the best of luck.

None of this would have been possible without the timeless devotion and love of my family. For their advice I am always grateful. Drs. David and Zoya Soane instilled in me a love of science and the values of hard work and education. My father was ever-present in discussions of science and technology; my mother - for being my

friend and caregiver over many years of my life. They have both devoted themselves to their two children, myself and my brother Nicholas, and have shown us a boundless world. For a small family you are all that I need. Nicky - you are my best friend and brother, and you have always and will always be the sobering influence in my life. We have shared many rare moments that resonate with us as brothers. They are the foundation for the friendship that will continue for many, many years. I know that you will have success in what you do. I also want to mention my grandmother, Galina Arkadeevna Martynenko, for the fond memories from childhood. Her life story is an inspiration for me to this day. I love my family dearly, and I am looking forward to having them in the next chapter of my life. Спасибо за все!

One of the amazing gifts that I found over the course of my MIT career is the friendship of many people. Conner Galloway, best friend from my undergraduate years, kept my passion for physics alive throughout the many psets and late nights. Dr. Jason Hummelt, gym buddy and essential friend, with whom I passed many evenings in friendship after work - to him I owe much of my sanity throughout the concluding months of the PhD. Dr. Matt Schram, Dr. William Uspal, and Dr. Chris Leon, the original "no shame" crew, what can I say other than to emphasize that your friendship, and the adventures we got into, comprised so much of what made MIT memorable. You three formed the cadre of my friends in graduate school, and we share many memories and exploits. I thank you especially for everything that you have done as friends over the years. You were always there for me. And to all of my friends who are not listed by name, you know who you are and that I value our friendship.

There is a host of others that I need to acknowledge. In their own ways they have each been an influence on my life in graduate school. Without them, my life would be devoid of passion and interest. Throughout graduate school, I made many friends by pursuing my principal hobby at MIT, intramural ice hockey. The EECS Killer Volts, Ashdown, and Physics Annihilation Operator teams, and my fellow teammates, were an important part of my life at MIT. Notably, thank you Eva Polyzoeva for passing me the puck, yelling on the ice, and the many wonderful trips to the Garden. Thank

you to everyone on the teams for always skating out with me. Coaches David Hunter and Chad Martinovich are also directly responsible for teaching me how to skate and how to be a hockey player. The machinists at the Central Machine Shop at MIT were always helpful. They tolerated my mistakes and helped me to become a better engineer. I owe them thanks for building the various structures that were the core of my PhD, as well as the many conversations in the shop. Andrew Gallant, Scott Spence, and Michael Abruzzese suffered through my CAD mistakes the most (and to everyone there a big thank you). John Michaels, who drove a lunch truck for over thirty years, always greeted me on Albany street and became a source of familiarity that helped when work was difficult. Mme. Culot, pour m'enseignait le francais. Vous me faire un don qui restera avec moi toujours. Dr. Richard Bristol, for many years of advice, and for having the confidence in me when I was rudderless - thank you.

And to Katie Anne Scheier. You brought me happiness throughout the final time of my graduate career. I thank her for the love that we found and for what we learn from each other. She is always my partner in crime as well as a source of strength. I am so lucky to have met you. And we ended up in this quadrant of the galaxy.

Alexander Soane
August 8, 2017
Cambridge, MA.

to my grandmother,

Галина Аркадеевна Мартыненко (Galina Arkadeevna Martynenko)

and to my brother,

Nicholas (Nicky) Visotsky Soane

Капля камень точит

"Quant au courage morale, il avait trouvé fort rare, disait-il, celui de deux heures après minuit; c'est-à-dire le courage de l'improviste."

- Napoleon Bonaparte

Taken from *Watership Down* by Richard Adams.

Contents

List of Figures

List of Tables

Chapter 1

Introduction

Gyrotrons as a class of vacuum electron device have had a rich history in published literature. Cornerstone books include the published works of Nusinovich [1], Kartikeyan et al. [2], Gilmour [3], Tsimring [4], and Edgecombe [5]. This thesis describes experimental and theoretical research on a gyrotron travelling wave tube amplifier operating at 140 GHz. The major themes of this document will be: the theory of gyrotrons, challenges encountered when operating at high frequency microwaves and the design of this experiment, and the results of experimental study.

1.1 Motivation

The advent of radio was a transformative invention in not only cultural and political history but also in the history of engineering. The ability to communicate over vast distances essentially instantaneously was only the gateway into a scientific revolution that now encompasses such wide-ranging fields as fundamental chemistry to astronomy. Acquiring mastery over the electromagnetic spectrum has been a scientific and engineering challenge. To date, humans can control and use frequencies that vary from AM radio (1 MHz) to X-rays (order of petahertz). Despite this extent of frequencies, one specific band has until recently lacked a practical source. Known as the "Terahertz Gap", the spectrum in the range of 0.1 to 1 THz has historically been without high-power sources. Gyrotrons are one class of devices that is capable of

producing high power in this frequency regime.

This thesis will focus on a pulsed amplifier that operates at 140 GHz, well into what is known as the "millimeter wave" regime (MMW). The MMW band occupies frequencies between about 30 GHz to 300 GHz, and is named thusly because the wavelengths at these frequencies are on the order of a millimeter. As a subset of the "Terahertz Gap", the MMW band is important for numerous applications that span several important sectors. Communication and defense are two such sectors that benefit directly from high-power sources in the MMW band. The frequency band and available high-power sources are both features that have applications in these sectors. In particular, wideband, high-power MMW systems are used for satellite communication [6, 7]. Another space-related role taken on by MMW sources is at the MIT Lincoln Labs Haystack radar in the form of an upgrade to a 94 GHz system [8].

MMW sources have found important roles in the security and defense sectors. The ability to scan for contraband (such as weapons) rapidly is a much-needed innovative technology. Several examples, such as the now-common body scanners at airports, have been designed [9, 10]. MMW sources have even been applied for detecting chemical and biological elements [11]. High-power MMW sources have also found applications in industrial processes [12]. Another sector that benefits directly from MMW systems is the field of fundamental chemistry research, and this field is the ideal end-user for the 140 GHz gyro-amplifier experiment. Interestingly, MMW sources are a crucial technology in advancing nuclear magnetic spectroscopy (NMR) systems.

1.2 MMW Sources for use with Dynamic Nuclear Polarization NMR

NMR has been a standard tool in chemistry research and has been known as a physical process for decades [13, 14]. NMR's spectroscopic approach allows for detailed analysis in a diverse array of chemistry research, but is limited by its reliance on the small magnetic moments of nuclear spins. It has been known since 1953 [15] that

instead of using the spin polarization of nuclei that the NMR technique could be expanded to utilize the greater polarization difference in the electron spins. Known as dynamic nuclear polarization (DNP), this quantum mechanical process transfers the electron spin polarization onto the nuclear spin polarization [16], thus enhancing the sensitivity of traditional NMR techniques. In theory, DNP is capable of achieving an enhancement factor equal to the ratio of the paramagnetic resonances of an electron and proton, $\gamma_e/\gamma_p \sim 660$ (for example for the case of a hydrogen atom). Experimentally, an enhancement of ~ 100 was first demonstrated by Carver and Slichter [17]. Contemporary DNP NMR experiments have achieved similar enhancement values, as seen in Fig. 1-1, albeit at very different operating parameters. The immediate benefit of such an enhancement is the reduction of data acquisition time, one of the principle downsides to traditional NMR. Such an enhancement leads to a significant reduction in the time and cost of operating NMR instruments.

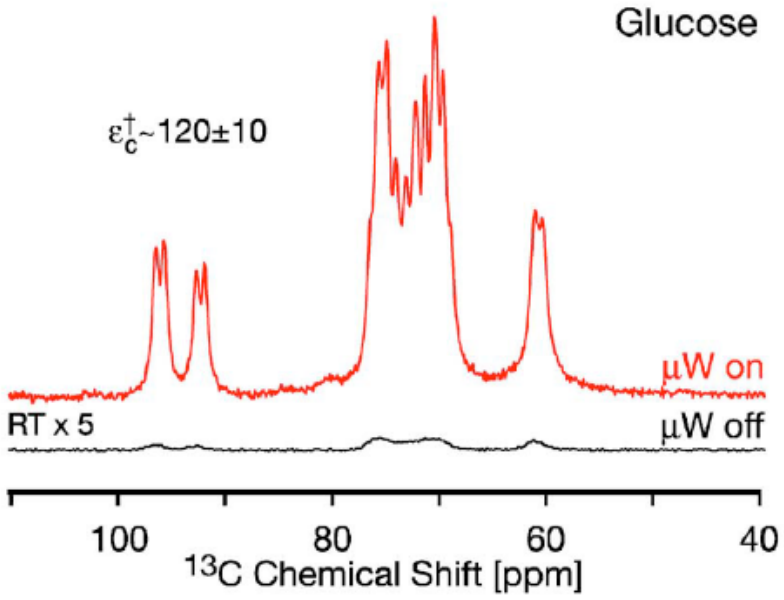

Figure 1-1: An example of a DNP-enhanced NMR signal, showing an enhancement of about 120 with MMW power applied to the glucose sample. Figure adapted from [18].

Because the paramagnetic ratio is 660, this shows that the frequency of radiation needed to excite electrons for a DNP NMR experiment is 660 times greater than the corresponding proton frequency (in a given magnetic field). For example, in the

original experiment performed by Carver and Slichter [17], they used a 30.3 gauss static magnetic field, which gave a proton paramagnetic resonance of 50-kc/sec and an electron paramagnetic resonance of 84 Mc/sec. In 1953, a variety of microwave sources could fulfill the role of providing the radiation needed to excite electrons at the necessary frequencies given the state of magnet technology. However, there is a distinct advantage at operating NMR analysis at high magnetic fields, where the spectral resolution is correspondingly better [19]. As stronger and stronger magnetic fields are used, the electron paramagnetic frequency is likewise scaled to higher values (the frequency scales linearly with the static magnetic field, B_0). Consequently, much of DNP NMR was originally limited by the availability of sources as the required frequency entered the THz regime. Commercially-available technology began to hit an upper frequency limit when a 3.4 T magnet was used in a DNP NMR experiment, which required 94 GHz radiation to excite the electron population [20]. In addition to achieving the correct frequency, it is desirable to produce high power, as experimental factors affect how efficiently the electron population is polarized. DNP NMR as a field needed a class of device capable of high power output in the THz regime.

Just as magnet technology unlocked NMR at high magnetic fields, gyrotrons as a vacuum electron device class allowed DNP to continue to be applied to these high-field NMR experiments. The Francis Bitter Magnet Laboratory at MIT pioneered the use of gyrotrons for DNP NMR in 1993 [21]. The advent of MMW sources has opened the technique of DNP for application to modern NMR. DNP is used to enhance the sensitivity of NMR spectra by a factor in the range of 100, and since 1993 several new DNP NMR experiments have been conducted. At MIT alone, gyrotrons have been used for DNP NMR experiments at 250 GHz [22], 330 GHz [23], and 460 GHz [24, 25]. A design for a 527 GHz gyrotron has been completed at MIT [26]. Other gyrotron-based DNP instrumentation and experiments are being conducted internationally at various frequencies, such as 198 GHz [27], 263 GHz [28], and 395 GHz [29]. These listed experiments are based on gyrotron oscillators with a continuous wave (CW) output. There is an interest in developing gyro-amplifiers for pulsed-DNP NMR experiments [30, 31, 32, 33, 34, 35].

Pulsed DNP NMR is different from CW DNP NMR. CW DNP experiments, as mentioned, have been widely successful. There is, however, a limitation on the polarization enhancement, ϵ, in which $\epsilon \sim 1/f$, where f is the Larmor frequency and is linear with the magnetic field [36, 37]. This means that as NMR reaches for higher magnetic fields, the enhancement is adversely affected. The search for an alternative to CW DNP was actually performed early in the history of DNP. In 1958, Bloembergen and Sorokin demonstrated a pulsed DNP NMR experiment [38]. Recent developments have evolved the pulsed DNP technique to include solid samples (as opposed to only liquid samples) [33]. A key advancement in using pulsed DNP is the realization that the inverse scaling with the magnetic field can be avoided if the problem is transformed into the nuclear rotating frame [39]. In order to exploit this fact, a certain pulse train of microwave power is needed [40]. In order to form a specific pulse train, a phase-controlled source at the proper frequency is required. Gyrotron amplifiers fit this role when used in conjunction with a solid state driver, where you can manipulate the phase as necessary.

1.3 The State of MMW Sources

As discussed, gyrotrons are desirable for application to DNP NMR research. They are, however, not the only MMW source available. Microwave sources can be generally classed as either being a solid state device or a vacuum electronic device. The technology of each branch differs widely from the other's, and consequently the applications are also diverse. In general, vacuum electronic devices are based on the interaction of an electron beam with an operating RF mode of a waveguide, whereas solid state devices are based on transistor technology. Owing to the requirements to accelerate and confine an electron beam, a typical vacuum electronic device is much larger than any solid state source; however, the benefits of higher power are much more readily attainable with this class of devices. This fact can be seen in Fig. 1-2, which shows how various available MMW sources perform in terms of power versus frequency [41].

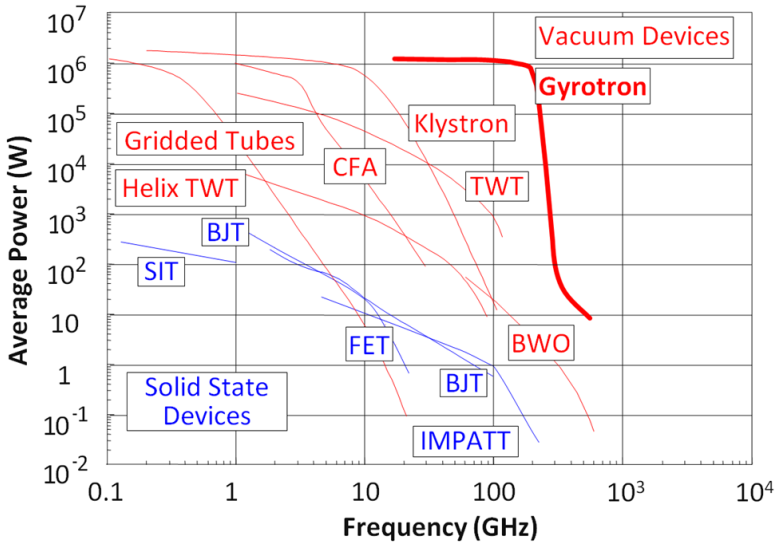

Figure 1-2: The frontiers of power versus frequency for both solid state and vacuum electronic devices. Gyrotrons show promise for direct application to DNP.

As shown in the plotted power versus frequency, all devices suffer in performance as the “Terahertz Gap" is pushed; however, gyrotrons remain as one of the promising sources even as frequencies are extended towards 1 THz.

1.4 Gyrotrons as Oscillators and Amplifiers

Gyrotrons as a class of vacuum electronic devices have been known since the 1950s. The fundamental theory that describes the gyrotron interaction, namely the electron cyclotron resonance instability, was proposed by several researchers - R. Twiss [42], J. Schneider [43], and A. Gaponov [44]. Essentially, a gyrotron device relies on the interaction between a slightly relativistic beam and an eigenmode of a waveguide cavity. The electrons, which are gyrating in a confining magnetic field, lose some of their perpendicular velocity in transferring energy to the eigenmode of the cavity. This is the origin of the prefix “gyro" in the term gyrotrons. It is important to note that the cyclotron instability relies on the electron beam being relativistic, although the actual Lorentz factor γ may still be close to 1.

In the most basic configuration, a gyrotron device consists of an electron gun, a (superconducting) magnet, and an interaction cavity. Due to the fact that the energy

extracted from the beam is only from its perpendicular velocity, it is desirable to have a source of electrons with a high perpendicular velocity component. A magnetron injection gun (MIG) is capable of producing such an electron beam [45]. A MIG style electron gun has a cylindrically-symmetric, sloped emitting surface, which injects an annular electron beam with a velocity vector that has both axial, v_z, and perpendicular, $v_\perp$, components. The ratio of perpendicular to axial velocity components is typically referred to as the pitch factor, $\alpha = v_\perp/v_z$. The guiding center radius, R_g, which is the radius of the annular electron beam, is significantly larger than the Larmor radius, r_c. This annular beam is launched towards the center of a strong magnet, whose field is chosen such that the cyclotron resonance frequency for the electrons is close to that of the desired microwave frequency. Because the electron beam is entering into a region of increasing magnetic field (at the magnet's center), the beam itself undergoes adiabatic compression. Thus, the perpendicular energy of the electrons increases as the orbital momentum increases. Once in the flat top of the magnetic field the beam interacts with the eigenmode of the microwave waveguide, transferring some of its perpendicular energy to the electromagnetic field through stimulated emission provided that the frequency of the microwaves is close to a harmonic of the frequency of the electron gyration. The beam then continues through the magnetic field and is deposited on an anode, known as a collector. The microwaves, in turn, are coupled out of the system. This can be achieved through various techniques, but one common and desirable approach is to convert the microwave mode into a Gaussian mode. A Gaussian mode can be easily coupled out of any system with a transmission line. A simplified, cartoon view of a gyrotron is presented in Fig. 1-3.

Gyrotrons are fast wave devices, called so because the phase velocity of the microwave within the waveguide is faster than the speed of light. This is in contrast to slow wave devices, which rely on the design of the waveguide to keep the phase velocity of the wave below that of the speed of light. It has been recognized for some time that slow wave devices can be used to generate microwave radiation [46]. When the phase velocity is below that of light, it is possible for a waveguide mode to interact

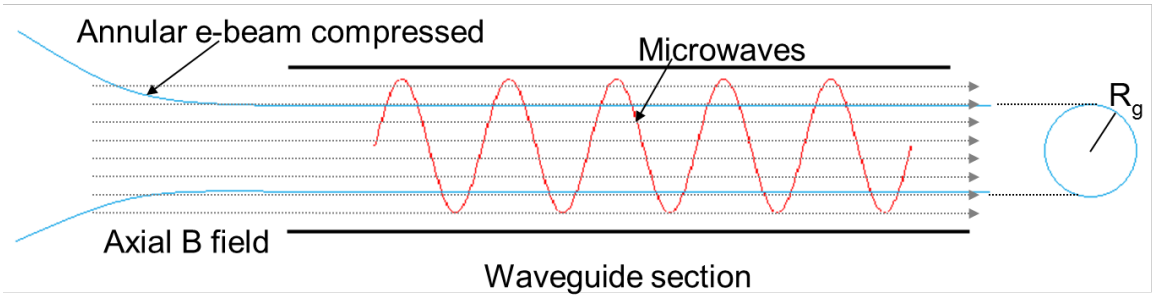

Figure 1-3: A cartoon schematic of the fundamental gyrotron device. The guiding radius of the electrons, shown here as R_g, highlights that the beam produced by a MIG gun is annular in structure.

with an electron beam via its parallel velocity component. Although highly successful as MMW sources, the slow wave designs inherently rely on mechanical dimensions that are typically less than the wavelength of interest. Consequently, as the frequency of MMW sources is pushed higher into the THz regime, both the manufacturing tolerances of these wavelength-scale mechanical features as well as concerns about heat dissipation become important. The mechanical scaling for fast wave devices follows the same inverse relationship with frequency as for slow wave devices; however, in the case of fast wave devices, operation in higher order modes is readily possible. This allows the mechanical dimension of fast wave devices to remain on the order of several wavelengths, which at near-THz frequencies helps with mechanical tolerances and manufacturing. The ability to operate in a higher order mode is one of the cornerstones behind the confocal waveguide that will be discussed in this thesis.

Gyrotrons can be harnessed to operate in two ways: as an oscillator and as an amplifier. In both cases, the overall setup for a gyro-device is the same. Both require a confining magnetic field (often supported by a superconducting magnet), an electron gun, and a system for supporting and transporting microwaves. Schematically, a cartoon view of a gyrotron oscillator and amplifier is shown in Fig. 1.4.

A gyrotron oscillator, Fig. 1.4a, is typically based around a short cavity with a resonant mode that supports the desired microwave frequency. A method of extracting the RF power is included, which often consists of a mode converter. Similar to the oscillator is the gyrotron amplifier, Fig. 1.4b, and is also known as a gyro-travelling wave

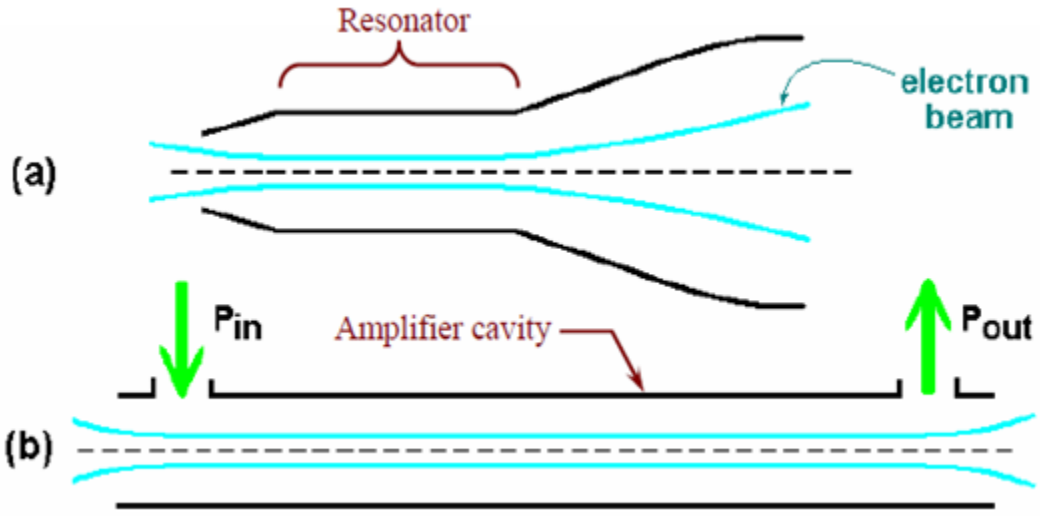

Figure 1-4: Depiction of a gyrotron oscillator (a) and amplifier (b). Both systems use the CRM instability, and are capable of theoretically high power and gain performance, making them desirable for a number of applications.

tube (gyro-TWT). Gyro-TWTs are fast-wave devices that, like oscillators, rely on the cyclotron resonance maser instability and thus are capable of high gain performance. As previously mentioned, in the MMW regime, both oscillators and gyro-TWTs feature an overmoded waveguide design. This is due to the fact that at the millimeter scale (140 GHz $\sim$ 2 mm wavelength), fundamental waveguide is necessarily on the order of a millimeter. Because of restrictions on electron guns and the danger of beam interception and ohmic heating on waveguide walls, it is infeasible to design gyrotrons to operate with fundamental waveguide when MMWs are desired. To overcome this restriction, the approach taken in this experiment is that of choosing a specific geometry for operation as an overmoded waveguide. This geometry, known as a confocal configuration, has the important benefit of mode selectivity, and will be discussed in a further section.

1.5 Gyrotron Oscillators

Gyrotron oscillators are an excellent source of high-power MMW radiation [47]. As seen in Fig. 1.4a, the heart of the gyrotron oscillator is a cavity that features a

downtaper at the gun-end (to protect from backward waves) and an uptaper at the output end (to direct the MMW power). These cavities are overmoded by design. The overmoded cavity allows gyrotron oscillators to operate in a higher-order mode, which frees the mechanical dimensions and tolerances to be multiple wavelengths in scale. This has a couple of key advantages, namely that the large physical dimensions help with reducing ohmic loss and allow the use of a higher-current, larger diameter electron beam [48]. The total beam current in a gyrotron oscillator can be significant, and this fact lends itself to making the gyrotron oscillator a source of high output power [49]. The fact that gyrotron oscillators operate in a highly overmoded cavity means that, for efficient transmission outside of the vacuum tube, the gyrotron oscillator design typically features an internal mode converter. These mode converters are often quasi-optical and designed to convert the high-order TE_{mn} operating mode into a Gaussian beam [50, 51]. A typical gyrotron oscillator device schematic is shown in Fig. 1.5, and features the principle components of a gyrotron oscillator. These components are the MIG electron gun, the main (often superconducting) magnet, the operating cavity where the MMW are generated, the quasi-optical mode converter, and the collector. All of these components are housed within a vacuum tube.

In tracing the history of gyrotron oscillator development, we see an initial drive to produce high-power, CW sources [52]. Pulsed operation of gyrotrons was investigated as well, and over the decades this technology has advanced considerably [53, 54, 55, 56]. Because of their reliability and high output power, gyrotron oscillators found a natural application to plasma heating [57]. The frequency stability of gyrotron oscillators actually poses as one of their principle limitations - gyrotron oscillators are not readily frequency-tunable. This limitation has been addressed by step-tunable schemes [58] as well as utilizing gyrotron cavities that are capable of operation at more than one frequency (at different operating points) [59, 60]. The development of high-power gyrotrons will continue for many different applications. Perhaps one day gyrotrons will be an integral part of a successful fusion experiment [61].

1.6 Gyrotron Amplifiers

The cyclotron maser instability may also be utilized in an amplifying capacity. Gyrotron amplifiers, also known as gyrotron travelling wave tubes (gyro-TWTs) are the second application of the gyrotron interaction. The gyro-TWT setup was first demonstrated decades ago [62, 63, 64]. In principle, gyro-TWTs are capable of high gain over a broad bandwidth [65]. Indeed, a gyro-TWT operating at 35 GHz demonstrated a performance of 70 dB of gain during an experiment conducted at the National Tsing Hua University in the Republic of China [66]. The frequency of 35 GHz allowed this experiment to be designed for the fundamental mode TE_{11} of a waveguide. This fact becomes important when higher frequencies are considered, because in order to maintain the use of a fundamental mode, the corresponding waveguide dimension needs to be reduced. Using a fundamental mode is preferred, as it eliminates the possibility of mode competition. Unfortunately, its use is not feasible at 140 GHz, so an alternative approach is taken. The alternative approach in question is the use of an overmoded interaction structure. In this scheme, the frequency of operation is confined by a higher-order mode of a waveguide, which allows the waveguide dimension to remain relatively large. The choice of waveguide mode is one of the crucial design elements, and the quasi-optical confocal waveguide will be the subject of this thesis, but many choices exist. These include helically corrugated waveguide [67] and a photonic bandgap waveguide [30, 68].

Regardless of interaction waveguide choice, the fact that the waveguide is overmoded means that mode competition has been introduced to the gyro-TWT system. Research that looked at ways to circumvent mode competition discovered that adding lossy material helps mitigate this problem [69, 70, 71, 72, 73]. Another possibility for mode suppression is the addition of a sheath helix [74]. The method of mode suppression chosen for experiment described in this thesis is to use a diffractive loss from a quasi-optical, open waveguide geometry, known as a confocal geometry. Designed to be quasi-optical and overmoded, the confocal geometry has been demonstrated successfully in a gyrotron oscillator [75]. The properties of the confocal waveguide

will be discussed in detail in a subsequent chapter.

As amplifiers, gyro-TWTs require MMW sources. The source used in this experiment is a solid state driver, capable of phase controlled pulses. Power is transmitted through a corrugated waveguide into the vacuum tube, where it is focused into the operating mode of the confocal waveguide. As such, the overall alignment and design of this gyro-TWT experiment is crucial to the system's success as an amplifier. A detailed discussion of the gyro-TWT setup will be described in a future chapter. Figure 1.6 shows a cutaway schematic of the gyro-TWT system as used for the experiments described in this thesis. The principle components, which are ubiquitous for gyro-TWT setups, are labelled. It is seen that gyro-TWTs are complex assemblies, each individual component having to work in concert in order to achieve successful and high gain. One of the main aims of this thesis is to motivate this point and showcase some of the design strategies that can be taken in order to navigate all of the parameters necessary when engineering a gyro-TWT system.

1.7 Thesis Outline

This thesis is a compendium of work that relates to the development of a gyro-TWT using a confocal waveguide as an interaction circuit. In the following chapters I will discuss the theoretical framework for the gyro-TWT (including a presentation of the gyrotron equations and the quasi-optical confocal waveguide), numerical simulations developed for the confocal gyro-TWT, and the experimental setup and results from this investigation. This is organized into the following chapters. In chapters 2, 3, and 4, I discuss the confocal waveguide, derive the gyro-equations that govern the gyro-TWT interaction, and explore a new numerical tool that can be used to simulate the gyro-TWT interaction for a confocal waveguide mode. In chapter 5, I present the experimental setup of the confocal gyro-TWT experiment and discuss the principle components in detail. The experimental results are shown and discussed. The thesis concludes with chapter 6.

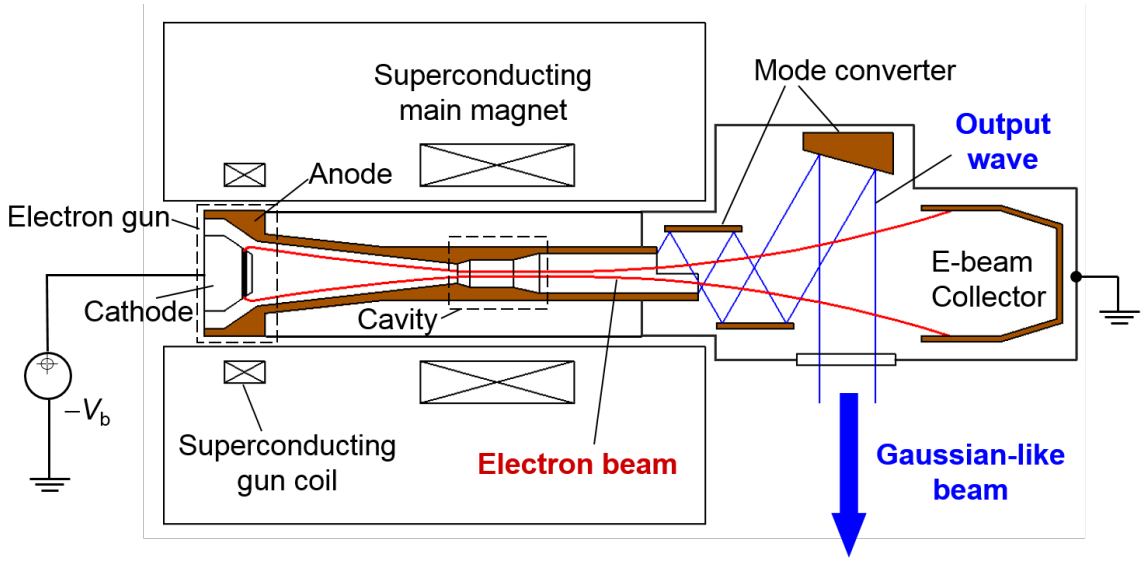

Figure 1-5: The design schematic of a typical gyrotron oscillator is shown. The principle components are the electron gun, main magnet, cavity within the vacuum tube, the quasi-optical mode converter, and the grounding collector for the electron beam.

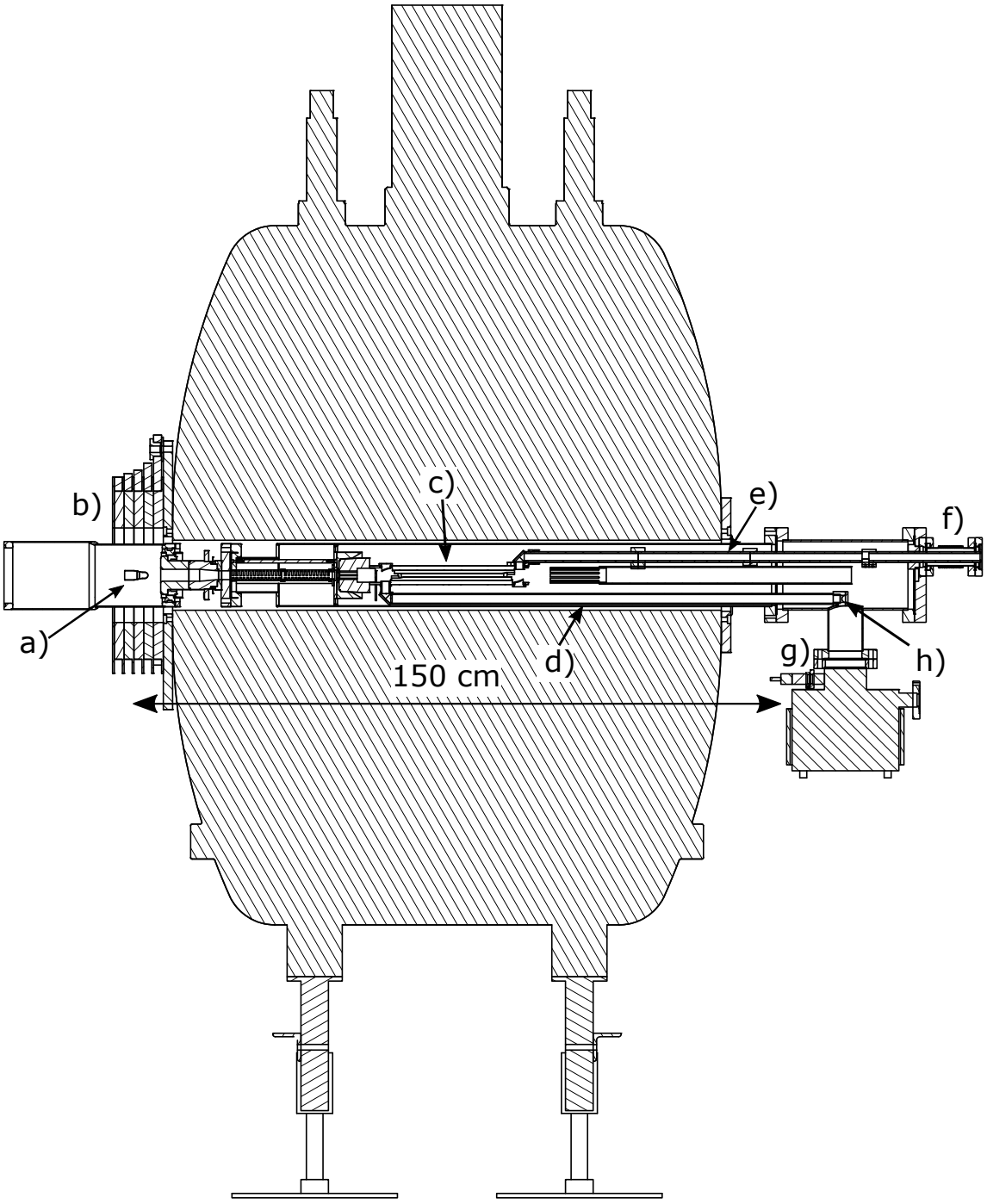

Figure 1-6: A cross section schematic of the confocal system setup is shown, in which a) location of electron gun, b) the gun coil magnet, c) confocal circuit, d) input waveguide, e) output waveguide, f) the output window, g) the ion pump, and h) the location of the input window (axis normal to the page). The tube is housed inside of a superconducting magnet.

Chapter 2

Confocal Waveguide

In this chapter we explore the confocal geometry as a choice for the interaction waveguide. As has been previously discussed, the gyro-TWT works by transferring energy from the perpendicular velocity component of a travelling electron beam to RF fields of a millimeter wave mode of a waveguide. The electron beam is confined by a magnetic field, typically from a superconducting magnet, which also sets the cyclotron frequency.

The annular electron beam propagates collinearly with the electromagnetic mode of the interaction waveguide, during which time the energy is transferred between the beam and the millimeter wave. The guiding center radius of the electron beam is augmented by the magnetic field strength. In typical operation, the local magnetic field at the emission surface at the cathode is less than the main flat top magnetic field at the interaction region (within the waveguide). Adiabatic compression of the electron beam follows the general behavior that

$$B_0 R_{go}^2 = B(z) R_g(z)^2 \tag{2.1}$$

where B_0, R_{go} are the magnetic field and guiding center at the cathode and $B(z)$, $R_g(z)$ are the magnetic field and guiding center as a function of axial position z. This compression ratio, that is the ratio of $B_0/B(z)$, is used to form a final guiding center radius within the waveguide that allows the annular beam to overlap with peaks in

the electric field of the operating spatial mode.

Essentially, the choice of what spatial mode to use to support the millimeter wave power is not very restrictive - provided that the spatial mode has peaks where the electron beam overlaps is a sufficient constraint. One common waveguide that supports the operating mode is a simple cylindrical pipe. To avoid the possibility of competition from unwanted frequencies in unwanted modes, it is desirable to operate at the lowest-order mode of a waveguide. This option adds a mechanical constraint that the waveguide dimension is on the order of the RF wavelength. As the gyrotron frequency increases, the corresponding wavelength inversely decreases. In order to maintain the lowest-order mode as the operating mode, the waveguide dimensions must also scale toward decreasing sizes. Likewise, the guiding center radius of the annular beam is decreased. Eventually, this trend towards smaller physical dimensions will lead to space charge effects in the electron beam and ohmic losses on the waveguide itself. Therefore, it is advantageous for the gyrotron amplifier to operate in a higher order mode of the interaction circuit in order to minimize these effects.

Operation in a higher order mode allows us to lift the constraint of reduced mechanical dimensions. Although helpful for reducing space charge effects and ohmic losses, functioning as an overmoded waveguide introduces the possibility of parasitic competition from unwanted modes. Avoiding parasitic oscillations is an important design consideration when engineering overmoded interaction circuits. Contemporary gyro-amplifiers take advantage of a variety of design approaches to address the issue of mode competition. Lossy-wall gyro-amplifiers have been designed and operated at 35 GHz [76, 77] and at 95 GHz [65]. An alternative design feature is a helically-corrugated interaction circuit [67, 78]. We present a confocal interaction circuit as an alternative to lossy-wall designs. Gyrotrons with confocal circuits continue to be studied intensively [79, 80, 81, 82, 75]. In this chapter the confocal waveguide is introduced as an overmoded geometry that can support 140 GHz radiation. A quasi-optical approximation of its field properties is derived and the loss rate per unit length of confocal rails is found.

2.1 Quasi-optical approximation of a confocal waveguide

2.1.1 Membrane function

We begin with a description of the confocal geometry. As seen in Fig. 2-1, the confocal geometry consists of two rails positioned such that their radius of curvature R_c, is equal to that of their separation distance, $L_\perp$ ($R_c = L_\perp$). The aperture, or total width of each mirror, is $2a$. As this geometry is not closed, the width is adjusted in order to either increase or decrease the diffractive loss of the supported HE_{mn} modes. These supported spatial modes have m variations along $\hat{x}$ and n variations along $\hat{y}$, and are uniform in $\hat{z}$. Fig. 2-1 shows the HE_{06} mode, in which there are six variations along the $\hat{y}$ direction.

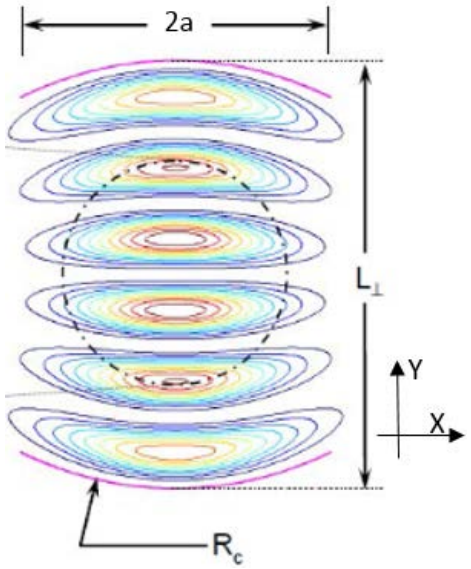

Figure 2-1: The confocal geometry including the field distribution of the HE_{06} mode, shown on a linear scale. The guiding centers of the electron beam are on the dashed annulus. Each electron has a gyroradius of $v_\perp/\omega_c$.

The HE_{06} mode is a good choice for an operating mode at 140 GHz because at this frequency, a mirror separation distance of 6.83 mm provides a cutoff of 137.2 GHz in this mode. The dispersion relation for the HE_{06} mode is plotted along with the relations for the HE_{15} and HE_{05} modes in Fig. 2-2. A more detailed discussion

of the electron gun will be presented in a subsequent chapter, but it is important to note that at the operating magnetic field the electron beam's guiding center radius is about 1.8 mm. At a rail spacing of 6.83 mm, this guiding center radius would overlap well with the second and fifth peaks of the HE_{06} mode, as shown in Fig. 2-1.

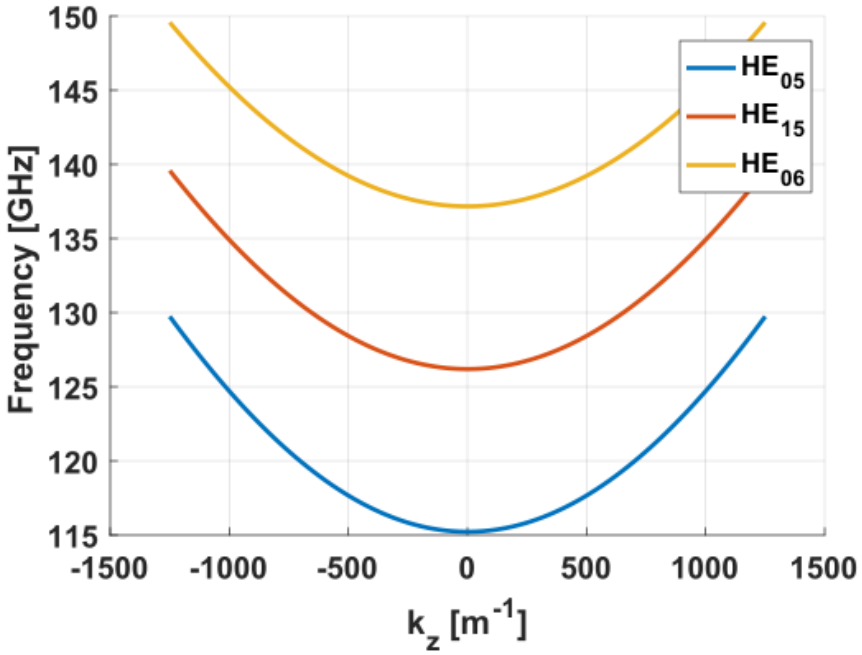

Figure 2-2: The HE_{06} operating mode's dispersion relation is plotted for a rail spacing of 6.83 mm. The two nearest lower order modes of HE_{15} and HE_{05} are plotted as well. A cutoff of 137.2 GHz for the HE_{06} mode indicates that this is an appropriate choice for an operating mode to support 140 GHz RF power.

For a closed waveguide, supported modes are described by the membrane function Ψ, which obeys the wave equation:

$$\nabla_{\perp}^2 \Psi + k_{\perp}^2 \Psi = 0 \tag{2.2}$$

in which the transverse wavenumber $k_{\perp}$ is real ($k_{\perp} = k_{\perp r}$). In consideration of the fact that the confocal waveguide is not a closed geometry, we introduce a quasi-optical approach to finding an approximate membrane function [83, 84]. The formulation for a closed geometry [1] relies on the exact solution to the wave equation in Eq. 2.2. Translational symmetry in the $\hat{z}$ component reduces the problem to two dimensions.

Additionally, we assume a solution that is based on a modified plane wave in the $\hat{y}$ direction:

$$U(x,y) = B(x,y)e^{-ik_\perp y} \tag{2.3}$$

As indicated in Eq. 2.3, we assume a wave propagating in the $\hat{y}$ direction. Variation in x is absorbed into the function $B(x,y)$, an appropriate step if assuming the paraxial approximation of $k_y = \sqrt{k_\perp^2 - k_x^2} \simeq k_\perp - \frac{k_x^2}{2k_\perp}$. Now, the wave equation Eq. 2.2 becomes

$$\frac{\partial^2 B}{\partial x^2} + \frac{\partial^2 B}{\partial y^2} - 2ik_\perp \frac{\partial B}{\partial y} = 0 \tag{2.4}$$

Since the field distribution is a modified plane wave propagating in the $\hat{y}$ direction, we can neglect $\frac{\partial^2 B}{\partial y^2}$ as small compared to the term $2ik_\perp \frac{\partial B}{\partial y}$. With this simplification, Eq. 2.4 becomes

$$\Big[\frac{\partial^2}{\partial x^2} - 2ik_\perp \frac{\partial}{\partial y}\Big] B(x,y) = 0 \tag{2.5}$$

Using the form of Eq. 2.3 for U, we provide a general solution to the membrane function Ψ as two counter-propagating waves:

$$\Psi = -iU - iU^* \tag{2.6}$$

The confocal geometry, when examined with a quasi-optical approximation, lends itself readily to a Gaussian beam solution for $B(x,y)$. Thus, U may be expressed as

$$\begin{aligned} U(x,y) = \Big(\frac{2}{\pi}\Big)^{\frac{1}{4}} \sqrt{\frac{w_0}{w(y)}} \exp\Big(-\frac{x^2}{w^2(y)}\Big) \times \\ \exp\Big(-ik_{\perp r}y - i\frac{k_{\perp r}x^2}{2R(y)} + \frac{i}{2}\arctan\frac{y}{b_o}\Big) \end{aligned} \tag{2.7}$$

where $b_o = k_{\perp r} w_0^2/2$, following the derivations in [83]. Furthermore, w and R are

$$w^2(y) = w_0^2\Big[1 + \Big(\frac{2y}{k_{\perp r} w_0^2}\Big)^2\Big] \tag{2.8}$$

$$\frac{1}{R(y)} = \frac{y}{y^2 + (k_{\perp r} w_0^2/2)^2} \tag{2.9}$$

The perpendicular wavevector component, $k_{\perp r}$, may be found by considering the boundary conditions of Eq. 2.7 under the confocal geometry. In particular, at a coordinate $(x, y) = (0, L_\perp/2)$ we know that the phase front curvature $R(y)$ needs to match the confocal mirror radius, R_c. Consequently, $k_{\perp r}$ is found to be

$$k_{\perp r} = \frac{\pi}{L_\perp}\Big(n + \frac{2m+1}{\pi} \arcsin\sqrt{\frac{L_\perp}{2R_c}}\Big) \tag{2.10}$$

Since $L_\perp = R_c$ for the confocal geometry,

$$k_{\perp r} = \frac{\pi}{L_\perp}\Big(n + \frac{m}{2} + \frac{1}{4}\Big) \tag{2.11}$$

These results are in agreement with those derived by Nakahara [85], following Goubau [86]. In this section we have derived the quasi-optical approximation of the membrane function that describes the field distribution of a confocal resonator. Because the confocal geometry is open, RF power may leak out of the sides of the waveguide. Thus, a mode HE_{mn} will, whilst propagating axially, lose power through transverse diffraction. This leads to a loss per distance that is useful for suppressing undesired (lower-order) modes that do not support the microwave field intended for amplification.

2.1.2 Diffractive losses in a confocal resonator

We follow the derivation in [84, 87] in our discussion of losses incurred by waveguide modes HE_{mn} in the confocal geometry. The wave vector $k_\perp$ is decomposed into both a real and an imaginary component, $k_{\perp r} + ik_{\perp i}$. Eq. 2.11 is the real component; a more general expression is needed:

$$k_\perp = \frac{\pi}{L_\perp}\left(n + \frac{m}{2} + \frac{1}{4} + \frac{\delta}{\pi}\right) - i\frac{\Lambda}{2L_\perp} \tag{2.12}$$

In Eq. 2.12 we have introduced a small phase shift δ as well as an imaginary component for $ik_{\perp i}$. Λ is directly related to the diffraction losses. As discussed in Section 2.1.1, the quasi-optical solution to the modes in a confocal geometry is found by superimposing propagating Gaussian waves to form a standing wave between the curved mirrors. Diffraction occurs because the transverse width of the confocal mirrors is insufficient to capture the transverse extent of the waveguide modes HE_{mn}. With each subsequent reflection, the Gaussian wave loses a fraction of its power. Schematically, modes with $m > 0$ have a broader transverse "footprint", so more readily diffract for a given confocal aperture width. This effect is shown in Fig. 2-3.

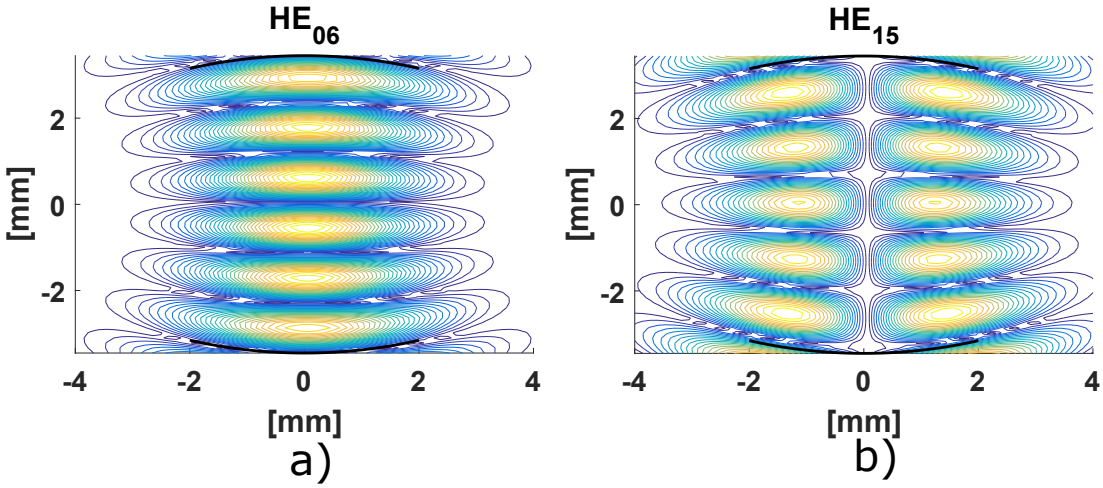

Figure 2-3: Contours of the horizontal component of the electric field distribution for the HE_{06} mode at 140 GHz (a) and HE_{15} mode at 126 GHz (b) are plotted. This field distribution is found for an aperture of $2a = 4$ [mm] and $R_c = 6.83$ [mm]. These plots are on a linear scale with yellow showing the highest field values.

Λ is written in terms of the Fresnel diffraction parameter C_F and the radial spheroidal wavefunction expressed in prolate spheroidal coordinates [84, 88] $R^{(1)}_{0,m}(\xi_1, \xi_2)$:

$$\Lambda = 2\ln\left[\sqrt{\frac{\pi}{2C_F}}\frac{1}{R^{(1)}_{0,m}(C_F, 1)}\right] \tag{2.13}$$

The Fresnel diffraction parameter is defined as $C_F = k_{\perp r}a^2/L_\perp$, where a is half

the width of the confocal mirrors. In Eq. 2.13, $R^{(1)}_{0,m}(C_F, 1)$ is a function of C_F as well as m, which specifies the transverse mode content of the HE_{mn} waveguide modes. For the first three values of m (0, 1, 2) the values of $R^{(1)}_{0,m}(C_F, 1)$ are shown in Fig. 2-4 and $\log(\Lambda)$ are shown in Fig 2-5, both as a function of C_F.

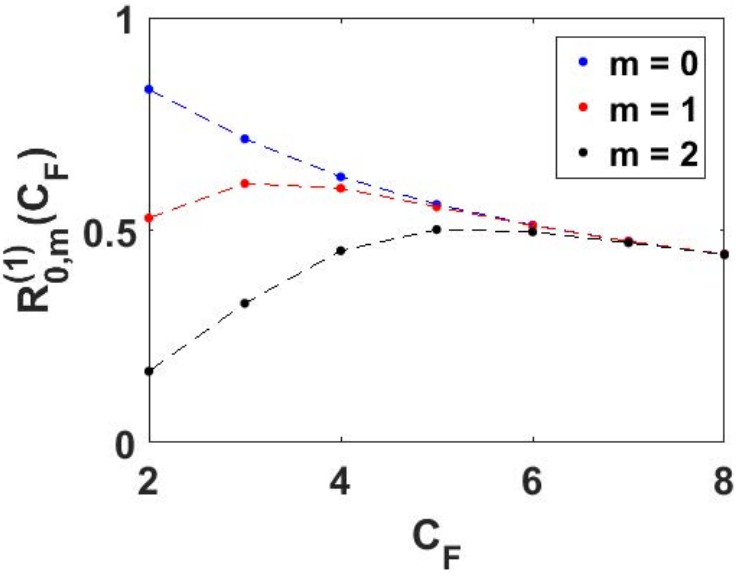

Figure 2-4: The exact values of $R^{(1)}_{0,m}(C_F, 1)$ plotted against C_F for various values of m; the lines connect calculated points.

In the wave vector component k_z, losses incurred are due to the imaginary component, k_{zi}. If we consider a *loss rate* in terms of decades per axial distance, then the loss rate is expressed as

$$\text{Loss Rate} = \frac{20}{\ln(10)} k_{zi} \tag{2.14}$$

in which

$$k_{zi} = \text{Im}\sqrt{\left(\frac{\omega}{c}\right)^2 - k_\perp^2} = -\frac{k_{\perp r} \times k_{\perp i}}{k_{zr}} \tag{2.15}$$

where $k_{zr} = \sqrt{\frac{\omega^2}{c^2} - k_{\perp r}^2}$ is assumed to be not close to 0 (i.e. the mode is not close to cutoff; $k_{zr} \gg k_{zi}$). We calculate the attenuation in decades per unit length as a function of C_F (or aperture a). Figure 2-6 shows a comparison between the

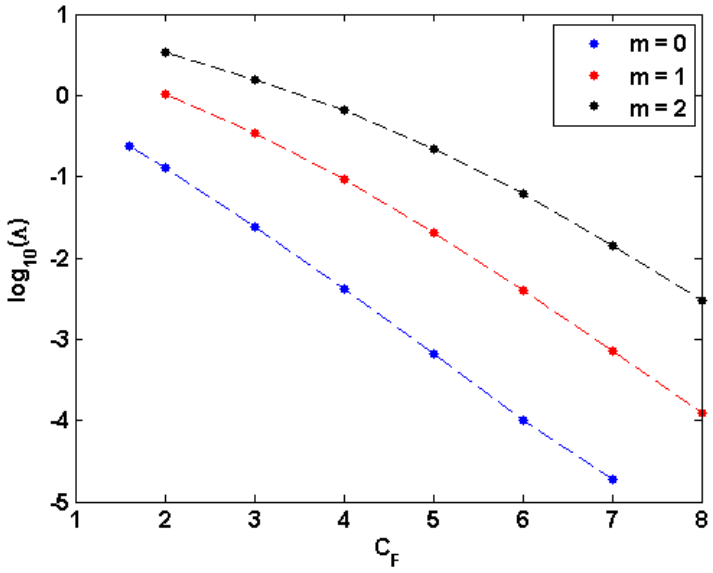

Figure 2-5: The exact values of $\log(\Lambda)$ plotted against C_F for various values of m; the lines connect calculated points.

theoretical loss rate and numerical simulation results from the commercial numerical software program CST Microwave Studio. For the theoretical loss rate, Eq. 2.14 was used. These results are for a frequency of 140 GHz in a confocal geometry with $R_c = 6.83$ mm.

2.1.3 Field equations and RF Lorentz force

Our quasi-optical approach to deriving the membrane function Ψ allows us to find the electromagnetic vector fields. This is necessary in order to determine the electromagnetic interaction between the gyrating electrons of the electron beam and the RF power of the microwaves. With the general solution of Eq. 2.6, we may write the vector fields of $\vec{E}$ and $\vec{H}$ as

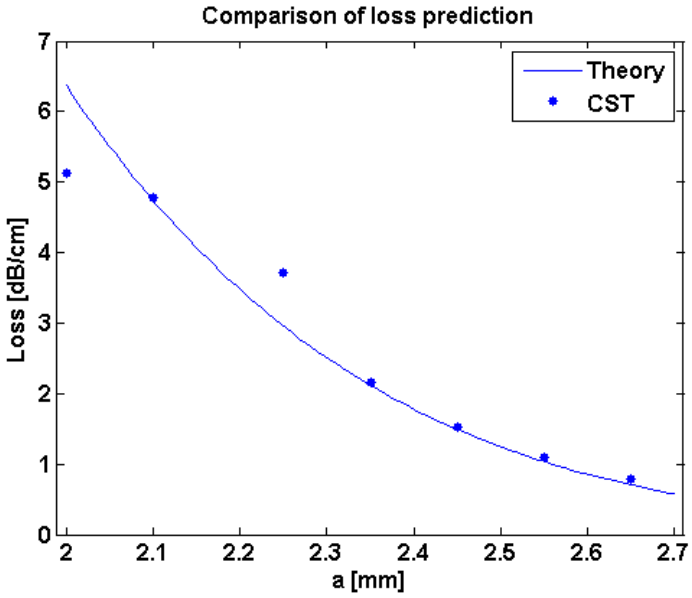

Figure 2-6: Comparison of loss rate due to diffraction using Eq. 2.14 and numerical simulation software CST for an HE_{06} mode. Here, $R_c = 6.83$ mm and the frequency is 140 GHz.

$$E_x = \frac{k}{k_{\perp r}^2}\frac{\partial \Psi}{\partial y} = \frac{k}{k_{\perp r}}(U^* - U) + \frac{k}{2k_{\perp r}^3}\frac{\partial^2}{\partial x^2}(U^* - U) \tag{2.16}$$

$$E_y = -\frac{k}{k_{\perp r}^2}\frac{\partial \Psi}{\partial x} = i\frac{k}{k_{\perp r}^2}\frac{\partial}{\partial x}(U + U^*) \tag{2.17}$$

$$H_x = \frac{k_{zr}}{k_{\perp r}^2}\frac{\partial \Psi}{\partial x} = -i\frac{k_{zr}}{k_{\perp r}^2}\frac{\partial}{\partial x}(U + U^*) \tag{2.18}$$

$$H_y = \frac{k_{zr}}{k_{\perp r}^2}\frac{\partial \Psi}{\partial y} = \frac{k_{zr}}{k_{\perp r}}(U^* - U) + \frac{k_{zr}}{2k_{\perp r}^3}\frac{\partial^2}{\partial x^2}(U^* - U) \tag{2.19}$$

along with the general solution that $H_z = U + U^*$ and, because of the transverse electric nature of this waveguide mode, $E_z = 0$, with $k = \omega/c$.

Equations 2.16-2.19 describe the transverse components under the quasi-optical approximation. Using these components, the RF Lorentz ($\vec{G}$) force may be found. The components of this force are necessary in order to analyze the interaction in this waveguide mode. A thin, annular electron beam of radius R_g (the "guiding center") is injected into the confocal cavity, as seen in Fig. 2-7. At each position around the guiding center exist populations of electrons with gyroradius r_c. The coordinate

transform between the guiding center (X, Y) and the beam center (x, y) is given by

$$x = X + r_c \cos\theta \tag{2.20}$$

$$y = Y + r_c \sin\theta \tag{2.21}$$

It is particularly useful to find the radial and azimuthal components of the Lorentz force (G_r & G_θ) at every guiding center due to the azimuthally-symmetrical electron beam [1].

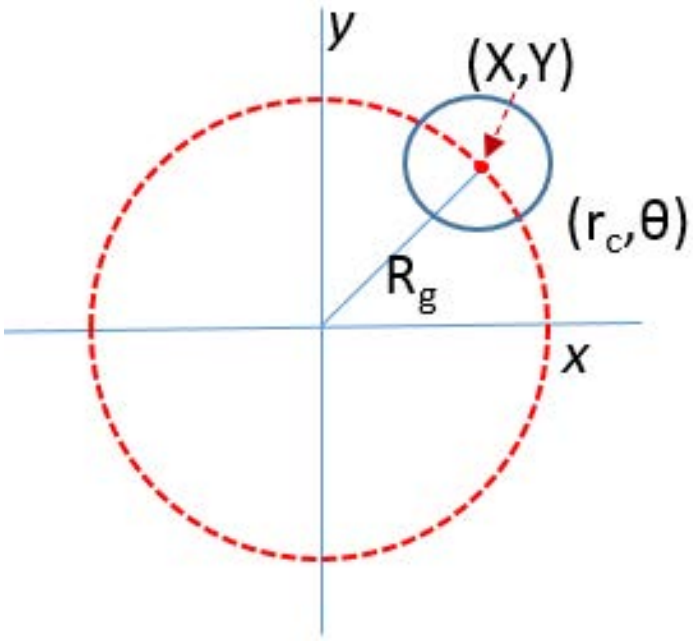

Figure 2-7: An exploded view of the geometry at every guiding center. (X, Y) are the coordinates of the location of the guiding center.

We start with the radial component of the RF Lorentz force.

$$G_r = (E_x - \beta_z H_y)\cos\theta + (E_y + \beta_z H_x)\sin\theta + \beta_\perp H_z \tag{2.22}$$

where β_z and $\beta_\perp$ are the axial and perpendicular electron velocities, v_z and $v_\perp$, normalized to the speed of light c, respectfully. We expand Eq. 2.22 in azimuthal harmonics:

$$G_r = \sum_l G_{lr} \exp(-il\theta) \tag{2.23}$$

As we are concerned with the fundamental harmonic, the first coefficient of the expansion ($l = 1$) should be found. With a coordinate transformation to the guiding center (X, Y), we may use Eqs. 2.16-2.19, 2.22 to express G_{1r} in terms of the function U.

$$\begin{aligned} G_{1r} = &-\frac{1}{2}\frac{k - \beta_z k_{zr}}{k_{\perp r}}(U - U^*) - \frac{1}{2}\frac{k - \beta_z k_{zr}}{2k_{\perp r}^3}\Big(\frac{\partial^2 U}{\partial X^2} - \\ &\frac{\partial^2 U^*}{\partial X^2}\Big) - \frac{1}{2}\frac{k - \beta_z k_{zr}}{k_{\perp r}^2}\Big(\frac{\partial U}{\partial X} + \frac{\partial U^*}{\partial X}\Big) \\ &+ \beta_\perp k_{\perp r} r_c \frac{1}{2}(U - U^*) \end{aligned} \tag{2.24}$$

In the limit of $k_{\perp r} r_c \to 0$, and using Eqs. 2.6 and 2.19 we can further reduce Eq. 2.24 with reference to Ψ as

$$G_{1r} = -i\frac{k - \beta_z k_{zr}}{2k_{\perp r}^2}\Big(\frac{\partial \Psi}{\partial X} + i\frac{\partial \Psi}{\partial Y}\Big) \tag{2.25}$$

Equation 2.25 relates the fundamental harmonic's radial RF Lorentz force to the membrane function, Ψ, the latter of which we have found via the quasi-optical approximation of the confocal field distribution. An analogous calculation may be computed for the azimuthal component of the Lorentz force, G_θ, which relates to the Cartesian field components as

$$G_\theta = (E_y + \beta_z H_x)\cos\theta - (E_x - \beta_z H_y)\sin\theta \tag{2.26}$$

Using a similar expansion $G_\theta = \sum_l G_{l\theta} e^{-il\theta}$, and restricting ourselves to the fundamental harmonic ($l = 1$), a similar treatment leads to an expression for $G_{1\theta}$ in terms of Ψ:

$$G_{1\theta} = -\frac{k - \beta_z k_{zr}}{2k_{\perp r}^2}\Big(\frac{\partial \Psi}{\partial X} + i\frac{\partial \Psi}{\partial Y}\Big) \tag{2.27}$$

Equations 2.25 and 2.27 comprise force terms that will be used in deriving the self-consistent set of gyro-TWT equations.

2.2 Discussion

We have introduced the concept of a confocal geometry and shown how a quasi-optical approach may be used to determine both the loss rate per unit length and the vector fields of its eigenmodes. The open geometry of the overmoded confocal waveguide supports 140 GHz whilst simultaneously is intended to suppress lower-order modes from competing due to the diffractive losses inherent in its design. In the following chapter, we will derive the equations that govern the interaction of the electron beam with the RF power.

Chapter 3

Gyro-Amplifier Equations

In this chapter, we discuss the physical method behind the transfer of energy from the perpendicular velocity component of the gyrating electrons to the RF field amplitude. First, we begin with a qualitative explanation of the mechanism for this energy transfer. We continue by using the equations in Section 2.1.3 to derive the governing equations of the electron beam-RF power interaction. A discussion of linear and nonlinear gain concludes this chapter.

Essentially, the mechanism that drives the energy transfer from the electron beam to the RF field is known as *bunching*. Electrons that are nominally equally distributed in phase about each Larmor radius in Fig. 2-7 are gradually brought together into a distinct bunch. Once formed, a charged bunch of electrons will interact with the RF fields to exchange energy, driving the amplification process. The initial seed RF power in the waveguide is what begins this bunching process. The derivation of the equations behind this mechanism are discussed in Section 3.0.1. A more qualitative explanation is given here now and relies on the dispersion relations for both the waveguide modes and the electron beam.

The waveguide mode dispersion relation is given by the usual formulation:

$$\omega^2 - k_z^2 c^2 - k_\perp^2 c^2 = 0 \tag{3.1}$$

where k_z and $k_\perp$ are the components of the wavevector, ω is the angular frequency,

and c is the speed of light. The wavevector components are set by the geometry of the waveguide, and in the case of a confocal geometry we have derived the components in Chapter 2. For the electron beam, the dispersion relation assumes the form of

$$\omega - \Omega_c - k_z v_z \approx 0 \tag{3.2}$$

where $\Omega_c = eB_o/m_e\gamma$ is the cyclotron frequency. In Ω_c, e is the electron charge, B_o is the magnetic field, m_e is the electron mass, and γ is the relativistic Lorentz factor $\gamma = 1/\sqrt{1 - v^2/c^2}$. It is interesting to note that the mechanics behind bunching rely on the inclusion of the Lorentz factor γ; without it, bunching would not happen. Although typical electron gun voltages are in the tens of kV, well below the relativistic regime, the Lorentz factor still needs to be included in numerical code in order for bunching to take place. When Eqs. 3.1, 3.2 are plotted together, we see that it is possible for the linear electron dispersion line to be tangential to the waveguide mode. This is shown in Fig. 5-19.

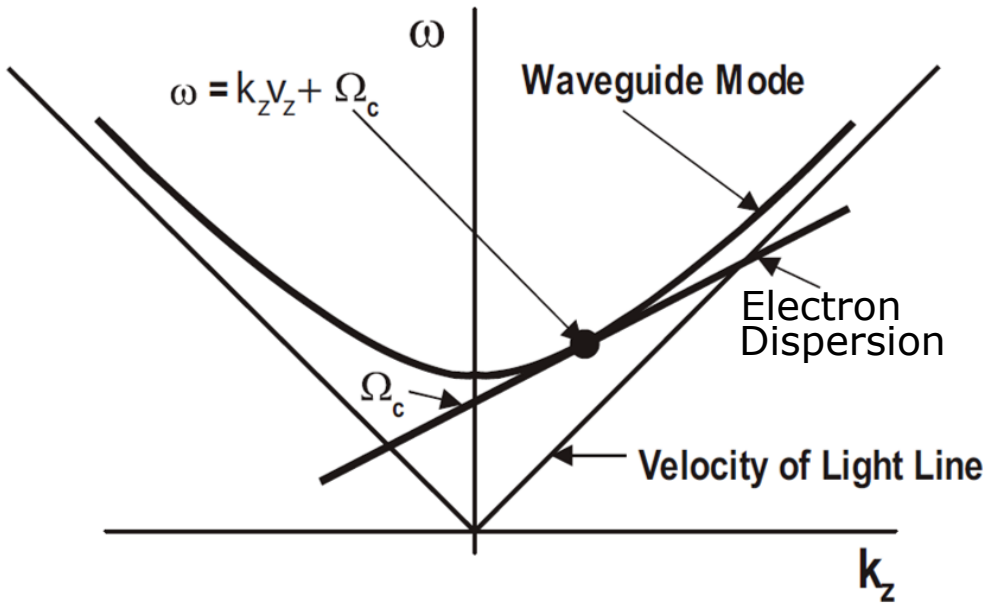

Figure 3-1: The electron beam dispersion line plotted with the waveguide mode. It is possible for the electron beam line to be tangential to the waveguide mode at a certain frequency.

Under this tangential condition, RF power at the corresponding frequencies in

the waveguide mode can interact with the gyrating electron beam. Important design points to note in Eq. 3.2 is that several electromagnetic parameters appear via the terms Ω and v_z. These include the magnetic field, B, the applied beam voltage (via the Lorentz term γ), and the pitch factor $\alpha = v_\perp/v_z$. Experimentally, these parameters are tunable to a certain extent, and must be considered when designing a gyro-amplifier system.

In the subsequent sections, we formally derive the electrodynamic motion equations as well as the field growth equations that underpin the gyro-amplifier physics. A discussion of both linear (small signal) gain and nonlinear (saturated) gain follows in Chapter 4.

3.0.1 Motion equations

The motion equations that govern the dynamics of an electron in a waveguide field begin with the fundamentals [1]:

$$\frac{dp_\perp}{dz} = -\frac{e}{v_z}\mathrm{Re}\Big(CG_\theta e^{i(\omega t - k_{zr}z)}\Big) \tag{3.3}$$

$$p_\perp \frac{d\psi}{dz} = \frac{e}{v_z}\mathrm{Re}\Big(CG_r e^{i(\omega t - k_{zr}z)}\Big) \tag{3.4}$$

where C is the waveguide mode amplitude, $p_\perp$ is the perpendicular electron momentum, G_θ and G_r are the RF Lorentz force components, and ψ is the electron phase in its gyro-orbit. In order to keep track of the phase advance due to electrons gyrating in the magnetic field, using the longitudinal momentum p_z we introduce the variable $h_H = eB_o/cp_z$ (which conveniently allows us to write the Larmor radius as $r_c = \frac{p_\perp}{h_H p_z}$) and B_o is the magnetic field. The longitudinal momentum is $p_z = \gamma mc\beta_z$. Then, the gyrophase can be defined as

$$\theta = h_H z + \psi \tag{3.5}$$

Equation 3.5 is useful to quantify the phase of the waveguide mode with respect

to the gyrophase:

$$\omega t - k_{zr} z - \theta = -\vartheta \tag{3.6}$$

Furthermore, as follows from Eqs. 2.25, 2.27

$$\frac{dp_\perp}{dz} = \frac{e}{v_z}\mathrm{Re}\Big(C\frac{k-\beta_z k_{zr}}{2k_{\perp r}}L_1(X,Y)e^{-i\vartheta}\Big) \tag{3.7}$$

where the coupling factor L_1 is

$$L_1(X,Y) = \frac{1}{k_{\perp r}}\Big(\frac{\partial\Psi}{\partial X} + i\frac{\partial\Psi}{\partial Y}\Big) \tag{3.8}$$

We can then take the differential Eqs. 3.5 and 3.6 and find that

$$\frac{d\vartheta}{dz} = \frac{d\psi}{dz} + \frac{\Omega + k_{zr}v_z - \omega}{\beta_z c} \tag{3.9}$$

where $\Omega = eB_o/\gamma mc$ is the cyclotron frequency. Now, we rewrite Eq. 3.4 as

$$\begin{aligned} p_\perp\frac{d\vartheta}{dz} + \frac{\omega - k_{zr}v_z - \Omega}{v_z}p_\perp = \\ \frac{e}{v_z}\mathrm{Re}\Big(C(-i)\frac{k-\beta_z k_{zr}}{2k_{\perp r}}L_1(X,Y)e^{-i\vartheta}\Big) \end{aligned} \tag{3.10}$$

For $\gamma_0, \beta_{z0}, \beta_{\perp 0}$, and Ω_0 defined at the beginning of the interaction ($z = 0$), we use normalized electron energy, w, and the parameter b:

$$w = 2\frac{1 - \frac{k_{zr}}{k}\beta_{z0}}{\beta_{\perp 0}^2}\frac{\gamma_0 - \gamma}{\gamma_0} \tag{3.11}$$

$$b = \frac{k_{zr}}{k}\beta_{\perp 0}^2\frac{1}{2\beta_{z0}(1 - \frac{k_{zr}}{k}\beta_{z0})} \tag{3.12}$$

(It can be seen that the product $bw = \frac{k_{zr}}{k}\frac{1}{2\beta_{z0}}\frac{\gamma_0-\gamma}{\gamma_0}$). The components of momentum may be rewritten to incorporate normalized electron energy as follows:

$$p_z = p_{z0}(1 - bw) \tag{3.13}$$

$$p_\perp = p_{\perp 0}\sqrt{1 - w} \tag{3.14}$$

We introduce the parameter μ,

$$\mu = \frac{\beta_{\perp 0}^2\Big(1 - \frac{k_{zr}^2}{k^2}\Big)}{2\Big(1 - \frac{k_{zr}}{k}\beta_{z0}\Big)} \tag{3.15}$$

The term $\frac{\omega - k_{zr}v_z - \Omega}{\beta_z c}$ in Eq. 3.9 may be expressed with b and μ as

$$\frac{\omega - k_{zr}v_z - \Omega}{\beta_z c} = \frac{\omega}{c\beta_{z0}(1 - bw)}\Big(\frac{\omega - k_{zr}v_{z0} - \Omega_0}{\omega} - \mu w\Big) \tag{3.16}$$

Therefore, Eq. 3.9 is conveniently expressed as

$$\begin{aligned}\frac{d\vartheta}{dz} = &-\frac{\omega}{c\beta_{z0}(1 - bw)}\Big(\frac{\omega - k_{zr}v_{z0} - \Omega_0}{\omega} - \mu w\Big) + \\ &\frac{em\gamma_0}{p_{z0}(1 - bw)}\frac{1}{p_{\perp 0}\sqrt{1 - w}} \times \\ &\mathrm{Re}\Big(-iC\frac{1 - \beta_{z0}\frac{k_{zr}}{k}}{2k_{\perp r}}kL_1(X, Y)e^{-i\vartheta}\Big)\end{aligned} \tag{3.17}$$

For further convenience, we may define the detuning parameter Δ:

$$\Delta = \frac{\omega - k_{zr}v_{z0} - \Omega_0}{\omega} \tag{3.18}$$

and normalize length as $z' = kz$. Then, the relative gyrophase ϑ, in normalized coordinates z', varies as

$$\begin{aligned}\frac{d\vartheta}{dz'} = &\frac{1}{\beta_{z0}(1 - bw)}\Big(\mu w - \Delta + \\ &\frac{1 - \frac{k_{zr}}{k}\beta_{z0}}{\gamma_0\beta_{\perp 0}\sqrt{1 - w}}\mathrm{Im}\Big[\frac{eC}{2mc^2k_{\perp r}}L_1 e^{-i\vartheta}\Big]\Big)\end{aligned} \tag{3.19}$$

To find the differential of the normalized electron energy, w, we may take the derivative of Eq. 3.14:

$$\begin{aligned}\frac{d}{dz'}(p_{\perp 0}\sqrt{1-w}) &= \frac{em\gamma_0}{p_{z0}(1-bw)} \\ &\quad\times \mathrm{Re}\Big(C\frac{1-\beta_{z0}\frac{k_{zr}}{k}}{2k_{\perp r}}L_1 e^{-i\vartheta}\Big) \qquad (3.20)\\ -\frac{1}{2\sqrt{1-w}}\frac{dw}{dz'} &= \frac{1}{m\gamma_0 c\beta_{\perp 0}}\frac{e}{c\beta_{z0}(1-bw)}\Big(1-\beta_{z0}\frac{k_{zr}}{k}\Big) \\ &\quad\times \mathrm{Re}\Big(C\frac{1}{2k_{\perp r}}L_1 e^{-i\vartheta}\Big) \qquad (3.21)\end{aligned}$$

From Eq. 3.21 we find that

$$\begin{aligned}\frac{dw}{dz'} &= -2\frac{\sqrt{1-w}}{1-bw}\Big(1-\beta_{z0}\frac{k_{zr}}{k}\Big)\frac{1}{\gamma_0\beta_{z0}\beta_{\perp 0}} \\ &\quad\times \mathrm{Re}\Big(\frac{eC}{2mc^2k_{\perp r}^2}L_1 e^{-i\vartheta}\Big) \qquad (3.22)\end{aligned}$$

We denote additional normalized variables with a prime:

$$\mu' = \frac{\mu}{\beta_{z0}} \qquad (3.23)$$

$$\Delta' = \frac{\Delta}{\beta_{z0}} \qquad (3.24)$$

$$C' = \frac{eC}{mc^2\gamma_0\beta_{z0}\beta_{\perp 0}}\Big(1-\beta_{z0}\frac{k_{zr}}{k}\Big)\frac{1}{k_{\perp r}} \qquad (3.25)$$

The above simplifications allow us to summarize the variation of both the relative gyrophase, ϑ, and normalized electron energy, w, with respect to normalized coordinates z':

$$\frac{d\vartheta}{dz'} = \frac{1}{1-bw}\Big(\mu' w - \Delta' + \frac{1}{\sqrt{1-w}}\mathrm{Im}\Big[C'\frac{1}{2}L_1 e^{-i\vartheta}\Big]\Big) \tag{3.26}$$

$$\frac{dw}{dz'} = -2\frac{\sqrt{1-w}}{1-bw}\mathrm{Re}\Big(C'\frac{1}{2}L_1 e^{-i\vartheta}\Big) \tag{3.27}$$

Equations 3.26 and 3.27 fully characterize the dynamical properties of an electron beam interacting with a waveguide mode at any guiding center (X, Y).

3.0.2 Mode excitation equations

Just as an electron is affected by the presence of a waveguide mode's EM field, the waveguide mode itself is also changed by the electron beam. Following the derivation in [1], the mode amplitude C_s (of the s-th mode of the waveguide) interacts with the electron beam via the mode's electric field as integrated over the waveguide cross section $S_\perp$:

$$\frac{dC_s}{dz} = -\frac{1}{N_s}\int_{S_\perp} \vec{j_\omega} \cdot \vec{E_s^*} ds_\perp \tag{3.28}$$

in which $\vec{j_\omega}$ is the current density component at the angular frequency ω. The normalization factor N_s of the s-th mode is

$$\begin{aligned} N_s = \frac{c}{4\pi}\int_{S_\perp} (\vec{E_s} \times \vec{H_s^*} + \vec{E_s^*} \times \vec{H_s})\vec{z_0} ds_\perp = \\ \frac{c}{2\pi}\mathrm{Re}\int_{S_\perp} (\vec{E_s} \times \vec{H_s^*})\vec{z_0} ds_\perp = 4P_s \end{aligned} \tag{3.29}$$

In Eq. 3.29, P_s is the Poynting vector. The normalization factor N_s is explicitly calculated in Section 3.1 for the case of a confocal waveguide. Since the electric field is purely transverse, the integrand in Eq. 3.28 is $\vec{j_\omega} \cdot \vec{E_s^*} = \vec{j_{\omega\perp}} \cdot \vec{E_s^*}$. Additionally, we know that by charge conservation in the electron beam, at any cross sectional slice the charge entering and exiting is conserved: $j_z dt = j_{z0} dt_0$. So, in considering the transverse current, we can relate it to the axial component by $\vec{j_\perp} d(\omega t) = \vec{j_\perp}\frac{j_{z0}}{j_z} d(\omega t_0)$.

Transforming to frequency space [1]:

$$\vec{j_{\omega\perp}} \cdot \vec{E_s^*} = \frac{1}{\pi} \int_0^{2\pi} \vec{j_\perp} \cdot \vec{E_s^*} e^{-i\omega t} d(\omega t) \tag{3.30}$$

Using the formulation to relate $d(\omega t)$ to $d(\omega t_0)$, Eq. 3.30 may be rewritten as

$$\frac{1}{\pi} \int_0^{2\pi} \vec{j_\perp} \frac{j_{z0}}{j_z} e^{-i\omega t} \vec{E_s^*} d(\omega t_0) = \frac{1}{\pi} j_{z0} \int_0^{2\pi} \frac{\vec{p_\perp}}{p_z} \vec{E_s^*} e^{-i\omega t} d(\omega t_0) \tag{3.31}$$

Using the relations for momentum in Eqs. 3.13 and 3.14 as well as recognizing that the area integral in Eq. 3.28 reduces to $(j_{z0} S_\perp)$, the differential equation for the growth of the amplitude C (dropping the mode number s) becomes

$$\frac{dC}{dz} = \frac{1}{N} \frac{1}{\pi} (j_{z0} S_\perp) \int_0^{2\pi} \frac{p_{\perp 0} \sqrt{1-w}}{p_{z0}(1-bw)} E_{1\vartheta}^*(x,y) e^{i\vartheta} d\vartheta_0 \tag{3.32}$$

in which $E_{1\theta}$ is the azimuthal component of the electric field (which interacts with the gyrating current component). The interaction is at the fundamental harmonic, so in the usual expansion $E_\theta = \sum E_{l\theta} e^{-il\theta}$ we are interested in $l = 1$.

Using the field Eqs. 2.16 and 2.17 and the fact that $E_\theta = E_y \cos\theta - E_x \sin\theta$, the fundamental harmonic $E_{1\theta}$ is

$$E_{1\theta} = -\frac{k}{2k_{\perp r}^2} \Big(\frac{\partial \Psi}{\partial X} + i \frac{\partial \Psi}{\partial Y} \Big) = -\frac{k}{2k_{\perp r}} L_1 \tag{3.33}$$

This is a result that follows the derivation for G_{1r} in Eq. 2.22. Thus, the amplitude differential dC/dz is rewritten as

$$\frac{dC}{dz} = -\frac{1}{N} \frac{1}{\pi} I_b \int_0^{2\pi} \frac{p_{\perp 0} \sqrt{1-w}}{p_{z0}(1-bw)} \frac{k}{2k_{\perp r}} L_1^* e^{i\vartheta} d\vartheta_0 \tag{3.34}$$

where I_b is the beam current. It is convenient to rewrite Eq. 3.34 in normalized form:

$$\begin{aligned}\frac{dC'}{dz'} &= \frac{e}{mc^2\gamma_0\beta_{\perp 0}\beta_{z0}k_{\perp r}}\Big(1-\frac{k_{z0}}{k}\beta_{z0}\Big)\frac{1}{k}\frac{dC}{dz} \\ &= -\frac{1}{N}\frac{1}{\pi}I_b\frac{e}{mc^2\gamma_0\beta_{\perp 0}\beta_{z0}k_{\perp r}}\Big(1-\frac{k_{z0}}{k}\beta_{z0}\Big)\times \\ &\frac{\beta_{\perp 0}}{\beta_{z0}k_{\perp r}}\int_0^{2\pi}\frac{\sqrt{1-w}}{1-bw}\frac{L_1^*}{2}e^{i\vartheta}d\vartheta_0\end{aligned} \tag{3.35}$$

We make one final simplification and introduce the normalized current, I_0, defined as

$$I_0 = 2\Big(\frac{eI_b}{mc^3}\Big)\frac{1-\frac{k_{z0}}{k}\beta_{z0}}{\gamma_0\beta_{z0}^2(\frac{k_{\perp r}}{k})^2}\frac{c^3}{\omega^2 N} \tag{3.36}$$

where

$$\frac{eI_b}{mc^3} = \frac{I_b(A)}{17000(A)} \tag{3.37}$$

In Eq. 3.37 the fraction $\frac{mc^3}{e}$ reduces to 17000 amps in SI units. Finally, the differential of the normalized amplitude C' in normalized units z' is expressed as

$$\frac{dC'}{dz'} = -I_0\frac{1}{2\pi}\int_0^{2\pi}\frac{\sqrt{1-w}}{1-bw}\frac{L_1^*}{2}e^{i\vartheta}d\vartheta_0 \tag{3.38}$$

Equations 3.26, 3.27, and 3.38 comprise the (normalized) self-consistent set of equations that describe gyro-TWT operation. In Eq. 3.38, a loss term may be introduced in the system if we consider an imaginary component to the axial wavevector, k_{zi}. Properly normalized, loss in the system is represented by $\frac{dC'}{dz'} \sim -k'_{zi}C'$ where $k'_{zi} = k_{zi}/k$.

In the absence of loss, it is convenient to derive an energy conservation relation. Since energy is transferred between the electrons and the field (power $\sim |C|^2$), we may use Eq. 3.38 to find that

$$\begin{aligned}\frac{d}{dz'}|C'|^2 = C'^*\frac{dC'}{dz'} + C'\frac{dC'^*}{dz'} &= I_0\frac{1}{2\pi}\int_0^{2\pi}\frac{dw}{dz'}d\vartheta_0 \\ |C'|^2 - |C'_{z=0}|^2 &= I_0\frac{1}{2\pi}\int_0^{2\pi}w d\vartheta_0\end{aligned} \tag{3.39}$$

The form of Eq. 3.39 is an expression of the conservation of energy in the system and relates the change of microwave energy to that of the electrons.

3.1 Normalization factor

The normalization factor first introduced in Eq. 3.29 has an analytical expression dependent on the field distribution of the operating mode. In our case, the quasi-optical approximation of the confocal waveguide mode is used to find an analytical solution for the normalization factor. To begin, we may relate the normalization factor N_s to the field distribution U by taking the explicit cross product in Eq. 3.29. Expanding the cross product, we find that

$$\vec{E_s} \times \vec{H_s^*} \cdot \vec{z_0} = E_x H_y^* - E_y H_x^* \tag{3.40}$$

Referring to Eqs. 2.16 - 2.19, Eq. 3.40 is equivalently

$$\begin{aligned} E_x H_y^* - E_y H_x^* = \\ \frac{k k_{zr}}{k_{\perp r}^2}(U - U^*)^2 + \frac{k k_{zr}}{k_{\perp r}^4}\Big(\frac{\partial U}{\partial X} + \frac{\partial U^*}{\partial X}\Big)^2 \end{aligned} \tag{3.41}$$

Equation 3.41 is a general result; we may consider the quasi-optical approximation of the field distribution in a confocal waveguide mode by using the expression for U given in Eq. 2.7 and write the integral in Eq. 3.29:

$$
\begin{aligned}
N_s = \frac{c}{2\pi}\frac{kk_{zr}}{k_{\perp r}^2}\iint \Big[& -4\sqrt{\frac{2}{\pi}}\frac{w_0}{w}\exp\Big(-\frac{2x^2}{w^2}\Big) \\
& \sin^2\Big(k_{\perp r}y + \frac{k_{\perp r}x^2}{2R} - \frac{1}{2}\arctan\frac{y}{b_o}\Big) + \\
& \frac{1}{k_{\perp r}^2}4\sqrt{\frac{2}{\pi}}\Big(\frac{2x}{w^2}\sqrt{\frac{w_0}{w}}\exp\Big(-\frac{x^2}{w^2}\Big)\cos\Big(k_{\perp r}y + \frac{k_{\perp r}x^2}{2R} \\
& - \frac{1}{2}\arctan\frac{y}{b_o}\Big) + \frac{k_{\perp r}x}{R}\sqrt{\frac{w_0}{w}}\exp\Big(-\frac{x^2}{w^2}\Big)\sin\Big(k_{\perp r}y \\
& + \frac{k_{\perp r}x^2}{2R} - \frac{1}{2}\arctan\frac{y}{b_o}\Big)\Big)^2\Big] dxdy
\end{aligned}
\tag{3.42}
$$

Equation 3.42 is an exact solution; we may take two approximations that will result in an analytical expression for the integrals. First, the argument of the trigonometric functions, $k_{\perp r}y + \frac{k_{\perp r}x^2}{2R} - \frac{1}{2}\arctan\frac{y}{b_o}$, describes a phase front. Under a paraxial approximation, the large term $k_{\perp r}y$ dominates, and therefore the argument of the trigonometric functions reduces to that single term. Second, we notice that in Eq. 3.42 the first term comes from the cross product component $E_xH_y^*$ whereas the remaining two are from $E_yH_x^*$. As has been seen in the field distribution of the confocal waveguide modes, the transverse term $E_x \gg E_y$. It follows that the first term of Eq. 3.42 dominates, and we may drop the remaining two. With these approximations, the normalization reduces to

$$
\begin{aligned}
N_s \simeq \frac{c}{2\pi}\frac{kk_{zr}}{k_{\perp r}^2}\iint \Big[& -4\sqrt{\frac{2}{\pi}}\frac{w_0}{w(y)} \\
& \times \exp\Big(-\frac{2x^2}{w^2(y)}\Big)\sin^2(k_{\perp r}y)\Big] dxdy
\end{aligned}
\tag{3.43}
$$

The limits of integration are $-\infty < x < \infty$ and $-L_\perp/2 < y < L_\perp/2$. We find that the normalization may be approximated as

$$
\begin{aligned}
N_s &\simeq -\frac{c}{\pi}\frac{kk_{zr}}{k_{\perp r}^2}L_\perp w_0 \\
\frac{c^3}{\omega^2 N_s} &= -\frac{c^3\pi k_{\perp r}^2}{\omega^2 ckk_{zr}L_\perp w_0} = -\frac{\pi}{k^3 k_{zr}}\frac{k_{\perp r}^2}{L_\perp\sqrt{L_\perp}}\sqrt{k_{\perp r}}
\end{aligned}
\tag{3.44}
$$

in which the final step is found from evaluating the radius $R(y = \frac{L_\perp}{2}) = L_\perp$ in Eq. 2.9 and therefore

$$
w_0 = \sqrt{\frac{L_\perp}{k_{\perp r}}} \tag{3.45}
$$

3.2 Discussion

In this chapter, we have discussed the underlying physics behind the gyro-amplifier operation. We have additionally derived the governing equations within the framework of a confocal waveguide. Next, we will examine the resulting equations with numerical simulations and introduce the concept of beamlets as a numerical tool.

Chapter 4

Beamlets

In Chapter 3 we derived the fundamental equations for the gyro-amplifier interaction. As part of the derivation, we applied the quasi-optical approximation of the confocal waveguide modes to the normalization factor in Section 3.1. As has been noted, the confocal modes are inherently azimuthally asymmetric. In this chapter, we examine the effect of this azimuthal asymmetry on the predicted gain by using a numerical tool called beamlets. Linear and nonlinear gains are discussed and numerical simulation examples shown. The effect of velocity spread, an important metric in quantifying the quality of the electron beam, is also discussed.

4.0.1 Beamlets and Coupling Factor

The spatial geometry of the interaction between the electron beam and the electromagnetic wave is embodied by the form factor, L_s (for the fundamental harmonic, $s = 1$), of the waveguide mode, which was given in Eq. 3.8. In the case of the confocal cavity, the form factor takes on different values at different guiding centers because the confocal modes (operating mode of HE_{06}) is azimuthally asymmetric. The lack of azimuthal symmetry means that different locations around the annular electron beam will experience locally different electromagnetic field strengths. This is seen in Fig. 4-1, which schematically features the annular electron beam discretized, overlaid on to the HE_{06} spatial mode of the confocal waveguide.

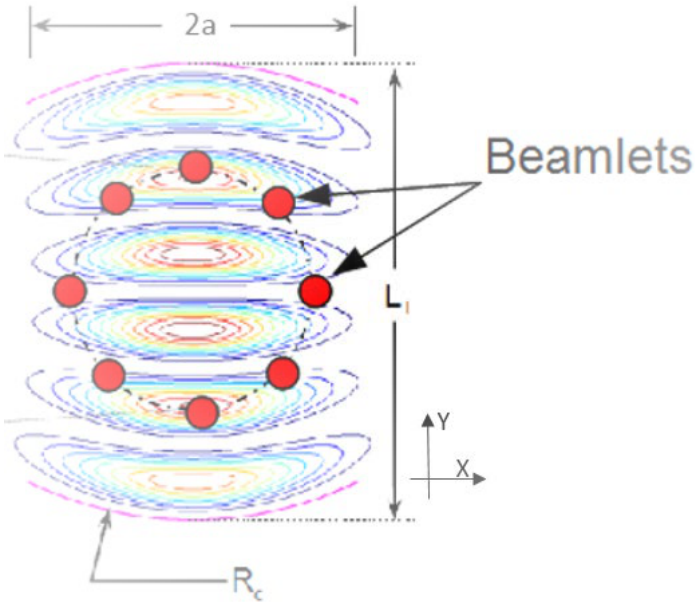

Figure 4-1: Schematic of a HE_{06} mode supported by a confocal geometry. The annular electron beam is shown as a dashed circle, and is discretized into distinct beamlets, shown as red dots. The coupling factor at different beamlets depends on the (asymmetric) field distribution of the HE_{06} mode.

The field pattern is clearly different at individual points around the guiding center radius of the electron beam, and this must be taken into account for the simulation of the gain from this interaction. In fact, the local coupling factor L_1 can be significantly different at various locations about the annular electron beam's interaction with the confocal mode. Using the results of the quasi-optical approximation in Section 2.1.1, we can numerically find this variation in L_1, shown in Fig. 4-2.

The dependence of L_1 on the location (angle) around the annular electron beam indicates that the local coupling is highly asymmetric with respect to the azimuthal coordinate. We can study how this fact may affect the calculated gain in both the linear and nonlinear regimes.

4.1 Linear Gain

Linear gain is derived by expanding Eqs. 3.26, 3.27, and 3.38 to first order. This linearization is appropriate for estimating the gain in the circuit when seeded by a

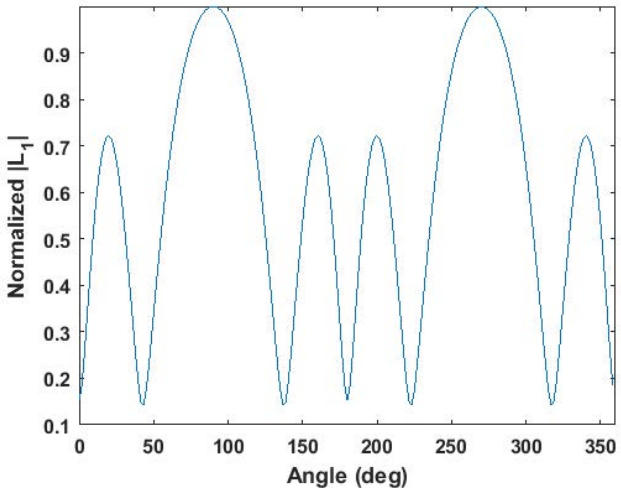

Figure 4-2: Coupling factor L_1 around an electron beam interacting with the HE_{06} mode of a confocal geometry with mirror radius $R_c = 6.83$ mm and beam radius $R_g = 1.6$ mm. Numerically, the coupling factor varies significantly with guiding center location.

small signal. In this section we expand the full gyro-amplifier equations and show that the asymmetry of a mode and electron beam is in fact irrelevant in the computation of linear gain. It suffices to simply take the average of the form factor, $\langle |L_1|^2 \rangle$ in the computation of linear gain.

We begin with the differential equations describing the evolution of electron phase, electron energy, and field amplitude, denoted respectively by [1] as θ, w, and C. The equations are derived in Section 3.0.2. For N guiding centers, these differential equations become

$$\frac{d\theta_n}{dz} = \frac{1}{1-bw_n}\{\mu w_n - \Delta + \frac{1}{2\sqrt{1-w_n}}\mathrm{Im}[CL_{1n}e^{-i\theta_n}]\} \tag{4.1}$$

$$\frac{dw_n}{dz} = -\frac{\sqrt{1-w_n}}{1-bw_n}\mathrm{Re}[CL_{1n}e^{-i\theta_n}] \tag{4.2}$$

$$\frac{dC}{dz} = -\frac{1}{N}I_o\sum_{n=1}^{N}\frac{1}{4\pi}\int_0^{2\pi}\frac{\sqrt{1-w_n}}{1-bw_n}{L_{1n}}^* e^{-i\theta_n}d\theta_{0n} \tag{4.3}$$

where the subscript n denotes the nth guiding center of an annular electron beam.

Effectively, the net field amplitude is the sum of contributions of electrons at all guiding centers, which in a numerical code will be discretized. The parameters b, μ, and Δ are related to the initial conditions of the electron beam-RF interaction at the beginning of the circuit ($z = 0$) and are defined in Section 3.0.1. Additionally, the values of θ_n, w_n, and C at $z = 0$ are, respectfully, a uniform distribution of the electrons over the entire Larmor radius in phase (0 to 2π), $w_n|_{z=0} = 0$, and $C(z = 0)$ numerically determined by the power in the waveguide mode. Furthermore, the integral in Eq. 4.3 is taken over the initial phase θ_{0n} at $z = 0$. In general, the terms L_{1n} are different for different guiding centers. Using the substitution

$$C = \bar{C}e^{-i\Delta z} \tag{4.4}$$

as well as a first order expansion

$$\theta_n = \theta_{0n} - \Delta z + \theta_n^{(1)} \tag{4.5}$$

$$w_n = w_n^{(1)} \tag{4.6}$$

we can rewrite Eqs. 4.1-4.3 in the following form:

$$\frac{d\theta_n^{(1)}}{dz} = (\mu - \Delta b)w_n^{(1)} + \frac{1}{2}\mathrm{Im}[\bar{C}L_{1n}e^{-i\theta_{0n}}] \tag{4.7}$$

$$\frac{dw_n^{(1)}}{dz} = -\mathrm{Re}[\bar{C}L_{1n}e^{-i\theta_{0n}}] \tag{4.8}$$

$$\frac{d\bar{C}}{dz} - i\Delta\bar{C} = -\frac{1}{N}I_0\sum_{n=1}^{N}\frac{1}{2\pi}\int_0^{2\pi}\Big[\Big(b - \frac{1}{2}\Big)w_n^{(1)} + i\theta_n^{(1)}\Big]\frac{1}{2}L_{1n}^* e^{i\theta_{0n}}d\theta_{0n} \tag{4.9}$$

The superscript (1) denotes the first-order terms for w_n and θ_n. To handle the integral over θ_{0n} in Eq. 4.9, we introduce a change of variables:

$$\bar{w_n}^{(1)} = \frac{1}{2\pi}\int_0^{2\pi} w_n^{(1)} L_{1n}^* e^{i\theta_{0n}} d\theta_{0n} \tag{4.10}$$

$$\bar{\theta_n}^{(1)} = \frac{1}{2\pi}\int_0^{2\pi} \theta_n^{(1)} L_{1n}^* e^{i\theta_{0n}} d\theta_{0n} \tag{4.11}$$

With this change of variables, Eqs. 4.7-4.9 become

$$\frac{d\bar{\theta_n}^{(1)}}{dz} = (\mu - \Delta b)\bar{w_n}^{(1)} - \frac{i}{4}\frac{1}{2\pi}\int_0^{2\pi} \bar{C} L_{1n} L_{1n}^* d\theta_{0n} \tag{4.12}$$

$$\frac{d\bar{w_n}^{(1)}}{dz} = -\frac{1}{2}\bar{C} L_{1n} L_{1n}^* \tag{4.13}$$

$$\frac{d\bar{C}}{dz} - i\Delta\bar{C} = -\frac{1}{N} I_0 \frac{1}{2}\sum_{n=1}^{N}\left[\left(b - \frac{1}{2}\right)\bar{w_n}^{(1)} + i\bar{\theta_n}^{(1)}\right] \tag{4.14}$$

As a final step, we note that we can sum over the N guiding centers index, n, by taking the express average over the guiding centers:

$$\bar{\bar{\theta}}^{(1)} = \frac{1}{N}\sum_{n=1}^{N}\bar{\theta_n}^{(1)} \tag{4.15}$$

$$\bar{\bar{w}}^{(1)} = \frac{1}{N}\sum_{n=1}^{N}\bar{w_n}^{(1)} \tag{4.16}$$

Finally, we can simplify Eqs. 4.12-4.14 to:

$$\frac{d\bar{\bar{\theta}}^{(1)}}{dz} = (\mu - \Delta b)\bar{\bar{w}}^{(1)} - \frac{i}{4}\bar{C}\frac{1}{N}\sum_{n=1}^{N}|L_{1n}|^2 \tag{4.17}$$

$$\frac{d\bar{\bar{w}}^{(1)}}{dz} = -\frac{1}{2}\bar{C}\frac{1}{N}\sum_{n=1}^{N}|L_{1n}|^2 \tag{4.18}$$

$$\frac{d\bar{C}}{dz} - i\Delta\bar{C} = -\frac{1}{2}I_0\left(b - \frac{1}{2}\right)\bar{\bar{w}}^{(1)} - \frac{i}{2}I_0\bar{\bar{\theta}}^{(1)} \tag{4.19}$$

In considering linear gain, we assume that $\frac{d}{dz} = i\Gamma$. This comes from an ex-

ponential field growth of $\exp(-i\Gamma z)$. Consequently, Eqs. 4.17-4.19 can be reduced to

$$(\mu - \Delta b)\bar{\bar{w}}^{(1)} - i\Gamma\bar{\bar{\theta}}^{(1)} - \frac{i}{4}\langle|L_1|^2\rangle\bar{C} = 0 \tag{4.20}$$

$$i\Gamma\bar{\bar{w}}^{(1)} + \frac{1}{2}\langle|L_1|^2\rangle\bar{C} = 0 \tag{4.21}$$

$$\frac{1}{2}I_0\left(b - \frac{1}{2}\right)\bar{\bar{w}}^{(1)} + \frac{i}{2}I_0\bar{\bar{\theta}}^{(1)} + (i\Gamma - i\Delta)\bar{C} = 0 \tag{4.22}$$

in which $\langle|L_1|^2\rangle \equiv \frac{1}{N}\sum_{n=1}^{N}|L_{1n}|^2$ is the averaged form factor over the guiding centers. We note that Eqs. 4.20-4.22 show that the reduced first-order expansion of considering multiple beamlets has simplified to the standard expression for linear growth as derived in [89], provided that the form factor in question is computed from an average of all guiding radii. Indeed, with the variable $I_0' = \frac{1}{4}I_0\langle|L_1|^2\rangle$, we can find that the polynomial dictating the gain term Γ is

$$\Gamma^2(\Gamma - \Delta) + \Gamma(b-1)I_0' + (\mu - \Delta b)I_0' = 0 \tag{4.23}$$

Thus, the linear gain when considering form factors that depend on the guiding center is identical to that of an approach that averages over all of the guiding centers. This fact reflects the superposition principle in the linear regime. This is useful computationally, because it shows that if the form factor L_1 is calculated from $\sqrt{\langle|L_1|^2\rangle}$, the resulting value can be used in Eq. 4.23 to compute the linear gain directly, but not the nonlinear gain.

Equation 4.23 is a third-order polynomial that can be numerically solved for a calculation of linear gain versus frequency. An example linear gain bandwidth is shown in Fig. 4-3. The confocal rail distance is 6.83 mm, the beam voltage is 35 kV, the beam current is 3 A, the pitch factor α is 1.5, the guiding center radius is 1.8 mm (chosen to interact with the peak field values of the HE_{06} mode), and the magnetic field is 5.12 T. This example gain bandwidth demonstrates that it is possible to achieve an appreciable gain per unit length over a broad bandwidth using the HE_{06}

mode of the confocal waveguide.

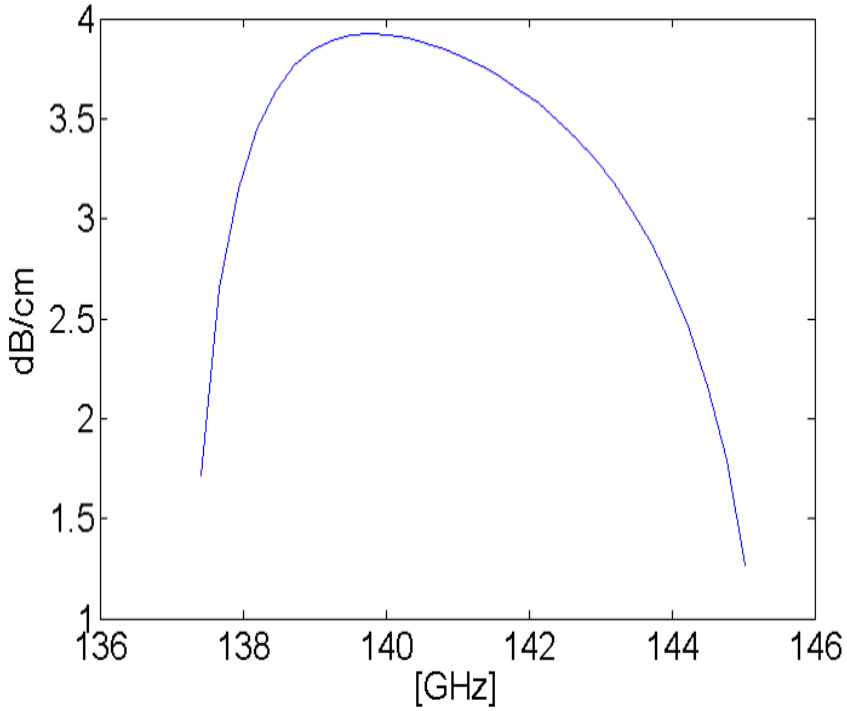

Figure 4-3: An example calculated gain bandwidth that demonstrates a linear gain per unit length of about 4 dB/cm at 140 GHz. A wide bandwidth is also seen.

4.2 Nonlinear Code Results

The nonlinear beamlet code was developed for application to interaction circuits which lack azimuthal symmetry (e.g. a confocal waveguide operating in the HE_{06} mode). For the beamlet method, the annular beam is divided into discrete beamlets, each with a coupling factor L_{1n}, calculated according to their relative location in the field distribution (c.f. Fig. 4-1 and 4-2). A second method using a single beamlet and beam averaged coupling coefficient $\langle L_1 \rangle$ is presented for comparison. For the beamlet method in all instances, 100 total beamlets are utilized, which well-discretizes the spatial variance of the fields. As a means of verifying the beamlet code, the gain for a circular waveguide operating in the azimuthally symmetric TE_{03} mode was calculated and compared with the predictions of MAGY [90]. Figure 4-4 shows that the gain

predicted by MAGY and the beamlet code are almost identical.

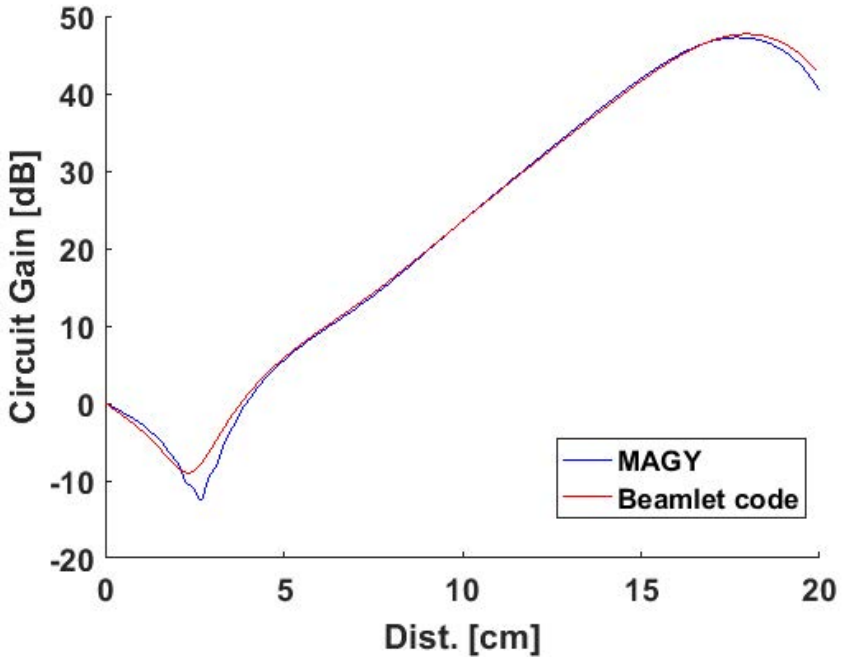

Figure 4-4: The gain for a TE_{03} mode as predicted by the beamlet and MAGY codes. The operating condition simulated is for a 141 GHz signal at 5.085 T, 37 kV, a pitch factor of 0.9, 3 A beam current, input power 50 mW, and a pipe radius of 3.54 mm.

The gain of a confocal waveguide operating in the HE_{06} mode is shown in Fig. 4-5 for both the beamlet method and the beam averaged coupling coefficient approach. These simulations were performed for 140 GHz with 50 mW input power, 5.085 T, 37 kV, 3 A beam current, confocal rail spacing $R_c = 6.83$ mm, a pitch factor α of 0.9, and a loss per unit length of 3 dB/cm, which represent typical operating values.

A difference of $\sim$ 1.7 dB in peak gain is computed between the code using an averaged L_1 and that of the beamlet simulation as seen in Fig. 4-5. This 1.7 dB difference in peak gain is observed to be invariable over a range of input power, as seen in Fig. 4-6 for the same operating conditions. Although the saturated gain difference of 1.7 dB appears small, it is important when considering power. For the case shown in Fig. 4-5, the estimated saturated output power is 500 W for the averaged case, but is only 360 W when accurately calculated by the beamlet theory.

Electron beam velocity spread is an important factor that can impact the predicted

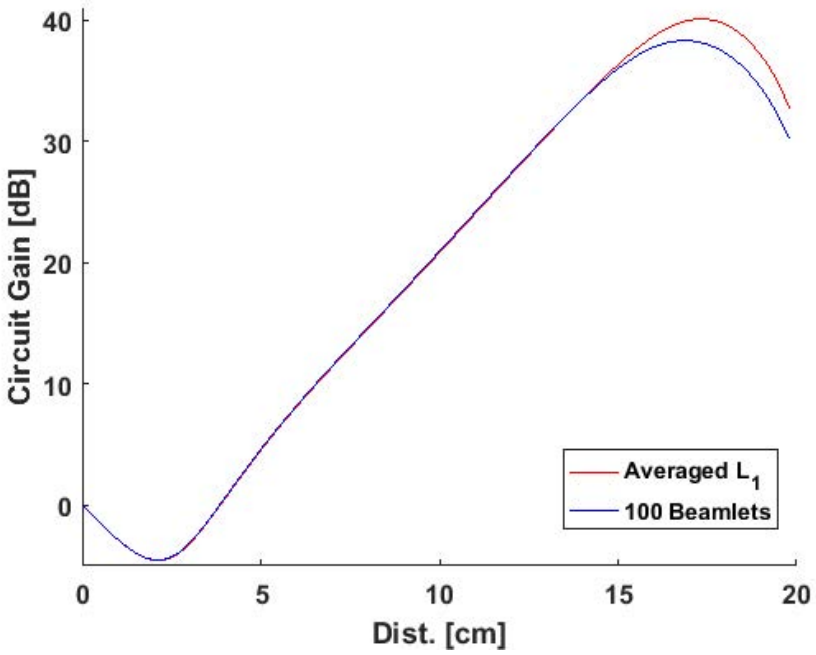

Figure 4-5: Confocal circuit gain versus interaction distance calculated using a single beam averaged coupling factor $\langle L_1 \rangle$, and 100 beamlets.

gain of a gyrotron amplifier and has been studied analytically as well as numerically [91, 92]. We take the approach used in [92] to model the effect of a non-cold electron beam (a distribution of electron velocities is introduced).

The developed code was used to study the effect of velocity spread on the saturated gain in the confocal mode. The calculated gain in Fig. 4-7 is shown for an operating point of 5.085 T, 37 kV, 3 A beam current, a pitch factor of 0.8, confocal radius 6.83 mm, 3 dB/cm waveguide loss, and 1 W input power at 140 GHz.

The difference between saturated gain as calculated with an averaged coupling factor and the beamlet approach is shown in Fig. 4-7.

The results in Fig. 4-7 emphasize the importance of properly accounting for the effect of velocity spread on circuit gain. Again, as in Fig. 4-7, the use of a beam averaged coupling coefficient is found to overpredict the saturated circuit gain.

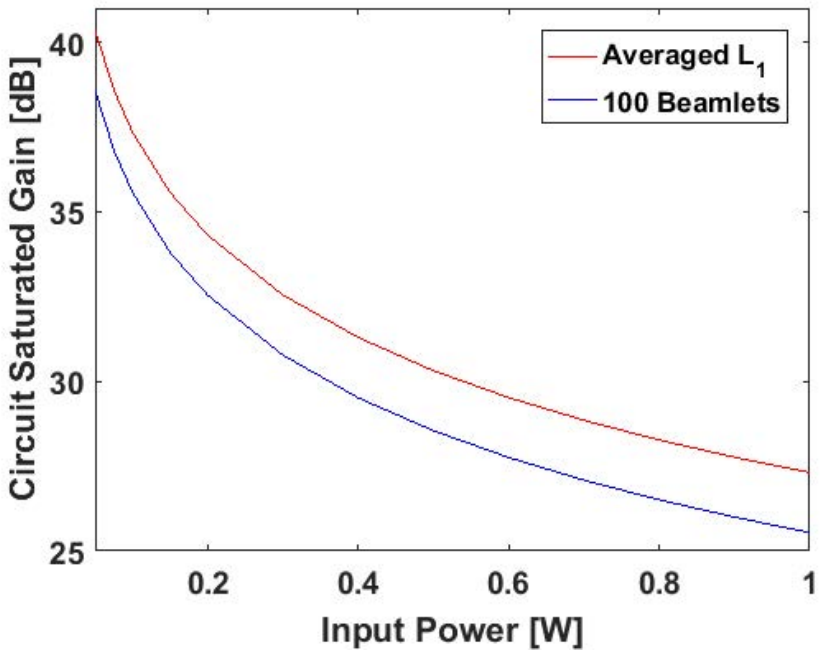

Figure 4-6: The peak confocal circuit gain versus input power as calculated using the beam averaged coupling factor method and the beamlet method.

4.3 Discussion

In this chapter, we have examined the governing gyro-amplifier equations with an intention of developing a practical application of them. Namely, we have linearized the full gyro-amplifier equations and have shown that the azimuthal asymmetry of the HE_{06} mode is irrelevant in this linearized regime. Subsequently, we introduced the concept of beamlets as a numerical tool to account for the mode's asymmetry when calculating the gain in the nonlinear regime. Both the linear and nonlinear regimes are important for developing an engineered gyro-amplifier system.

In regard to the asymmetry of the HE_{06} mode, due to nulls in its spatial distribution portions of the annular electron beam are not interacting strongly with the mode. Consequently, electrons at these guiding centers may not fully bunch, and the energy that they carry will remain in the transverse velocity component. In the case of the confocal waveguide modes, it is seen that the interaction between electrons in a given guiding center with the spatial mode depends on the location of the guiding center relative to the confocal geometry. Therefore, calculating an aver-

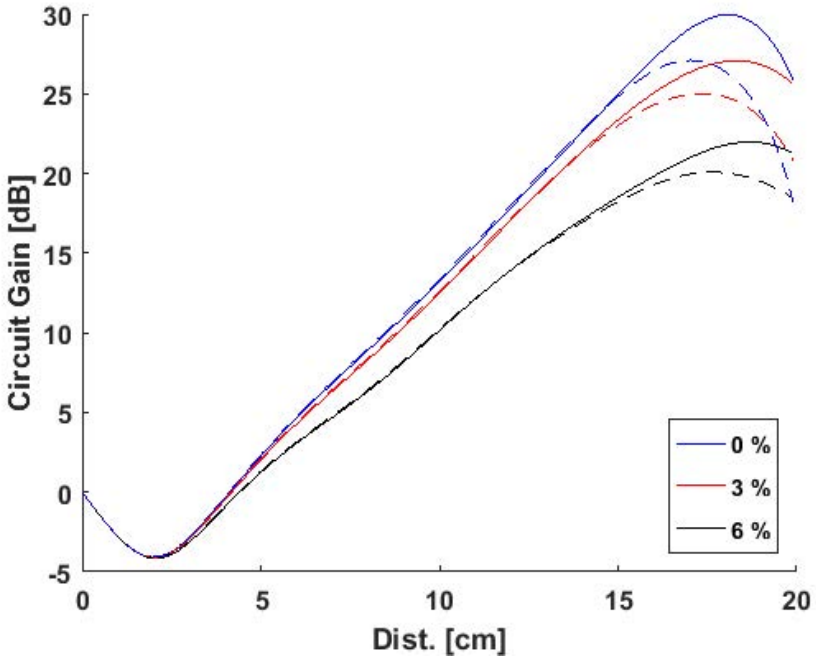

Figure 4-7: Confocal circuit gain versus interaction distance for various specified RMS velocity spread values. Solid curves are calculated using a beam averaged coupling factor $\langle L_1 \rangle$ and dashed curves are calculated using the beamlet method.

aged interaction value may over-sample the net coupling between the electron beam and the waveguide mode. This will result not only in a higher predicted gain but also in a diminished effect from increased waveguide loss, as sections of the electron beam that in reality are not interacting with the waveguide mode are included via the averaging calculation. In the beamlet case, which accurately accounts for the asymmetry of the waveguide mode, certain regions of the electron beam do not factor prominently into the gyrotron interaction. Consequently, those beamlets that are interacting with a strong field region amount to the entirety of the gyrotron interaction. Increased waveguide loss lowers the field strength, which adversely affects the bunching mechanism, leading to a greater difference in the predicted gain when comparing the averaged coupling against the beamlet code. Finally, the inclusion of velocity spread was demonstrated. At moderate velocity spread values, the difference in calculated gain has only a minor dependence on the absolute velocity distribution. This is consistent with the argument that it is the spatial distribution of asymmetric

modes, and the poor coupling between beam and mode at certain spatial locations, that contributes to a difference in calculated saturated gain.

Using the numerical tools developed in this chapter, an operating condition can be determined and the design of a hot test confocal waveguide gyro-amplifier engineered. In the following chapter, we discuss the considerations and approach to constructing a functioning hot test of a confocal gyro-amplifier.

Chapter 5

Experiment and Results of the Confocal Gyro-TWT

In this chapter we discuss the experimental setup and results of the confocal gyro-TWT study. We have previously seen how the confocal geometry can be used as an interaction waveguide, and how the radiative loss mechanism introduces mode selectivity to the system. Now, we take a look at the important components of the entire gyro-TWT experiment. These individual systems, such as the magnet, electron gun, mode converters, etc., need to be integrated in order for the gyro-TWT to be successful. We begin this chapter with an overview of these components.

5.1 Experimental Setup of the Confocal Gyro-TWT

A photograph of the laboratory setup as used during the confocal gyro-TWT experiment is shown in Fig. 5-1.

As can be seen in Fig. 5-1, the laboratory setup and gyro-TWT are macroscopic - the dimensions involved are on the order of centimeters to meters. This is contrasted with the millimeter-scale of the confocal waveguide and mode converters, where mechanical tolerances need to be within tens of microns. The heart of the gyro-TWT is the vacuum tube and internal components, which include the confocal waveguide. This tube is inside the bore of the superconducting magnet, spaced such that the

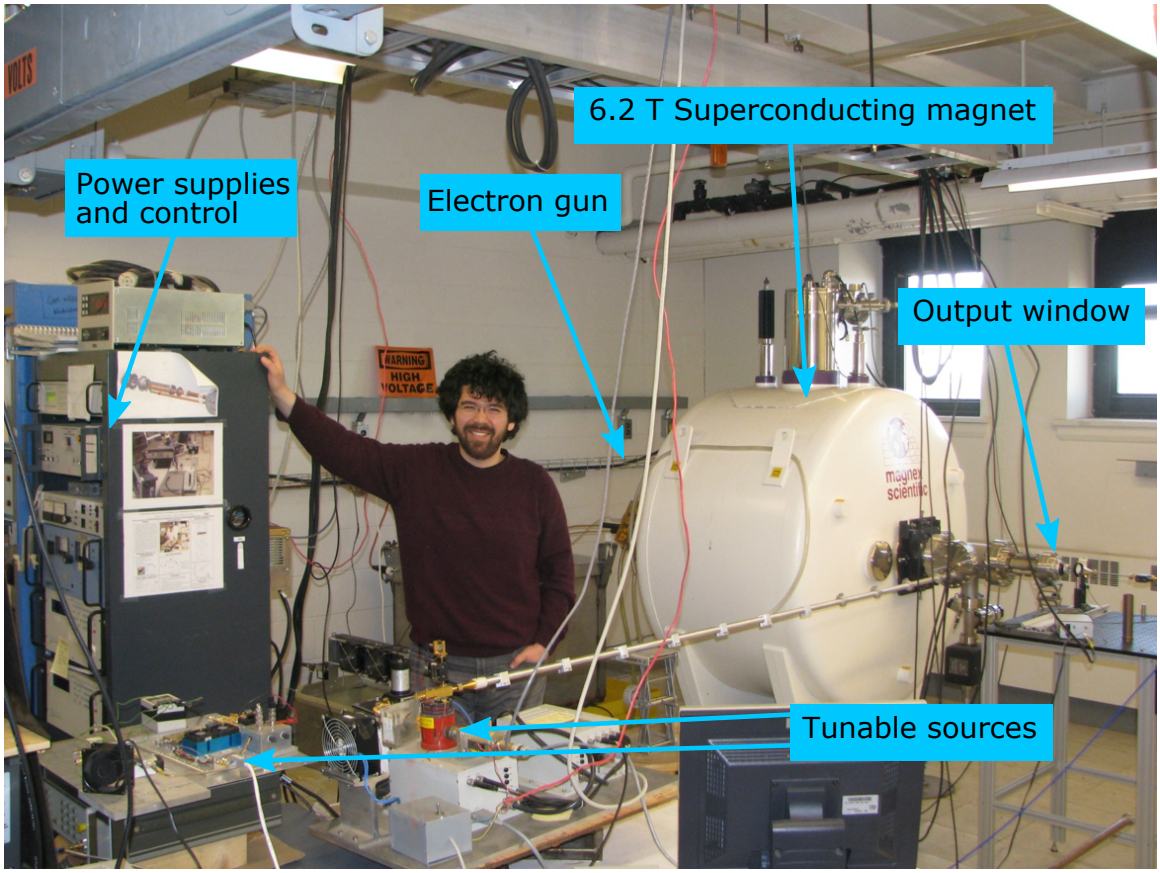

Figure 5-1: The laboratory as setup for the confocal gyro-TWT experiment.

confocal circuit is at the center of the magnetic field. A cross sectional diagram of the vacuum tube is shown in Fig. 5-2. The main elements of the internal components are labelled.

As part of the setup to transport microwave power to the circuit, individual sections of 20 cm corrugated waveguide were manufactured. The 12.7 mm internal diameter waveguides are corrugated with a depth and pitch optimized for 140 GHz microwaves. This was achieved with a trapezoidal tap, the critical dimensions of which are shown in Fig. 5-3.

These waveguide sections were clamped together to create a length of corrugated waveguide over 2.5 m in length. Microwaves are introduced into the vacuum chamber through a 3.28 mm Corning 7940 fused quartz window. This extensive input transmission line setup introduces a loss to the transported microwave power, which in the frequency range of interest (137 to 143 GHz) is about 6 dB in total.

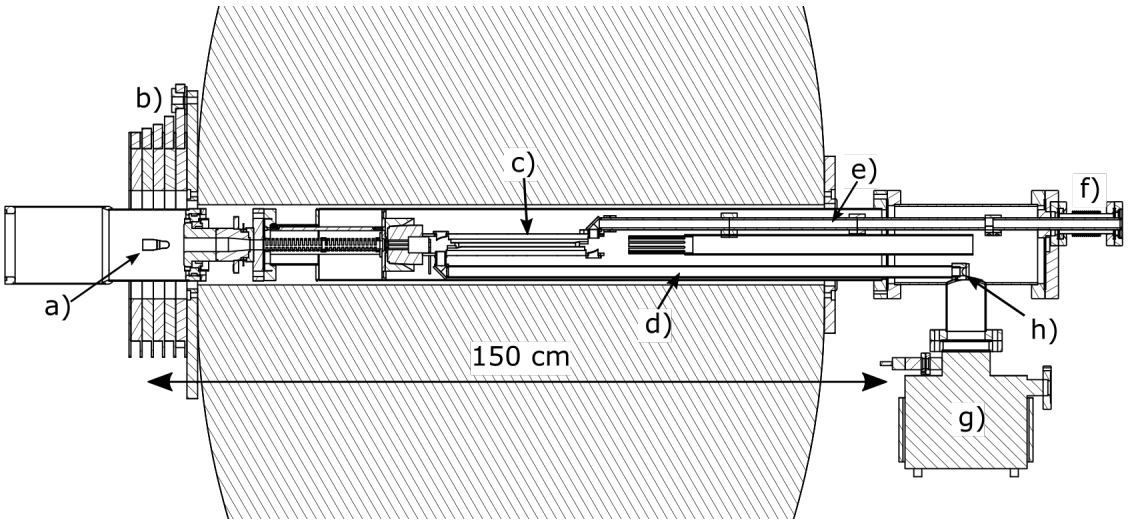

Figure 5-2: A cross section schematic of the confocal system setup is shown, in which a) location of electron gun, b) the gun coil magnet, c) confocal circuit, d) input waveguide, e) output waveguide, f) the output window, g) the ion pump, and h) the location of the input window (axis normal to the page). The tube is housed inside of the 6.2 T superconducting magnet.

It is important that the mechanical and magnetic field axes are aligned because a misalignment would result in the electron beam missing the interaction with the confocal mode. The meter-long system that supports the confocal circuit as well as the input and output corrugated waveguide is inserted horizontally into the vacuum tube and is secured by a taper and clamp arrangement. External alignment is performed by adjusting two 2D stages: one at the gun-end and one at the output-end. This allows for the stainless steel tube to be moved in space, but cannot influence any internal misalignment between the beam tunnel and circuit setups. Therefore, it is important to maintain a parallel setup internal to the vacuum pipe, which is provided by the bracing arms. In order to maintain a straight alignment to the vacuum tube mechanical axis internally, this meter-long system is supported by these stainless steel bracers that are compressed with a spring washer when the tube is assembled. Stainless steel bracer arms are bolted laterally to the confocal circuit and extend to the output conflat flange. The approach of applying a compression force via deforming wing washers (upon closure of the conflat flange) ensures that the tapered alignment nose is fitted securely to its mating collar. A photo showing the stainless steel bracing

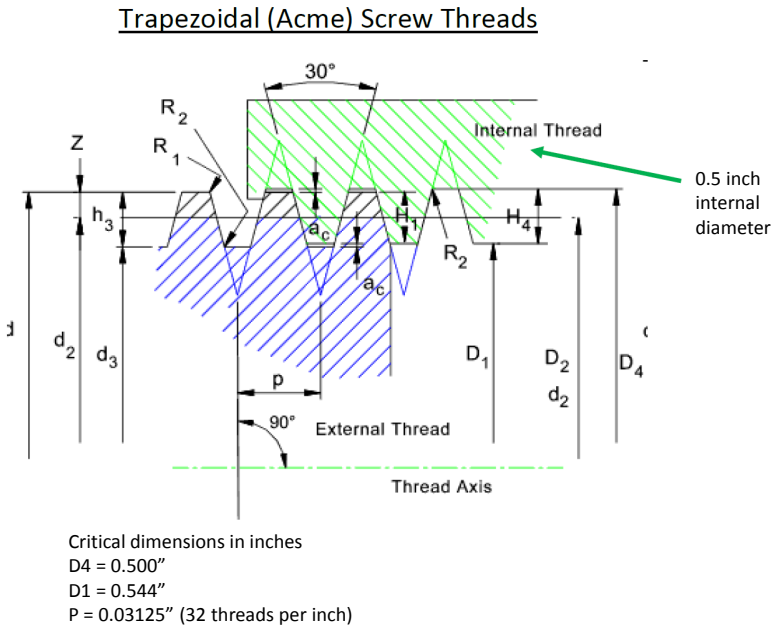

Figure 5-3: The trapezoidal tap dimensions used for fabricating corrugated waveguide sections.

arms, as well as the corrugated waveguide sections, is seen in Fig. 5-4.

The small signal gain of the gyro-amplifier is studied by using a solid state RF driver as an input source to the system. This Virginia Diodes amplifier multiplier chain (AMC) has an output power of about 50 mW over a bandwidth of 138 to 144 GHz. The AMC is able to function as either a continuous wave or as a pulsed source. Saturated gain behavior is studied by using an extended interaction oscillator manufactured by CPI. This source is operated in a pulsed capacity with a pulse width of 2 microseconds over a tunable band of 139.5 to 142 GHz. The output power into the transmission line is about 50 W at its peak and may be varied with an attenuator.

Below, we discuss the corrugated waveguide, superconducting magnet, and the electron gun, as these are external pieces of equipment for the overall experimental setup. We will then proceed to discuss the details of the confocal interaction circuit itself.

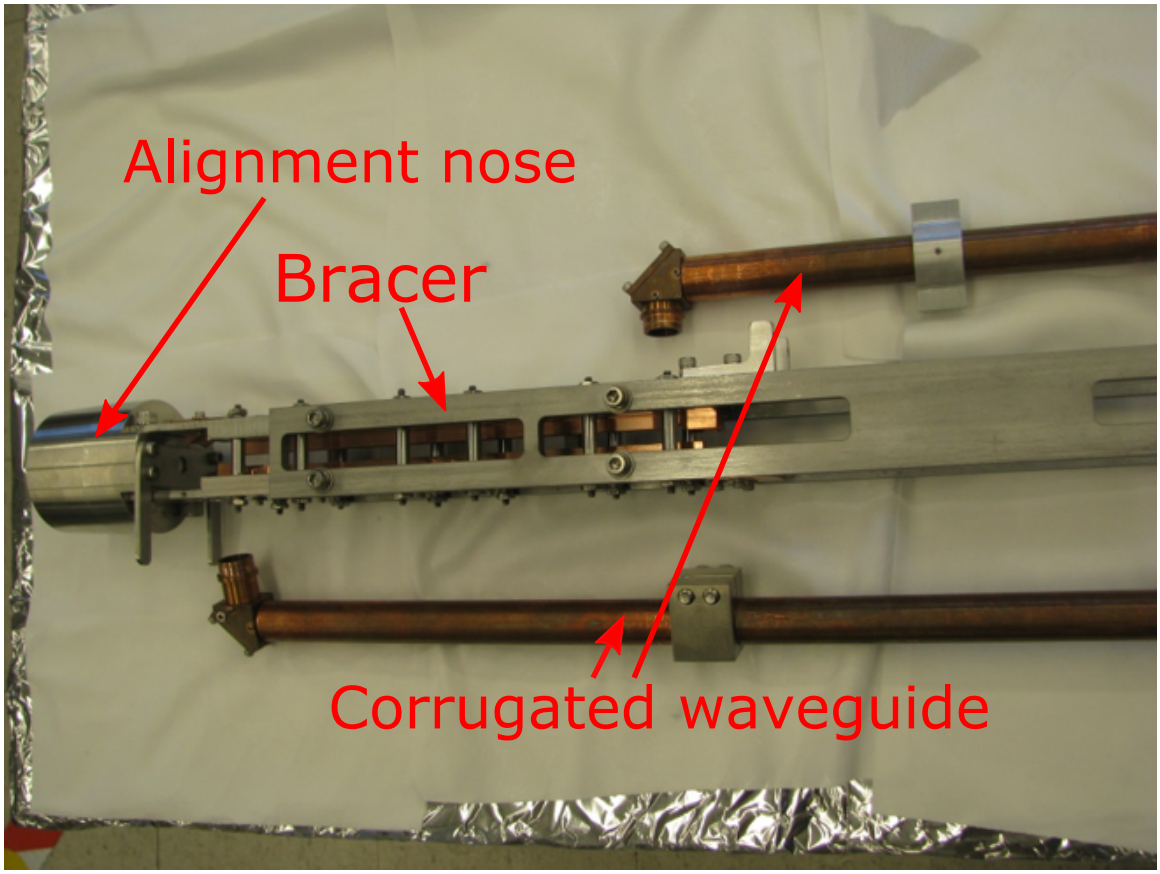

Figure 5-4: The stainless steel bracer arms support the confocal circuit. The copper, corrugated waveguide sections are seen above and below the circuit.

5.1.1 Superconducting Magnet

The superconducting magnet used in this experiment was manufactured by Magnex Scientific, LLC. It has the advantage of having a large bore of 12.7 cm in diameter, which is helpful for installing and aligning the vacuum tube. Additionally, the magnet features a flat top that is 20 cm, to a field variation of $\pm 0.5\%$. Two 2D translation stages are mounted on the ends of the superconducting magnet liquid helium jacket, and provide mechanical alignment for the vacuum tube. A separate, pancake style coil assembly is used to provide a local magnetic field near the electron gun's cathode. This gun coil is water cooled and is capable of 0.11 T at a maximum applied current of 100 A. The current leads are reversible, so the applied magnetic field can be additive or subtractive near the cathode. A detailed description of the magnetic field as well as the results of a direct measurement are discussed in the Appendix A.

5.1.2 Electron Gun and Pulse Forming Network

The gyro-TWT experiment used a CPI triode configuration, non-laminar VUW-8140 MIG gun, with nominal operating parameters of 65 kV and 5.0 A of beam current. These conditions were designed to operate at 5.6 T to produce a pitch factor α of 1.5 and a perpendicular velocity spread of 2.7%. For use as a gyro-amplifier at 140 GHz, the gun was ultimately run at a different operating point of 5.087 T, 48 kV beam voltage, 34 kV mod-anode voltage, a pitch factor of 0.64, and beam current up to 3 A. This operating condition will be described in a future section. The fact that the MIG gun is a triode configuration allows us to tune the pitch factor α by changing the mod-anode ratio. This mod-anode ratio controls the final mod-anode voltage via a resistor bridge. In practice, the resistor bridge comprises twenty separate taps. The mod-anode voltage, V_{MA}, is thus related to the cathode voltage, V_K, as

$$\frac{V_{MA}}{V_K} = -0.00496 N_T + 0.790 \tag{5.1}$$

where N_T is the tap number on the resistor bridge. By a combination of tuning both the gun coil current and the mod-anode tap, different values of α and final beam radius R_g can be explored.

The cathode emitter surface is $R_c = 9.12$ mm. Using the adiabatic relationship given by Eq. 2.1, it is possible to trace the beam radius as a function of axial coordinate z due to the fact that the magnetic field is itself changing, $B(z)$. An example of how $R_g(z)$ behaves is shown in Fig. 5-5.

The beam radius is most affected by the axial position of the emitter as well as the gun coil current. Hence, for where beam radius is concerned, the ability to tune these two parameters is essential in the laboratory setup.

One significant beam parameter that can affect the final gain (and output power) of both gyro-TWTs and gyrotron oscillators is the velocity spread of the electrons [93, 94, 95, 96]. A spread in perpendicular velocities results in some electrons having either too little or too great of a perpendicular velocity component to be bunched successfully for the given RF frequency. Consequently, the net gain suffers. Sources

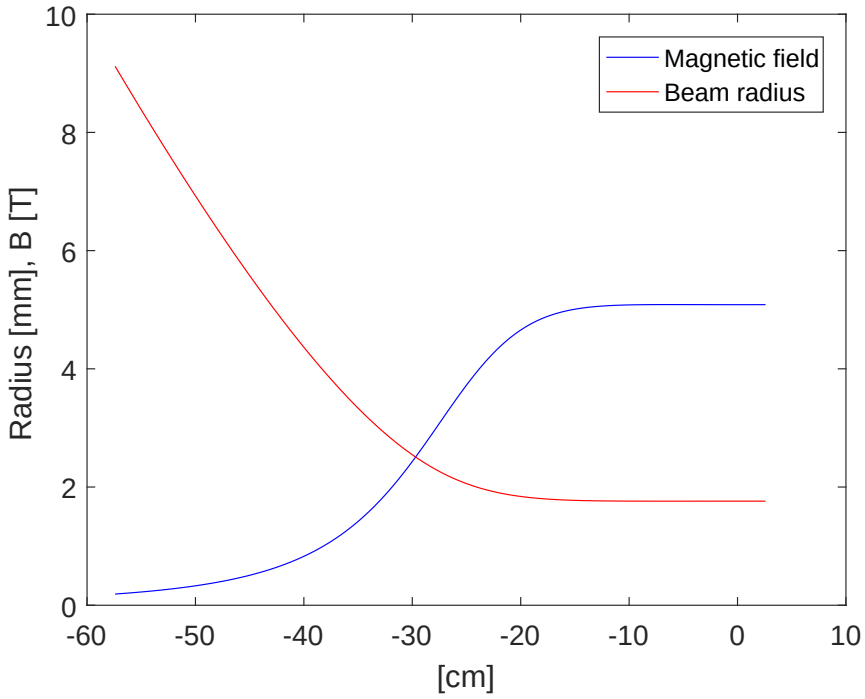

Figure 5-5: The beam radius $R_g(z)$ as a function of axial coordinate z, traced from the cathode position (with $R_g = 9.12$ mm) to the magnet center. The cathode emitter is located about 57 cm from the magnetic field center. At the emitter, the field is 0.19 T and the main flat top field is 5.09 T, giving a compression ratio of about 5 for the beam radii.

of velocity spread include optical (electromagnetic focusing) and material effects. Generally speaking, material effects can be related to surface roughness of the emitter source and thermal variations due to unequal heating of the cathode. Optical effects are due to the chosen electromagnetic operating parameters (cathode voltage, mod-anode voltage, magnetic field, and beam current). The optical effects can be modelled by a particle-tracking code, such as MICHELLE [97]. In fact, the design of MIG guns used for gyrotrons is a critical step in the development of a successful gyrotron. The optical effects are of principle concern in the engineering of these MIG guns [98]. Whereas the optical effects on velocity spread can be minimized by careful gun design, the material effects (due to surface chemistry and gradual aging with usage) are difficult to minimize. A detailed study following the approach taken in [99] was performed on the VUW8140 electron gun. The results are presented in Appendix B.

The electron gun is powered by a pulsed high voltage modulator. This modulator is capable of supplying a flat high voltage pulse to the electron gun up to 65 kV. The modulator itself (as a 6:1 step-up transformer) is driven by a pulse forming network, charged by a Spellman power supply and discharged by a thyratron. The temporal width of the flat top is about 4 microseconds, although the amplification experiments use the central 2 microseconds. Over this 2 microsecond region, the modulator supplies a steady voltage, which is necessary for stable amplification to take place. During experimental operation, both the high voltage and the tube collector current are read simultaneously. Figure. 5-6 shows an example of the data collection scheme when a WR8 diode is used to detect a 140 GHz signal.

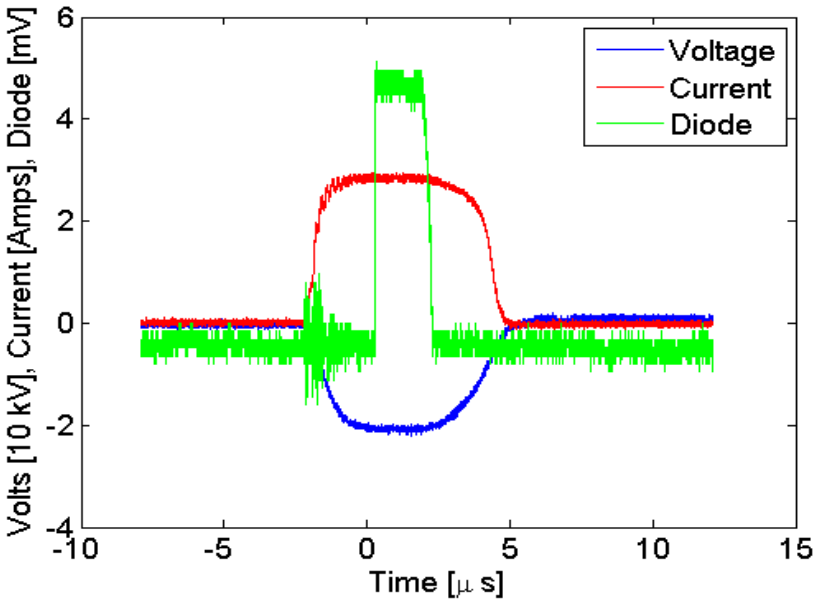

Figure 5-6: Data traces showing voltage, collector current, and diode response. The diode response is seen to correspond at the flat top of the high voltage pulse.

5.2 Mode Converters

The gyro-amplifier experiment features a 12.7 mm diameter corrugated waveguide for transmitting RF power into the vacuum tube. It is necessary to couple power from the HE_{11} mode of the corrugated waveguide into the HE_{06} mode of the confocal circuit.

This is accomplished by using a quasi-optical mode converter with a Vlasov-style design [100]. In total, two separate mode converter designs were ultimately tested. The original hot test of the confocal gyro-TWT lacked any such mode converters. Instead, input power was sent through a fundamental waveguide WR8 directly into the center of confocal rails. The output was collected by a circular uptaper. The circular uptaper ultimately was attached to the collector, which doubled as the output waveguide. This system is shown in Fig. 5-7. Although functional, neither the input nor the output is designed to interact with the HE_{06} mode of the confocal waveguide.

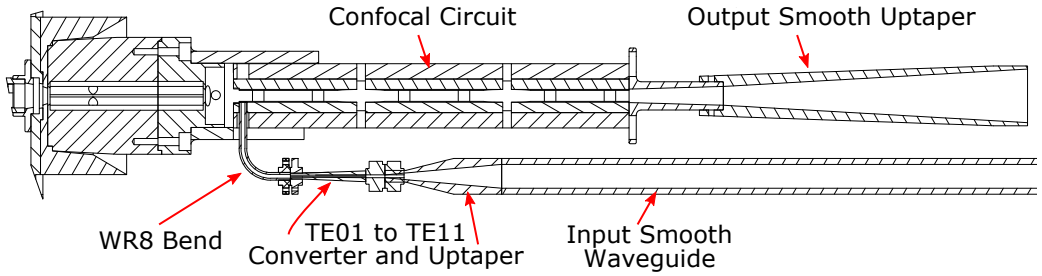

Figure 5-7: A cross sectional view of the input/output setup for the gyro-TWT experiment that features a WR8 bend and a circular uptaper as the input and output schemes, respectively.

This power coupling scheme was the first iteration hot tested during the gyro-TWT study. Although the system performed, there were inherent issues that could be problematic for application to DNP/NMR experiments. Namely, the input downtaper from circular waveguide to fundamental WR8 may cause reflections on the input transmission line. Second, the forceful coupling from HE_{06} to a circular uptaper does not create an ideal output transmission line mode. Moving to a power coupling scheme that uses the aforementioned quasi-optical mode converters was a necessary step in the further enhancement of the gyro-TWT system.

In order to address the power coupling issue, a first generation quasi-optical mode converter was designed and cold tested. This mode converter, as an initial test of the quasi-optical system, was intended to only replace the output circular uptaper, and featured a toroidal focusing mirror as well as an angled steering mirror. The steering mirror redirected output power into an output waveguide, which was now offset from the electron beam trajectory (thus allowing the collector to no longer also

act as an output waveguide). The initial design of the quasi-optical mode converter was oversized, which precluded its adaption as a symmetric input mode converter; therefore, the WR8 input scheme remained. A diagram of how the hot test design fitted to the original confocal circuit is shown in Fig. 5-8.

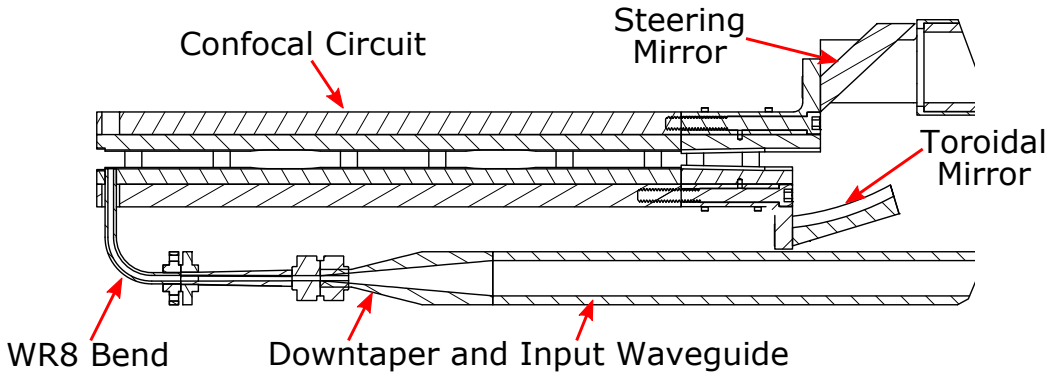

Figure 5-8: A cross sectional view of the hot test design for adapting the first quasi-optical mode converter for use with the existing confocal gyro-TWT system. The output of the confocal waveguide is redirected off-axis from the electron beam trajectory.

The quasi-optical mode converter was cold tested by using a 2D scan in order to probe the output field pattern. For application to DNP/NMR, it is advantageous to work with corrugated waveguide. A gaussian beam couples well to the transmission line mode of a corrugated waveguide, and thus the quasi-optical mode converter is designed to produce an output field pattern that is gaussian. The result of the cold test is shown in Fig. 5-9 along with a numerical prediction from the simulation code HFSS.

The output radiation pattern of the first generation mode converter was seen to match with that of the numerical prediction, although the desired gaussian beam was not measured. Despite this, the agreement between the cold test and simulation held promise for refining the design steps taken during the engineering of the mode converter.

Following the results of the first generation mode converter, it was decided to design new mode converters for both the input and the output of the confocal circuit. This led to the final gyro-TWT system as seen in Fig. 5-2. Importantly, the mode

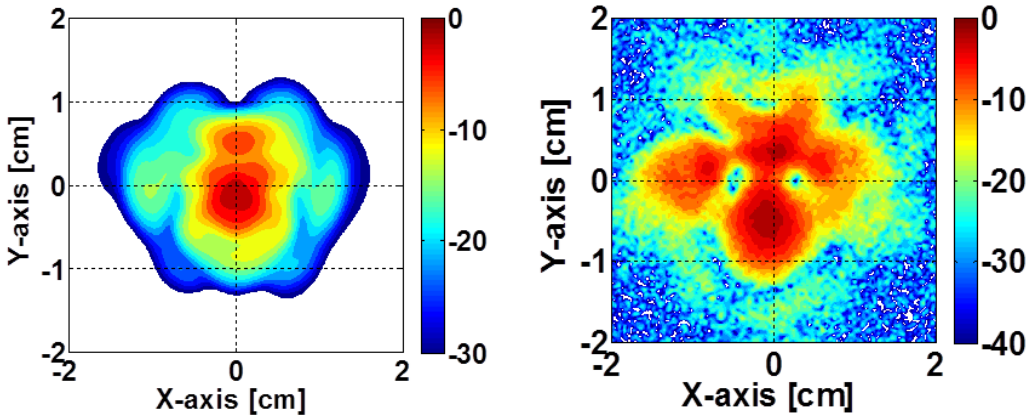

Figure 5-9: A vector network analyzer scan of the output radiation pattern, shown on the right, is compared with the numerical prediction from HFSS, shown on the left. The scale is logarithmic. The experimental result is seen to match reasonably with the numerical prediction.

converter design needed to be more compact in order to allow identical setups to be machined onto a new generation of confocal waveguide. This reciprocal system, with mirrors machined from the same piece of copper as would form the confocal rails, would be integrated into the final confocal circuit. Machining from the same piece of copper as that which forms the rails helps to ensure mechanical alignment of the mode converter to the confocal rails. A scale model of this Vlasov-style mode converter, shown as a cutaway CAD figure in Fig. 5-10, was fabricated and cold tested using a vector network analyzer (VNA). The scale model is identical to the complete structure except that the length of the confocal rails is 3 cm versus 20 cm in the full structure.

The scale cold test model mode converter was fully simulated with the commercial software CST Microwave Studio. A comparison of both the measured (VNA) and simulated (CST) S_{21} parameters is shown in Fig. 5-11. The S_{21} parameter shown is for the entire scale model, calibrated at the waveguide input to the quasi-optical launcher, and therefore includes the losses from both sets of launchers. Good agreement between simulation and measurement indicates a successful fabrication of a quasi-optical mode converter for the confocal HE_{06} mode.

The quasi-optical design furthermore reduces backward reflections in the corru-

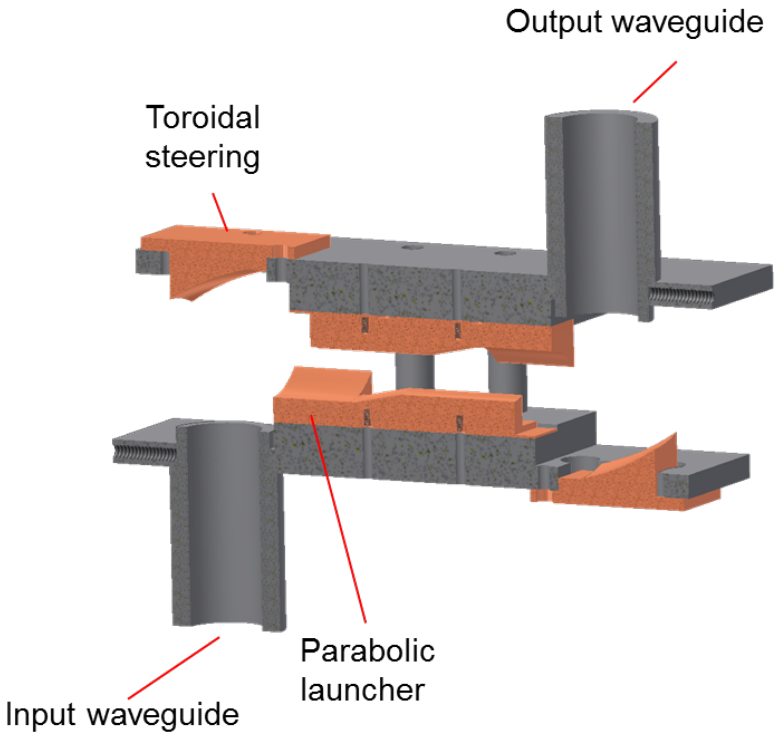

Figure 5-10: A CAD rendering of the cold test mode converter. This model includes integrated parabolic mirrors that were machined as part of the short confocal rail section.

gated transmission line as it avoids the downtaper that a fundamental waveguide WR8 input section would require. This final design was manufactured in a hot test form with the new confocal circuit.

5.3 Suppression of Vacuum Pipe Modes

Throughout the course of this project, it was consistently observed that there exist parasitic oscillations that compete with the operating frequency of $\sim$ 140 GHz. These oscillation frequencies were measured to be around 126.5 GHz, and had a typical starting current of above 1 A at nominal operating voltages. The existence of these parasitic oscillations went against the understanding that the open geometry of the confocal waveguide would suppress competing modes, such as the HE_{15} mode. Additionally, the fact these parasitic oscillations competed directly with the operat-

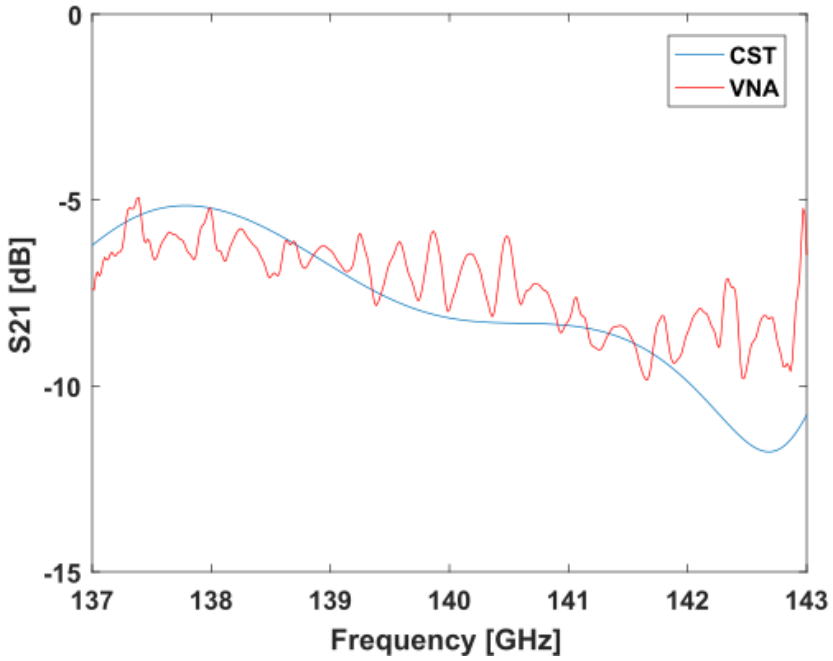

Figure 5-11: The S_{21} parameter shown for both the measured (VNA) and simulated (CST) results. Good agreement is seen between measurement and numerical simulation.

ing frequency meant that experimental studies of gain were limited in beam current. Because the small signal gain is proportional to $I^{(1/3)}$, achieving high gain even at optimal operating parameters was restricted due to the fact that the beam current was necessarily small. Figure. 5-12 shows the characteristic $I^{(1/3)}$ behavior of the small signal gain measured using the second generation confocal circuit at an operating condition of 5.085 T, 44 kV, and 140 GHz, as a function of beam current. A functional fit to the gain versus beam current behavior indicates that if the current were able to be higher that the gain would reach at least 30 dB. A new understanding needed to be discovered that would enable a design change to the gyro-TWT system in order to eliminate the competing parasitic oscillations.

Numerical studies performed in CST Microwave Studio showed that the interior wall of the vacuum chamber that houses the confocal circuit supported vacuum pipe modes that coupled back into the interaction region of the confocal geometry at frequencies measured during the hot test. In order to suppress these vacuum pipe modes, the dielectric ceramic Macor was added into the vacuum tube on the flanks

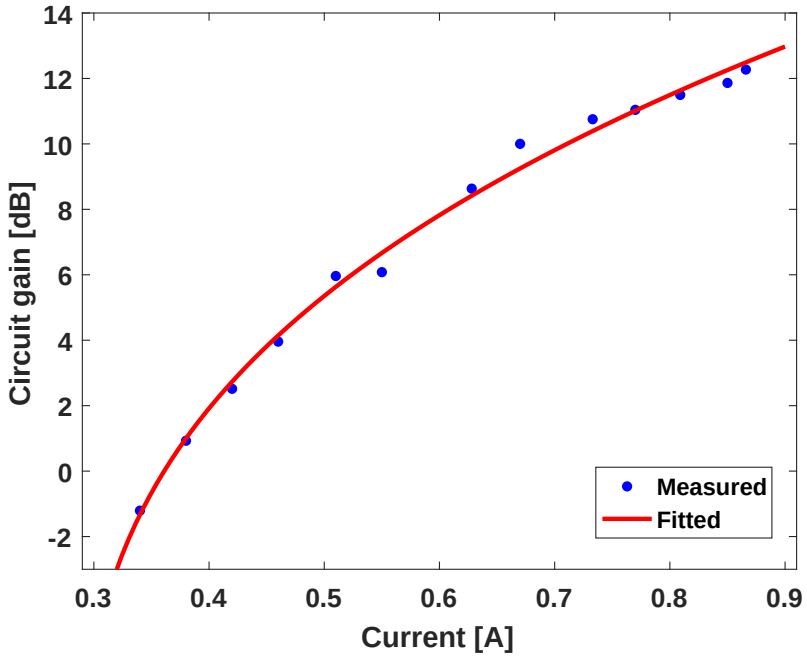

Figure 5-12: The small signal gain versus beam current. The gain versus current is fit to an $I^{(1/3)}$ dependence, and when extrapolated to 3 A the gain reaches 30 dB. The operating point is 5.085 T, 44 kV, α of 0.63, and 140 GHz. This indicates that it is advantageous to use higher beam current.

of the confocal structure. Fig. 5-13 shows the computed spatial mode pattern for a 126.5 GHz eigenmode of the entire cross section of the vacuum tube, including the vacuum tube inner walls and the confocal structure, with and without the inclusion of the Macor dielectric.

The addition of Macor bars creates an absorptive loss, which supplements the diffractive loss mechanism of the confocal geometry. A Q factor was computed by CST Microwave Studio for the vacuum pipe modes with and without the Macor bars. As shown in Table I, the Macor bars significantly dampen the quality factor of the vacuum pipe modes and help to prevent these parasitic oscillations at unwanted frequencies.

The inclusion of these Macor bars led to zero-drive stable operation at beam currents above 2 A and operating voltages above 30 kV. This is a requirement for successful amplifier operation at 140 GHz and for application to DNP/NMR systems.

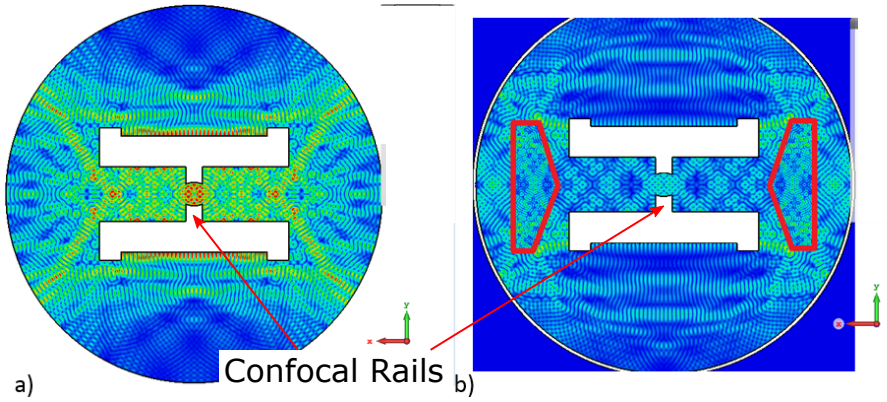

Figure 5-13: a) 126.5 GHz mode of the entire volume of the vacuum pipe without Macor bars. The vacuum pipe wall supports a mode that has strong fields at the confocal interaction region (located at the center of the simulation and as indicated by the arrows). b) The 126.5 GHz mode is seen to be suppressed by the addition of Macor bars (shown in red). These plots are on a linear scale with red showing the location of the highest E field values.

Frequency	Q no Macor	Q with Macor
126.1 GHz	2.9e4	450
126.2 GHz	4e4	480
126.5 GHz	3e6	170

Table 5.1: Quality factors computed for several spatial modes of the vacuum pipe.

5.4 Design Goals

In this section, we begin the discussion of the second generation of the confocal interaction circuit, and how it applies to the amplification of pulsed millimeter waves for use with pulsed DNP/NMR. Previously mentioned work has demonstrated the suitability of gyro-devices as a power source for high-field DNP spectroscopy experiments. As we know, fixed-frequency, continuous-wave gyrotron oscillators have been in service at the Francis Bitter Magnet Lab (FBML) at 140, 250, and 460 GHz. It is desired to develop a pulsed, phase-controlled amplifier centered at these frequencies for use in pulse DNP/NMR experiments. The application to DNP/NMR sets the experimental design goals, listed in Table 5.2.

Output Power	> 500 W
Bandwidth	> 1 GHz
Center Frequency	140 GHz

Table 5.2: The design goals of the 140 GHz gyro-TWT experiment.

5.5 Experimental results of first generation confocal circuit with severs

The confocal gyro-TWT underwent hot testing on the original system setup, which is shown in 5-7. This generation of confocal circuit, shown schematically in Fig. 5-14, is 21 cm in length (three sections of 5 cm confocal rails). The width of these rails, also known as the aperture ($2a$), is 5 mm. It features two severs of length 3 cm with a minimum aperture of 0.74 mm, cut directly into the confocal rails.

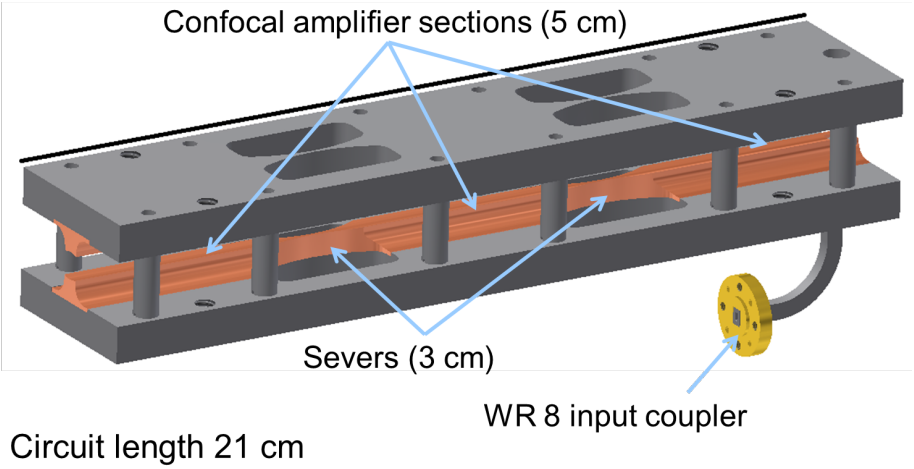

Figure 5-14: The first generation confocal circuit.

During the hot test of this initial setup, a large parameter space was explored. Ultimately, the gyro-TWT was found to have a peak output power at a magnetic field value of 5.182 T. At this field value, using a combination of the EIO and the VDI solid state source, the gain saturation was studied. Figure 5-15 shows the gain saturation behavior at 5.182 T, 40 kV, α of 0.54, and a beam current of 2.4 A, with a peak output power of 875 W, which corresponds to a device gain of about 12.5 dB. The high power point was measured at 139.7 GHz.

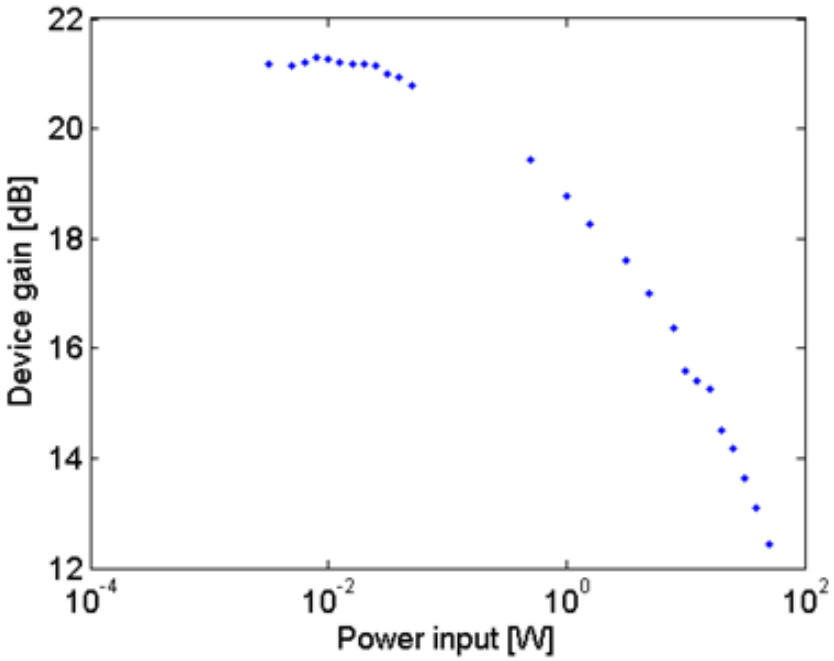

Figure 5-15: The gain saturation behavior for the first generation confocal circuit, as measured at 5.182 T, 40 kV, 2.4 A of beam current, and an operating frequency of 139.7 GHz. The peak output power of 875 W corresponds to a device gain of about 12.5 dB.

Of interest to DNP/NMR is the small signal gain, which would be used to amplify a pulse train from a solid state source. Therefore, the parameter space was scanned to optimize for the peak small signal gain. Figure 5-16 shows the gain bandwidth at a magnetic field of 5.05 T and 27 kV. The beam current was limited to 1.3 A in order to prevent oscillations.

The magnetic field was also taken to a higher field value. At 5.17 T, 40 kV, and a beam current of 1.5 A, the circuit gain was recorded near 30 dB. This is shown in Fig. 5-17.

The first generation confocal circuit demonstrated a peak output power of 875 W at 139.7 GHz. This achievement was the highest recorded output power measured during experimentation with the confocal gyro-TWT, and is a promising step towards high-power amplification. Circuit gain at about 30 dB near 139.4 GHz was observed. In conjunction with the hot test of the first generation confocal gyro-TWT, several improvements were underway. These included the installation of the aforementioned

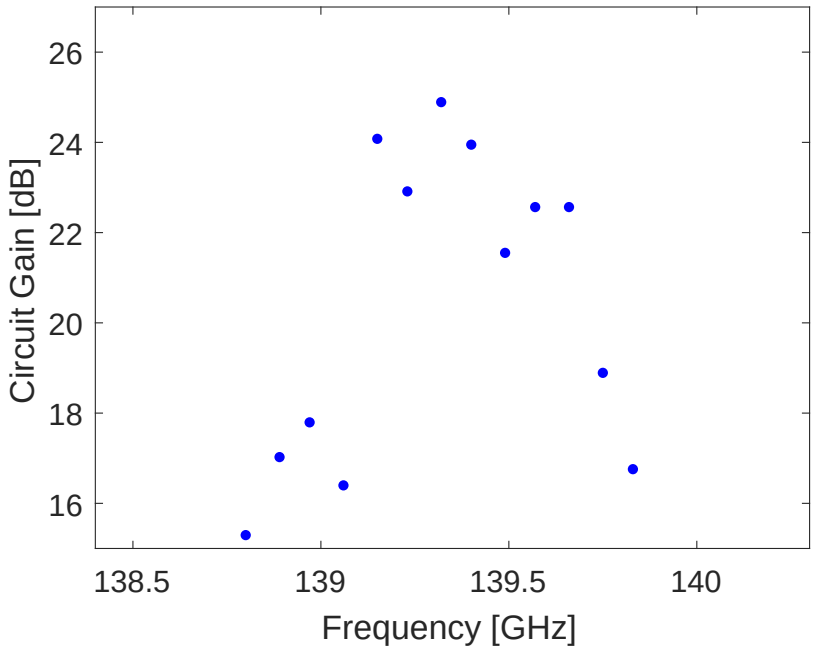

Figure 5-16: The small signal circuit gain for the first generation confocal circuit at an operating point of 5.05 T, 27 kV, α of 0.45, and a beam current of 1.3 A. The 3 dB bandwidth at this operating point is about 400 MHz.

corrugated waveguide, the design of quasi-optical mode converters, and the redesign of the confocal circuit itself. A discussion of the new confocal redesign follows.

5.6 Severless confocal circuit design

Work performed during the initial hot test of the gyro-TWT revealed that some improvements were possible. The quasi-optical mode converters, previously discussed, comprised such an improvement. It was desired to revisit the design of the confocal circuit itself. Key design decisions when constructing a confocal interaction circuit are the rail spacing, length of circuit, and rail width (the rail curvature is set by the condition that the radius equals the spacing). The interaction circuit is a 20 cm set of copper rails arranged with the confocal geometry described, the length chosen to be within the flat top extent of the superconducting magnet's field. The design elements that were changed are the radius of curvature of the confocal rails and their width. For the second generation circuit, the radius of curvature, equal to their separation,

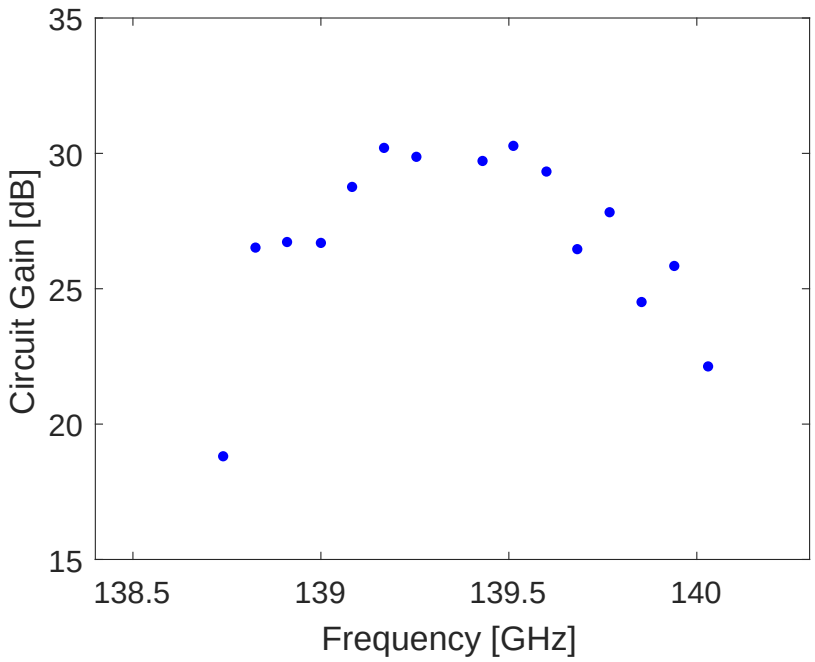

Figure 5-17: The small signal circuit gain for the first generation confocal circuit at an operating point of 5.17 T, 40 kV, α of 0.54, and a beam current of 1.5 A. The bandwidth is about 600 MHz, with a peak of 30 dB around 139.4 GHz.

is 6.83 mm. The loss per distance for each confocal mode depends on the width of the rails. The aperture of these rails is 4.3 mm, which at 140 GHz provides about 4 dB/cm of attenuation due to diffractive losses. A cutaway schematic showing the detailed arrangement of the confocal rails along with the reciprocal input/output mode converters is shown in Fig. 5-18.

The rail spacing determines the cutoff frequency for each mode. The cutoff frequency is a design variable that is used in conjunction with the electron gun operating parameters in order to give a good tangential grazing condition on the dispersion diagram. At a rail spacing of 6.83 mm, this cutoff is 137.3 GHz for the HE_{06} mode. As previously mentioned, the dispersion relations for the waveguide mode and the electron beam may be written as follows:

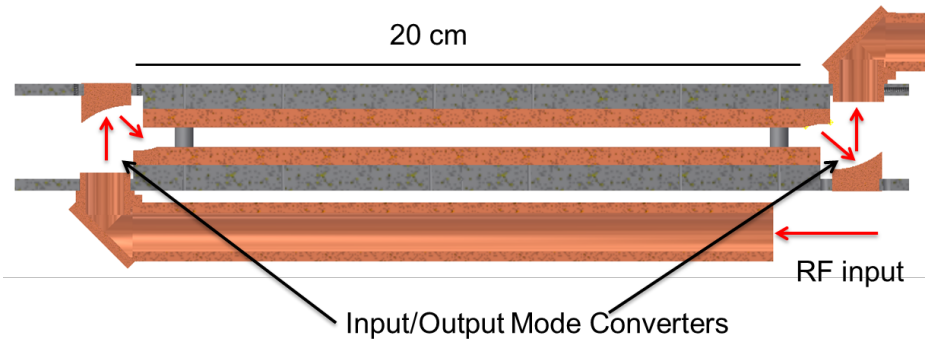

Figure 5-18: The confocal circuit was fabricated with integral input/output mode converters. The launchers were machined from the same bar of copper that was used to cut the confocal rails, a design feature that improves mechanical alignment.

$$\omega^2 - k_z^2 c^2 - k_\perp^2 c^2 = 0 \tag{5.2}$$

$$\omega - \Omega/\gamma - k_z v_z \geq 0 \tag{5.3}$$

where k_z and $k_\perp$ are the components of the wavevector, ω is the angular frequency, $\Omega = eB_o/m_e$ is the cyclotron frequency, and γ is the relativistic factor. In Ω, e is the electron charge, B_o is the magnetic field, m_e is the electron mass. We note that the dispersion relations experimentally depend on the magnetic field, the beam voltage, and the pitch factor $\alpha = v_\perp/v_z$. Gain occurs when the dispersion curves described by Eqs. 5.2 and 5.3 are near intersection. The ability to experimentally tune laboratory parameters such as beam voltage and magnetic field, as well as the choice of a waveguide cutoff by mechanical design, allow the possibility to engineer an interaction circuit to amplify at a desired frequency range. With a cutoff of 137.3 GHz, we can achieve a tangential grazing condition with a set of operating parameters obtainable in the laboratory. This can be shown visually in Fig. 5-19.

The principle mechanical design parameters of the severless confocal circuit are summarized in Table 5.3.

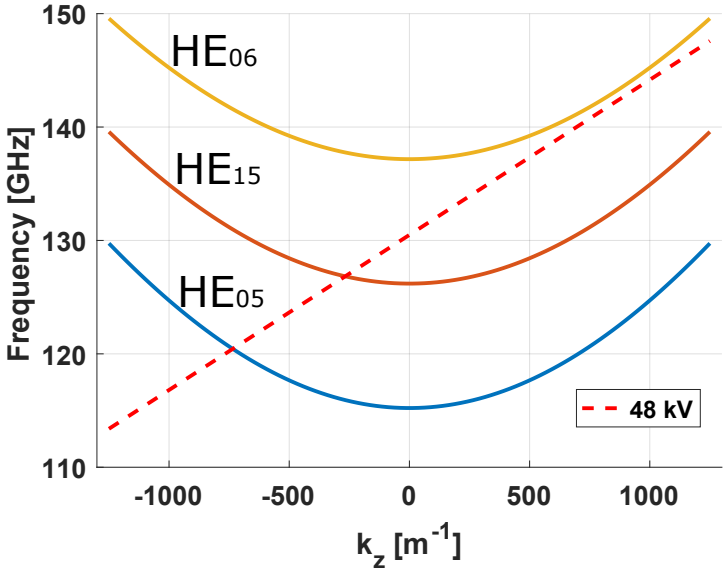

Figure 5-19: The dispersion curves, given by Eq. 5.2, are plotted for three modes (HE_{06}, HE_{15}, HE_{05}) of a confocal waveguide. Also plotted is the electron beam line given by Eq. 5.3. The parameters of the plot are typical for the present experiments with $B_0 = 5.087$ T, beam voltage of 48 kV, pitch factor $\alpha = 0.64$, and confocal rail spacing of 6.83 mm. The electron dispersion line is tangential to the waveguide mode curve around 140 GHz. The intersection of the electron beam line with the backward wave curves of the HE_{15} and HE_{05} modes indicates a potential source of parasitic oscillations that needs to be suppressed.

5.7 Experimental Results of Severless Confocal Circuit without Dielectric Loading

Losses in the gyro-amplifier system mean that the actual confocal circuit interaction needs to produce a high gain in order to achieve a high power for small signal amplification. The main sources of loss are the transmission waveguide and window setup as well as the reciprocal input/output quasi-optical mode converters. At 140 GHz, the total loss due to the sum of input and output coupling is about 12 dB, which is the offset when comparing device and circuit gain, the latter of which may be predicted using numerical simulations.

The numerical code MAGY was used to simulate gain in the confocal circuit [90]. At 5.08 T, 46 kV, 3 A of beam current and a pitch factor α of 0.8, a circuit gain of about 50 dB is predicted, provided that perpendicular velocity spread is low at 3%.

Length	20 cm
Rail width	4.3 mm
Rail spacing	6.83 mm

Table 5.3: Design parameters for the severless confocal circuit.

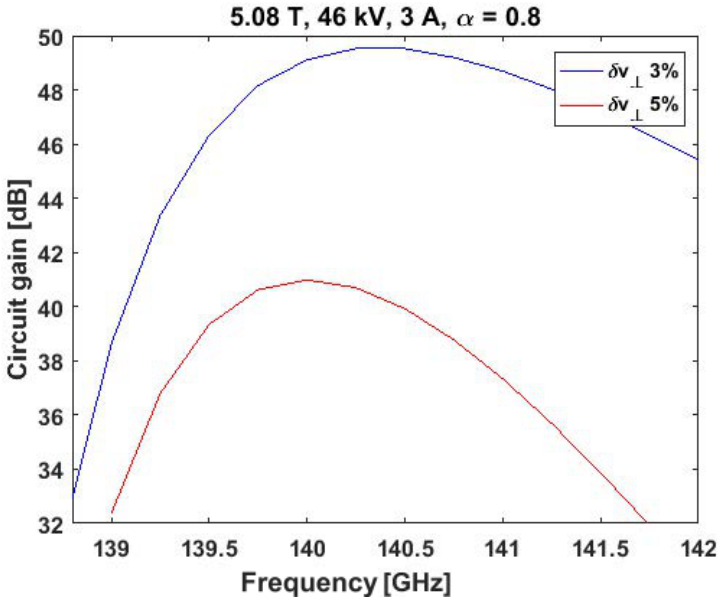

Figure 5-20: Simulated gain bandwidth results from the numerical code MAGY for the case of two different velocity spreads. A drop in simulated peak circuit gain due to a slight increase in velocity spread demonstrates the importance of good electron beam quality. These simulation results are for an operating point of 5.08 T, 46 kV, 3 A, and $\alpha = 0.8$.

Figure 5-20 shows the effect of an increase in perpendicular velocity spread from 3 to 5%. A drop in the simulated peak circuit gain from 50 to 40 dB due to an increase in the velocity spread illustrates the sensitivity of amplifiers to electron beam quality.

As previously mentioned, during initial hot tests of the gyro-amplifier, parasitic oscillations in the range of 126.5 GHz were observed at operating voltages around 45 kV and beam current of 1 A. In order to achieve high gain, operation around this voltage and a higher current of 3 A are desirable. Prior to the installation of Macor bars, the gyro-TWT was hot tested to find regions of high gain performance. Experimentally, there are several parameters that may be adjusted. These are the magnetic field, the cathode voltage, the mod-anode voltage, the gun coil current, axial

tube alignment (as offset from the magnet's center), and beam current. Ultimately, the beam current was increased to 3 A; however, during the initial hot tests, the beam current was kept lower, near 1 - 1.5 A, in order to avoid parasitic oscillations. The values explored are listed in Table. 5.4.

Parameter	Range
Magnetic Field	4.95-5.12 T
Cathode voltage	25-50 kV
Mod-anode radio	0.69-0.78
Gun coil current	0 - 100 A
Axial position	$\pm 1.5cm$
Beam current	1 - 3 A

Table 5.4: Range of explored operating parameters.

The extensive search throughout this large operating space was optimized to find the peak output power of the system at 140.0 GHz using the EIO as an input, with a fixed beam current of about 1.3 A. By adjusting the experimental parameters, the space of possible operating conditions was reduced. This is shown as a plot of output power versus magnetic field in Fig. 5-21, where for each magnetic field value the remaining experimental parameters (beam voltage, mod-anode ratio, gun coil current, and axial tube position) were explored.

Experimentally, adjusting the magnetic field is the most difficult laboratory procedure, due to the design of the superconducting magnet. The fine adjusting of all experimental parameters (including the magnetic field) is best performed when a reasonable magnetic field range is acquired. It is seen that the gyro-TWT performs the best near 5.08 T. Varying the operating parameters at 5.085 T produced gain bandwidths both close to cutoff as well as near the design frequency of 140.0 GHz, as seen in Fig. 5-22. For operating voltages of 37 kV and 45 kV, the beam current was necessarily low at about 1.2 A in order to avoid parasitic oscillations. Although the frequency band of interest could be accessed, namely around 140 GHz, the low current prevented access to higher small signal gain. Similarly, the higher gain seen at 37 kV is due to the fact that the bandwidth is closer to cutoff. This behavior was

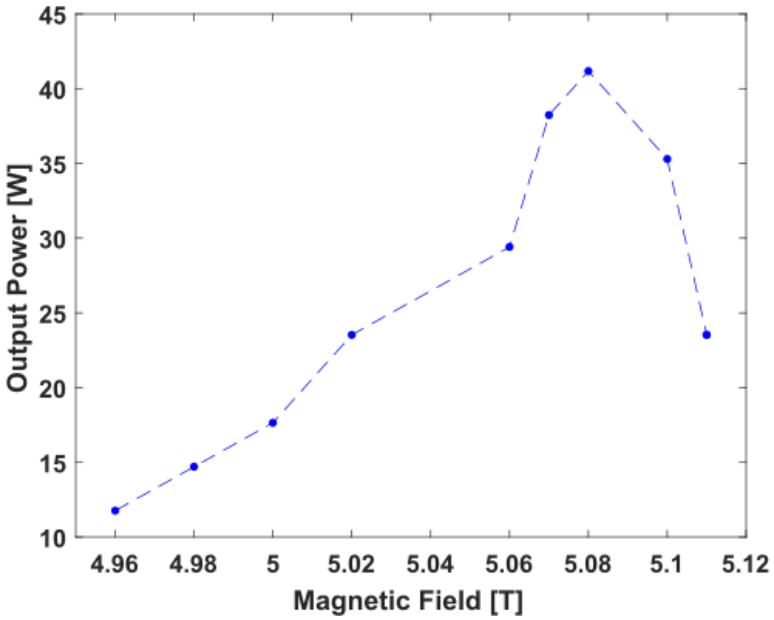

Figure 5-21: The output power from the gyro-TWT at a fixed beam current shown versus optimized experimental parameters at different magnetic fields.

reproduced after the discovery of vacuum pipe modes and the installation of Macor bars to suppress them.

Studies were also performed at magnetic fields not close to 5.08 T, in order to observe the effect on the gain bandwidth. In particular, Fig. 5-23 shows the gain bandwidth at an operating condition of 5.11 T, 47 kV, and a beam current of 1.7 A.

Likewise, at a lower magnetic field the gain bandwidth was seen to perform not as well. At a magnetic field value of 5.05 T, with 44 kV and 1.7 A of beam current, the circuit gain was not optimal, as seen in Fig. 5-24.

5.8 Results of Severless Circuit with Dielectric Loading

Although it was possible to operate the gyro-TWT at lower magnetic field values, the optimum magnetic field was experimentally found to be close to 5.085 T. Unfortunately, using a higher beam current was restricted by oscillations. Clearly, it

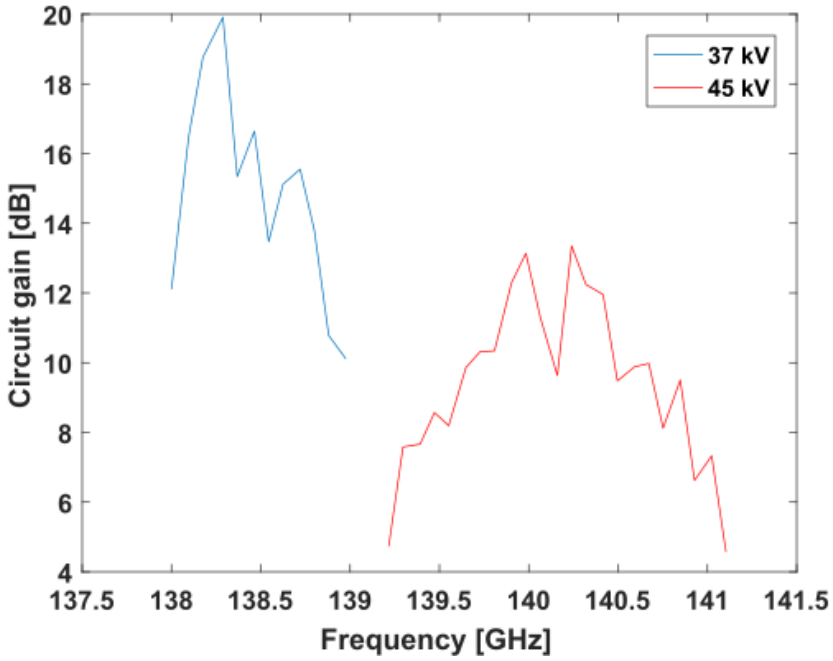

Figure 5-22: Gain bandwidths at the optimum magnetic field of 5.085 T. Changing the operating voltage shifts the bandwidth curve. The beam current in both cases was set at 1.2 A. At 37 kV, α is 0.55 and at 44 kV, α is 0.65.

was necessary to be able to increase the beam current while maintaining a zero-drive stable condition. As has been seen, the addition of Macor bars allowed for zero-drive stable operation at the target voltage and beam current, in which the parasitic oscillations were suppressed by the mechanism described in Section 5.3. This allowed for the beam current to be increased to 3 A. Using the original magnetic field choice of 5.08 T, the hot test of the gyro-TWT after the installation of Macor bars was designed to optimize for gain performance at 140.0 GHz. The electron gun code MICHELLE calculates a pitch factor α of 0.60 at the design operating point at 5.08 T. The experimental data and numerical calculation are shown in Fig. 5-25 for the operating point of 5.08 T, 46 kV, 3 A, and α of 0.60. The peak gain is measured at 139.4 GHz and is about 35 dB of circuit gain or 23 dB device gain. Agreement between experiment and numerical simulation using MAGY is achieved when perpendicular velocity spread is at 6%.

The results in Fig. 5-25 were optimized for 139.4 GHz. For optimization at 140.0

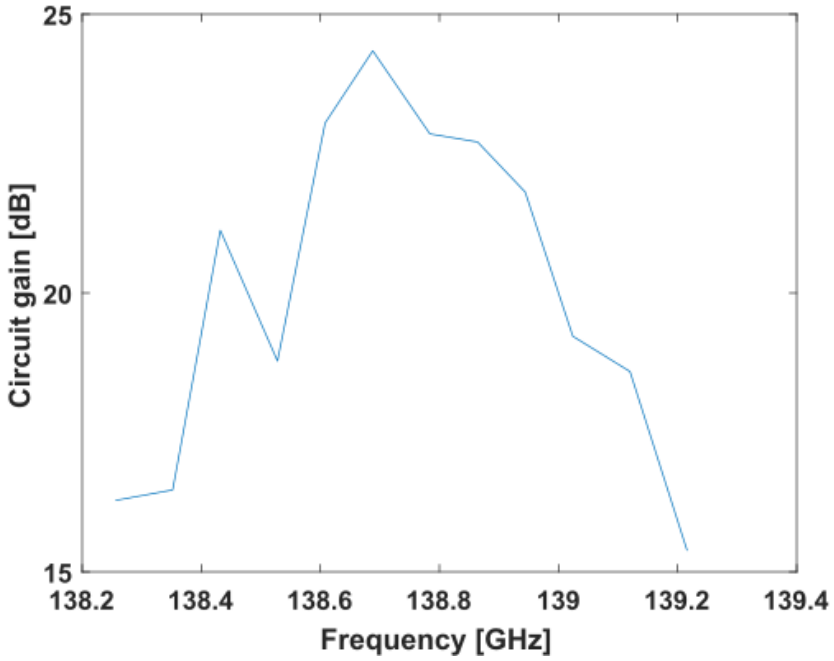

Figure 5-23: The gain bandwidth at 5.11 T, 47 kV, α of 0.67, with a beam current of 1.7 A. The gain peaks at about 138.7 GHz and 25 dB of circuit gain. The bandwidth itself is limited at close to 400 MHz.

GHz, the operating point was adjusted slightly to 5.087 T, 48 kV, and 3A of beam current. At this operating point, a peak circuit gain of about 35 dB (or 23 dB device gain) was measured at 140 GHz with a 3 dB bandwidth of 1.2 GHz. This measured gain bandwidth is shown in Fig. 5-26. At this operating point, the numerical electron gun code MICHELLE predicts a pitch factor α of 0.64. Given a perpendicular velocity spread of 6%, MAGY predicts a good agreement with the measured gain.

It is noted that the value of α is relatively low. Altering the operating point to explore a slightly lower magnetic field produced a gain bandwidth shown in Fig. 5-27. Although the circuit gain is 34 dB, α has a lower value at 0.57 and the velocity spread is still at 6%.

The saturated gain characteristics of this high gain operating point at 5.087 T were also explored. Figure 5-28 shows a comparison of measured to simulated saturated gain behavior. At the high gain operating point the output saturated power reaches about 550 W at 140.0 GHz with an input power of about 2 W and a circuit gain of about 24 dB.

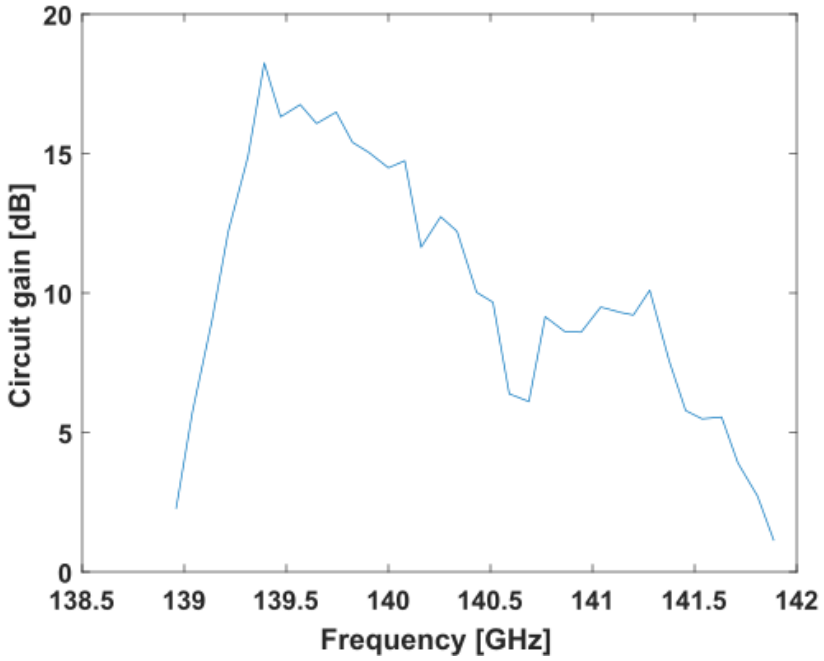

Figure 5-24: The gain bandwidth at 5.05 T, 44 kV, α of 0.64, with a beam current of 1.7 A. The gain peaks at about 139.4 GHz and about 18 dB of circuit gain. The bandwidth at this operating point is about 800 MHz.

As noted previously, it is possible for the gain to be higher near the waveguide's cutoff. With a higher beam current of 3 A, and an operating voltage of 38 kV, a gain bandwidth near the cutoff frequency was measured and is shown in Fig. 5-29. A simulation comparison with MAGY is shown to come closer to agreement at frequencies higher away from cutoff. It is not known why the program MAGY differs from the experimental results near cutoff.

Although this peak gain is about 40 dB at 137.9 GHz, this is not near the design frequency of 140.0 GHz. Nevertheless, it is a good demonstration of higher circuit gain near a waveguide's cutoff.

5.9 Conclusions on Experimental Setup and Results

We have reviewed the major components of the gyro-TWT, such as the superconducting magnet, the electron gun, and transmission line setup. Subsequently, we discussed the designs of the confocal interaction circuits that were tested during this

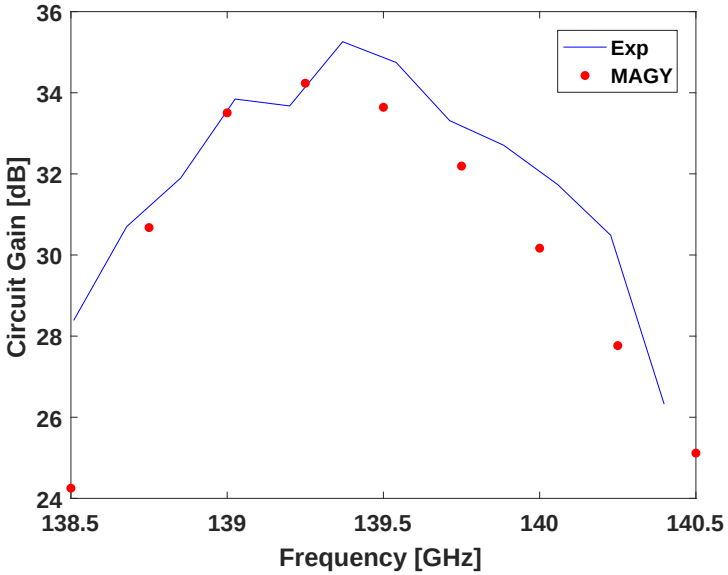

Figure 5-25: Zero-drive stable gain bandwidth is shown as the blue line with a peak of about 35 dB at 139.4 GHz. Good agreement is seen with a MAGY simulation at a velocity spread of 6%. These are the experimental results for the operating point at 5.08 T, 46 kV, 3 A, and $\alpha = 0.60$.

project. Based on the conclusions from the initial hot test of the first generation confocal circuit, it was decided to implement several improvements to the gyro-TWT system. The improvements reviewed in this chapter were the corrugated waveguide, the quasi-optical mode converters, and a redesign of the confocal circuit. Ultimately, a comprehensive study of the second generation confocal gyro-TWT was performed. This confocal circuit, with its attached quasi-optical mode converters, was successfully hot tested.

Using a newly designed set of reciprocal input/output quasi-optical mode converters, the confocal gyro-amplifier has demonstrated a peak circuit gain of 35 dB at 140 GHz with a bandwidth of 1.2 GHz. At this same operating point, the saturated output power at 140 GHz was measured at about 550 W. The measurements were performed under zero-drive stable conditions, necessary for application to DNP/NMR. Vacuum pipe modes were identified and simulated successfully using CST Microwave Studio. The inclusion of dielectric Macor bars in the vacuum tube reduced parasitic oscillations, which enabled this zero-drive stability. The discovery of the vacuum pipe

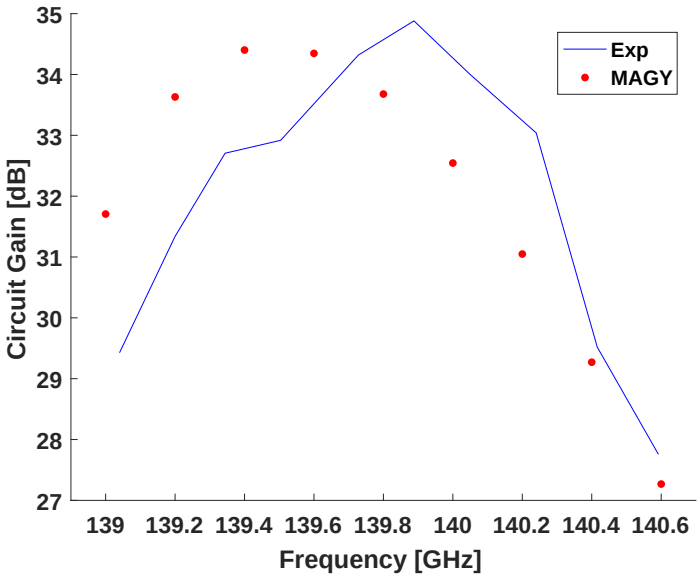

Figure 5-26: Zero-drive stable gain bandwidth is shown as the blue line with a peak of 35 dB at 140.0 GHz. Good agreement is seen with a MAGY simulation at a velocity spread of 6%. These are the experimental results for the operating point at 5.087 T, 48 kV, 3 A, and $\alpha = 0.64$.

modes is an important result of these experiments. Despite the fact that the vacuum tube itself is large compared to the operating wavelength, spatial modes supported by the inner walls of the vacuum tube may exist that interact with the electron beam. The potential for such an interaction to occur is in principle possible for any systems that rely on an open geometry as the choice for a circuit waveguide.

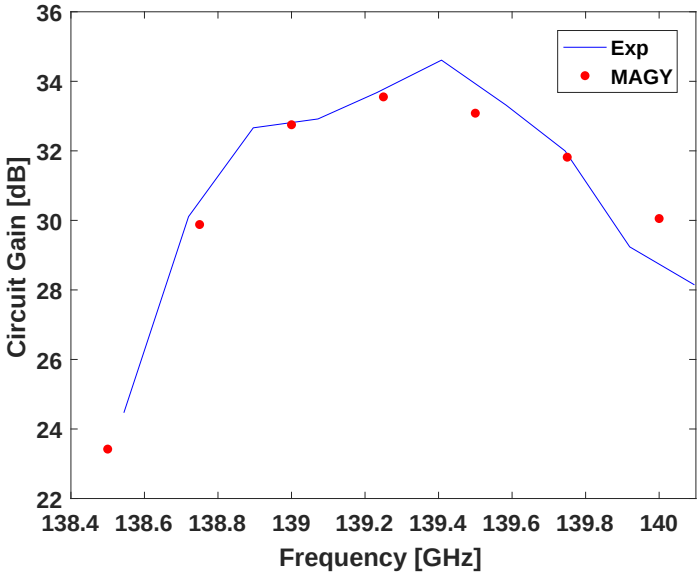

Figure 5-27: Zero-drive stable gain bandwidth is shown as the blue line with a peak of 34 dB at about 139.4 GHz. Good agreement is seen with a MAGY simulation at a velocity spread of 6%. These are the experimental results for the operating point at 5.075 T, 45.5 kV, 3 A, and $\alpha = 0.57$.

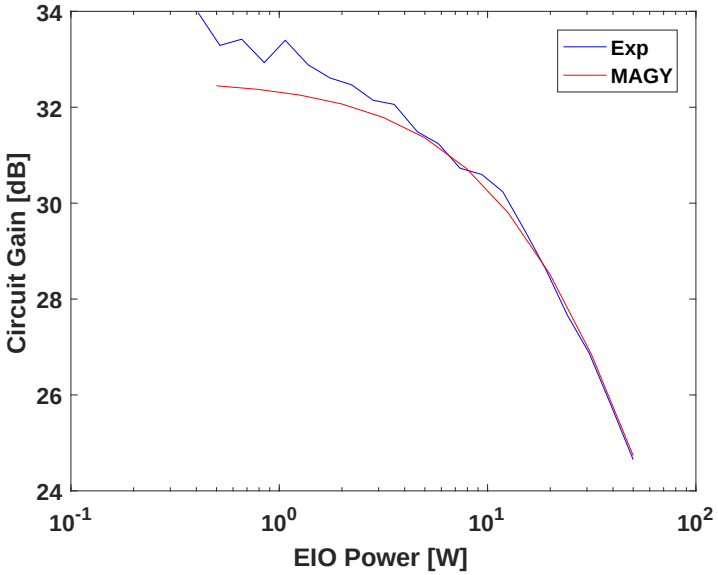

Figure 5-28: The measured saturated gain at 140.0 GHz is shown compared to numerical simulation using MAGY. These are the saturation results for the operating point at 5.087 T, 48 kV, 3 A, and $\alpha = 0.64$.

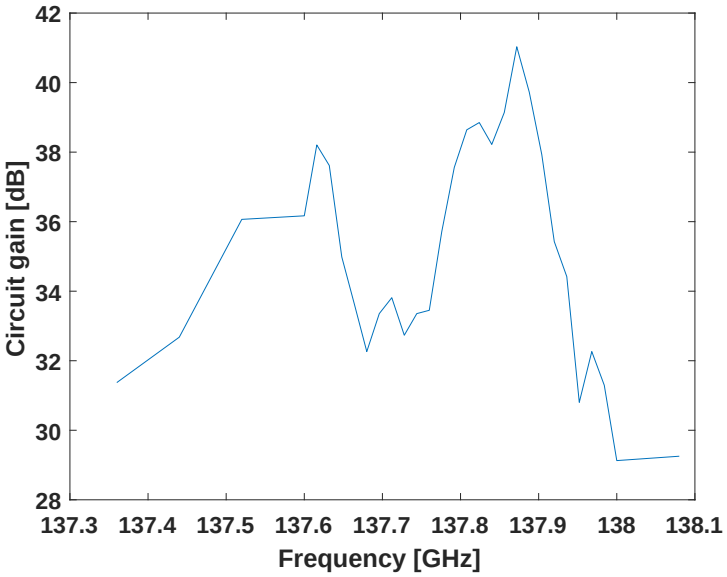

Figure 5-29: Gain bandwidth for an operating condition of 5.085 T, 38 kV, and beam current of 3 A. The gain bandwidth is narrow, but high as it is close to the cutoff frequency.

Chapter 6

Conclusion

In this thesis, I have presented the theory and experimental results of a confocal gyro-TWT operating at 140.0 GHz for use with pulsed DNP/NMR. As intended for operation with pulsed DNP/NMR, this gyro-TWT has demonstrated the highest zero-drive stable gain for a confocal circuit at 35 dB of circuit gain with a bandwidth of 1.2 GHz, centered around the design frequency of 140.0 GHz. The gyro-TWT achieved 550 W of output power, also at a zero-drive stable condition. This achievement opens the possibility of operating pulsed DNP/NMR at higher magnetic field values. It should be noted that the gyro-TWT achieved a small signal circuit gain of about 39 dB at 137.9 GHz; however this bandwidth was limited and centered near cutoff, not within the desired operating frequency of 140.0 GHz. The zero-drive stable operation was possible because it was discovered that the inner walls of the vacuum tube itself can support modes that are well-confined within the central portion of the system, exactly where the electron beam is travelling. A reasonable assumption had been that the cross section of the vacuum tube, which is hundreds of wavelengths (at 140 GHz) in diameter, could be reasonably treated as being an infinite distance away, and thus radiation leaked from the confocal rails would be lost to the system. The inclusion of Macor into the vacuum tube led to zero-drive stable operation. The realization that a system with dimensions that are large compared to the operating wavelength may pose difficulties for open geometries such as the confocal waveguide is an advancement that may be applied in future open geometry waveguides, and is a contribution to

the general field of gyro-TWT research.

More particularly, Chapters 2, 3, and 4 of this thesis discussed the theory and numerical studies associated with a confocal gyro-TWT. Specifically, Chapter 2 focused on the quasi-optical analysis of the confocal waveguide modes. In Chapter 3, we reviewed the gyro-equations that govern the gyro-TWT interaction. Chapter 4 presented the concept of beamlets as a numerical tool for analyzing the interaction between an electron beam with an annular arrangement of guiding centers when overlapping with an asymmetric waveguide mode. Several numerical examples were shown that may be of use in future designs for waveguides that support asymmetric modes.

In Chapter 5, a comprehensive discussion of the gyro-TWT experimental setup was presented. The macroscopic components of the experiment, namely the magnet, electron gun and high voltage modulator, and transmission line system were included. A detailed discussion of the design of the confocal waveguide, including the quasi-optical mode converters, followed. The design goals, operation of the experiment, and results concluded this chapter.

The Appendices show the results of an analysis performed both on the superconducting magnet as well as the VUW-8140 MIT electron gun, which are both important components of the gyro-TWT experiment. The measurements detailed in the Appendices provide important information about the performance of the magnet and electron gun, and how their performance may affect the final amplification result.

6.1 Recommendations for Future Work

6.1.1 Electron gun design

The results presented in this thesis, whilst promising, have a good chance to be improved upon. Most notably, it is desirable to reduce the velocity spread of the electron beam. As seen in Section B.1.1, the VUW8140 was originally designed to operate under a different set of conditions than those that are necessary for amplification at

140 GHz. The nominal velocity spread due to optical effects was predicted to be under 3%. If this figure could be reduced further, by using contemporary particle codes and fabrication techniques, in a design of a new MIG electron gun specific for 140 GHz amplification, then the gain may be increased.

6.1.2 Structural setup of gyro-TWT components

The fact that the magnet features a horizontal bore is an additional consideration that may be taken into account in future efforts. Maintaining a straight, horizontal, mechanical alignment with heavy components over a meter is a structural challenge. Furthermore, ensuring that the beam tunnel and confocal rail axes are collinear is important for guaranteeing that the electron beam maintains a consistent overlap with the confocal waveguide modes over the length of the interaction. In essence, the structural engineering of the internal components (confocal waveguide, mode converters, and corrugated waveguide) should be of principle importance. Additionally, maintaining a parallel set of confocal rails over a length of 20 cm can be addressed with a different fabrication technique. It may be possible to wire EDM a set of confocal rails from one block of copper, for example.

Appendices

Appendix A

Magnetic Field Measurements

A.1 The Superconducting Magnet

The superconducting magnet used in the 140 GHz gyroamplifier experiment was manufactured by Magnex Scientific, LLC. The magnet is capable of a maximum field strength of 6.2 T, although for normal operation at 140 GHz the field is approximately 5 T. The bore of the magnet is 12.7 cm (5 inches) and is kept at room temperature. To maintain the temperature necessary for superconductivity, the main field coils are immersed in a bath of liquid helium. An outer layer of liquid nitrogen helps to insulate the liquid helium, and a vacuum jacket provides additional thermal isolation from the laboratory temperature.

Several practical factors need to be considered during the design of an amplification circuit that relate directly to the superconducting magnet. An important parameter is the flat top length of the field, which determines the maximum length a circuit can be designed for. This magnet features an axial flatness of $\pm 0.5\%$ over a length of 20 cm, so the electron bunching that takes place at the operating field can only occur over the length of the flat top. Once electrons are no longer in the flat top, their dispersion line changes and they effectively fall out of tune with the microwaves. A second parameter of concern is the ratio of the transverse to axial fields. This ratio is a measure of the uniformity of the entire field throughout the bore, and is specified to be $B_t/B_z < 0.15\%$. A large transverse field would be detrimental to the electron

beam quality, which in turn would reduce the amplification. Finally, a measurement of the tilt and offset between the bore's mechanical axis and the axis of the magnetic field is an important check. Although the gyrotron tube is supported on both ends by 2D translation stages, a gross tilt is cause for concern because it could be indicative of a shift in the coil windings of the magnet itself. Likewise, the 2D translation stages cannot correct for any bowing in the magnetic field.

The electron gun itself is located in the bore of an independent gun coil assembly. This assembly is bolted to the face of the Magnex Scientific superconducting magnet. The same concerns as one would have about the superconducting magnet exist for the gun coil. The gun coil acts to trim the field at the cathode, so its uniformity and parallelism should be checked.

A.2 Measurement of the Field

A.2.1 Measurement technique

In order to check the compliance of the magnet's specifications, a 3D Hall probe (Lakeshore model 460 3-channel gaussmeter) was used. The measurements performed follow the magnet test procedure outlined in the Acceptance Test Procedure performed by Cyromagnetics on the 9.6 Tesla Recondensing Gyrotron Superconducting Magnet System. No documentation pertaining to the specific procedure related to the 6.2 T magnet by Magnex Scientific could be found; however, the measurement procedure carried out calculates the relevant parameters.

In order to measure the ratio of transverse to axial field (B_t/B_z), the 3D Hall probe is directly offset from the mechanical axis by a radius R_{probe}, a schematic of which is shown in Fig. A-1.

The probe is rotated cylindrically about the center of the circle prescribed by R_{probe} and magnetic field values on the transverse Hall probes are recorded at set angles. The net transverse field B_t is found by the following calculations:

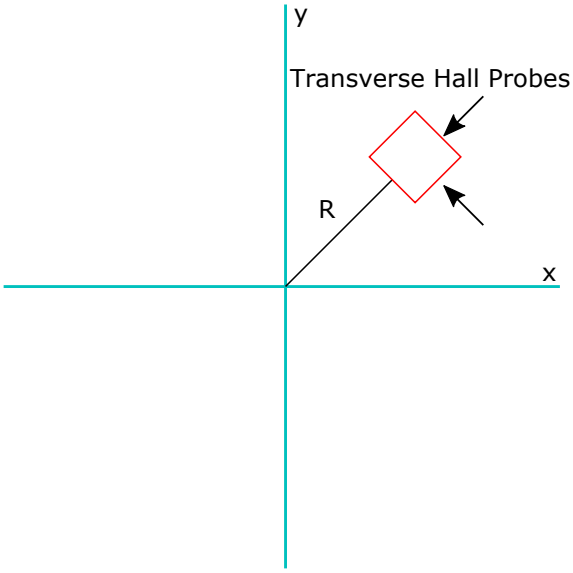

Figure A-1: Schematic of 3D Hall probe. The arrows denote the components of the magnetic field as measured on the sides of the Hall probe.

$$B_x = (B_{90} - B_{270})/2 \tag{A.1}$$

$$B_y = (B_0 - B_{180})/2 \tag{A.2}$$

$$B_t^2 = B_x^2 + B_y^2 \tag{A.3}$$

Likewise, using the same data we can extract the offset between the bore's mechanical axis and that of the magnetic field's. This is computed as:

$$\text{Offset}_\text{x} = \Big[(B_{90} - B_{270})/(B_{90} + B_{270})\Big] * R_\text{probe} \tag{A.4}$$

$$\text{Offset}_\text{y} = \Big[(B_0 - B_{180})/(B_0 + B_{180})\Big] * R_\text{probe} \tag{A.5}$$

Eqns. A.1 - A.5 can be used to determine if there is a gross misalignment between the bore and the magnetic field axis. Additionally, it can help to establish if a linear offset (no bowing of the magnetic field) can be corrected for with the mechanical 2D translation stages that hold the gyrotron tube.

Finally, a direct measurement of the axial field will verify the axial uniformity to be ±0.5% over the flat top of 20 cm.

A.2.2 Setup of Measurement Experiment

The measurement used the Lakeshore 460 3-channel gaussmeter probe, which had to be held off-axis from the center of a guiding support. It was necessary to design a support structure for the probe as well as a guiding carriageway in order for the probe to be moved axially and rotationally. Two values of R_{probe} were used, 0.35 and 0.2 inches. This is shown in Fig. A-2. The two offsets can be used independently to verify that the measurement results are not about a choice of a specific R_{probe}. The assembled probe support system is shown in Fig. A-3.

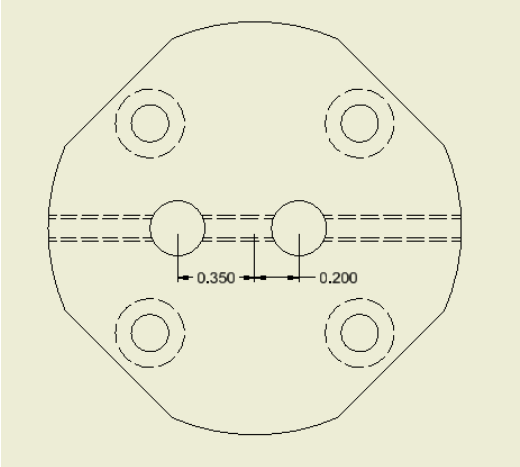

Figure A-2: Inventor CAD drawing of the main probe support, showing the two R_{probe} offsets of 0.35 and 0.2 inches.

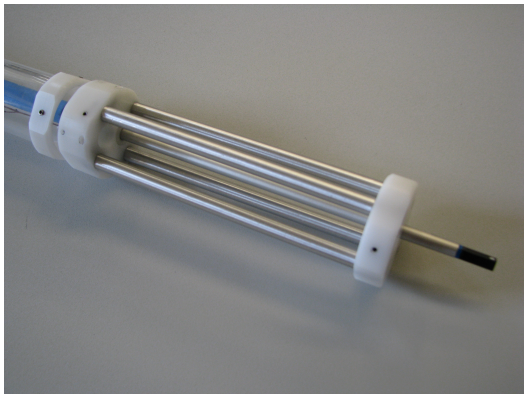

Figure A-3: Photograph of the assembled probe support system.

A.2.3 Measured results

The axial magnetic field was measured in order to check the specified ±0.5% flatness over the 20 cm of interaction length. This measured value is shown in Fig. A-4, in which the nominal peak magnetic field was set at 1 T.

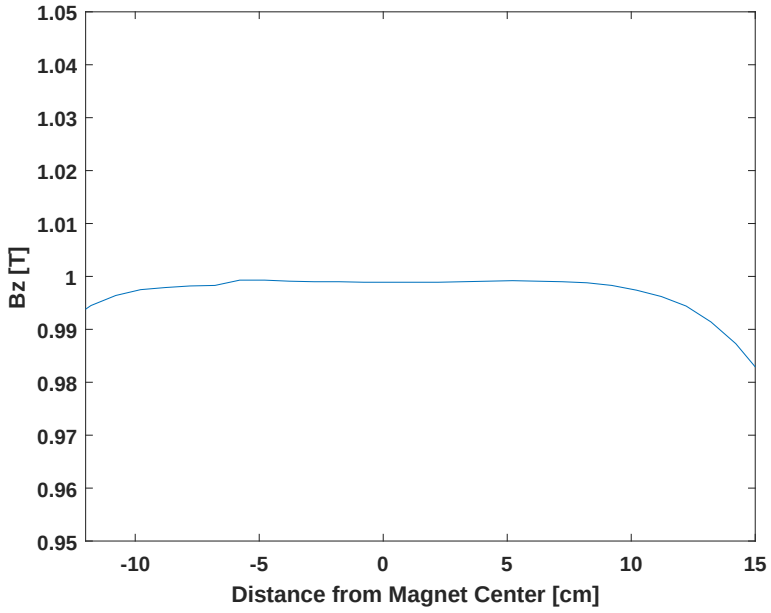

Figure A-4: The axial value of the magnetic field (nominal peak of 1 T) is within the ±0.5% specified flatness over the 20 cm of interaction length.

These values were recorded over the 20 cm flat top of the main field within the magnet's bore and compared to the measured Bz. A plot of the ratio against position relative to the magnet's center is shown in Fig. A-5. The offset is about 0.3% on average, which is twice the specified 0.15%.

The relative ratio of the transverse to the axial field is a result of a mechanical misalignment between the vacuum pipe and the magnetic axis. This is calculated and shown in Fig. A-6. The offset is relatively uniform over the magnetic field's flattop, and can therefore be corrected by an adjustment of the 2D stages. In practice, the 2D stages that shift the vacuum pipe are tuned according to the maximum output power at a given operating point. This corresponds to the best alignment between the vacuum pipe's mechanical axis and that of the magnetic field's axis.

A.3 Conclusions on Magnetic Field

The 6.2 T Magnex Scientific superconducting magnet's magnetic field was measured and analyzed. The flat top was verified over the 20 cm of interaction length where the

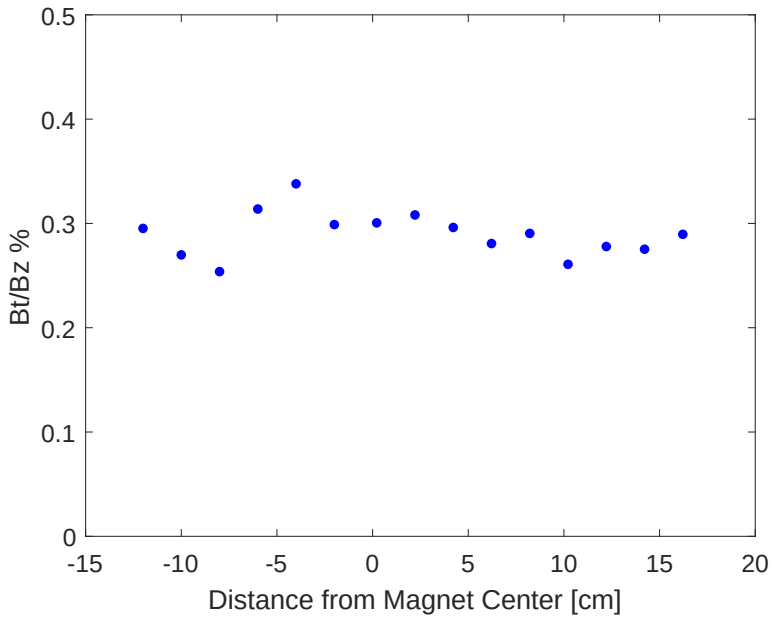

Figure A-5: Ratio of transverse to axial fields in the magnet bore. Positive displacement is toward the gun. The average $Bt/Bz \sim 0.3\%$ is about twice the specified 0.15%.

confocal circuit is located. Although there is a small mechanical offset between the mechanical and magnetic axes, this can be corrected for by repositioning the entire tube via the 2D translation stages. It is common practice, in fact, that after the vacuum tube is open to atmosphere and resealed that the tube is checked for alignment. This comprehensive magnetic field study confirmed that the Magnex Scientific magnet is in good operation and suitable for use on the gyro-TWT experiment.

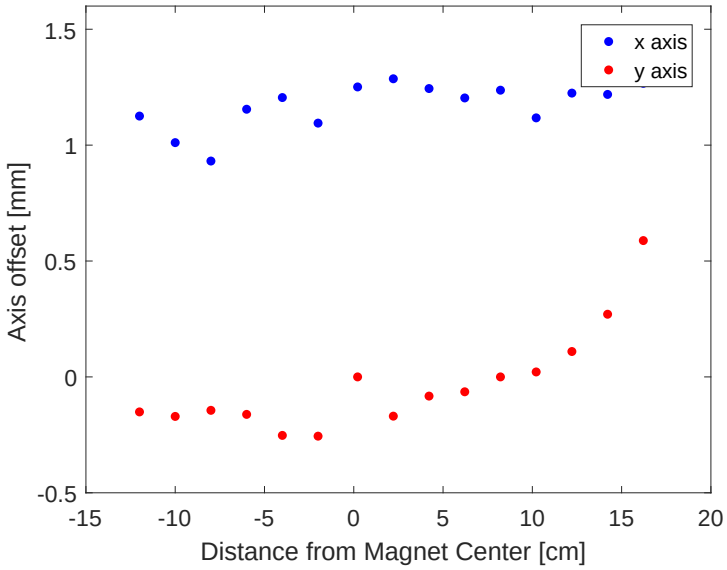

Figure A-6: Relative offset of the magnetic fields due to mechanical misalignment. This can be corrected by adjusting the 2D translation stages that are attached to the magnet body.

Appendix B

VUW-8140 electron gun

B.1 VUW-8140 non-laminar gun

The VUW-8140 MIT electron gun is one of the cornerstones of the gyro-TWT. As discussed, the electron beam quality and parameters are crucial for a successful operation of the gyrotron amplifier. A comprehensive study of the electron gun was performed in order to gain insight into its performance. Two separate tests were conducted: a beam interception test (witness plate measurement) and an emission versus voltage study.

B.1.1 Setup of the VUW-8140

An effort was made to characterize the VUW-8140 MIG electron gun that is in use on the 140 GHz gyroamplifier experiment. The VUW-8140 (CPI designation K-8140) is a non-laminar gun designed in a triode configuration for use in pulsed operation. Its 15 degree cathode angle results in non-laminar electron beam behavior. The original operating parameters are listed in Table B.1, along with computed beam performance.

A measurement was made of the voltage and current drawn by the cathode heater. This was compared to original CPI values, and is shown in Fig. B-1.

The computed resistance of the heater element is seen to have changed over the lifetime of the VUW-8140 by a factor of nearly two. This may indicate that the heater

Beam Voltage	65 kV
Beam Current	5.0 A
Maximum Beam Current	7.5 A
Mod-Anode Ratio	0.7
Heater Voltage	12.2 VAC
Heater Current	3.5 AC
Magnetic Field	5.64 T
Pitch Factor (α)	1.49
Perpendicular Velocity Spread ($\delta v_\perp$)	2.68%

Table B.1: VUW-8140 design parameters.

element has a varying ohmic resistance that is non-uniform around the cathode, which could result in non-uniform emission. Although the filament resistance has changed over the lifetime of the VUW-8140's use, the power drawn by the heater is known. A calibration for cathode temperature was computed based on original factory data that relates heater power to cathode temperature, and is shown in Fig. B-2.

In addition to the heater resistance, a test was performed to verify that the maximum output current at 65 kV reaches and surpasses the original 5.0 A design. A measurement of the absolute current emitted as a function of calculated cathode temperature is shown in Fig. B-3, and confirms that the VUW-8140 is capable of high-current emission.

While the VUW-8140 cathode was shown to have retained its high-current emission property, a further characterization was necessary to better understand the beam quality. The beam quality, both its uniformity and estimated spread in electron velocities, is an important factor in achieving high gain.

B.1.2 Beam interception test

The inherent asymmetry of the confocal waveguide's modes (HE_{0n}) requires that the electron beam be uniform in order to guarantee an interaction with the operating mode. If the gun is emitting non-uniformly, the possibility for a disproportionately large fraction of the total current to be localized at a minimum in the HE_{06} distribution exists. In this situation, a weak coupling between the electron beam and HE_{06}

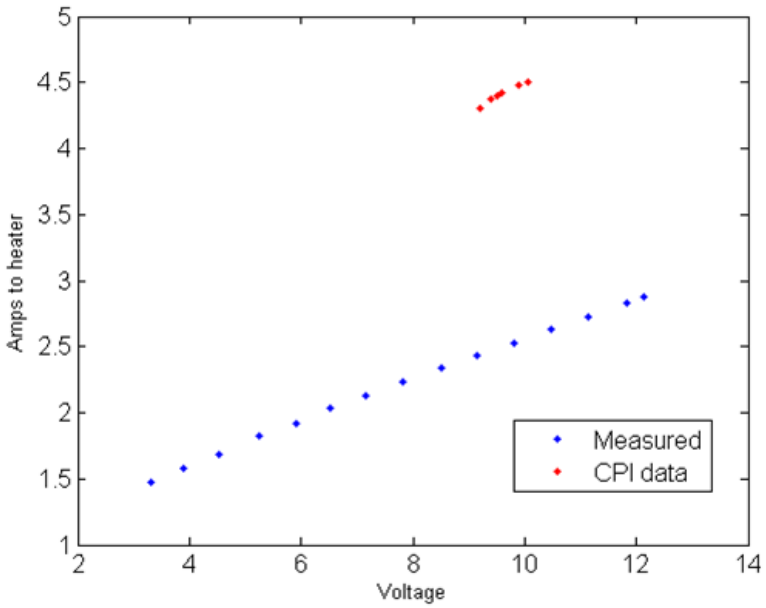

Figure B-1: Current drawn by the resistive heater element in the VUW-8140. Values compared to CPI data.

mode will result in low gain. A beam interception test can detect non-uniform emission. This test consists of placing a copper witness plate in the path of the electron beam. Damage incurred on the copper's surface when the beam is intercepted will show the relative distribution of current; a damage profile that is a uniform ring is the ideal result and indicates uniform emission. A copper plate was machined to attach to the end of the confocal circuit, which in turn is aligned to the mechanical axis of the confocal circuit. This configuration would provide the opportunity to detect if the mechanical and magnetic axes are collinear, an important criterion for optimizing the gain. The relative position of the witness plate to the magnetic center and the gun cathode is shown in Fig. B-4.

The electron gun was pulsed at 45kV, 5T, and 1.5 A peak current for over 2k shots. Operating under these conditions, with a repetition rate of 0.3 Hz, maintained a low pressure in the vacuum chamber (10^{-7} torr). Several individual shots were conducted at a peak current of 2 A, which resulted in a large pressure rise and subsequent interlock control that turned off the high voltage modulator. The damage profile from this test is shown in Fig. B-5.

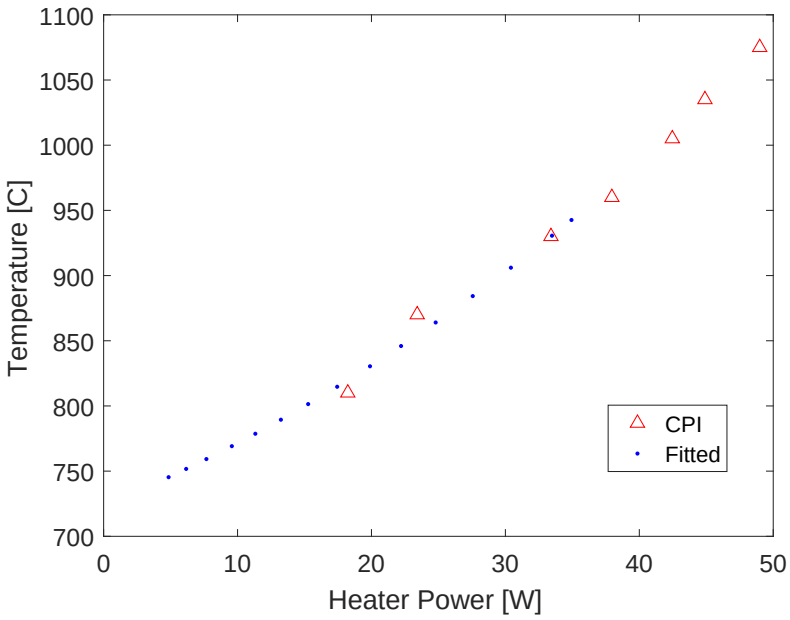

Figure B-2: Predicted cathode temperature as a function of power drawn by the heater filament. This predicted temperature is the result ofa fit to the original factory data, which is presented as a comparison.

Upon extraction of the copper witness plate, it was noted that the plate was offset from the mechanical axis by 0.9mm in the vertical direction. This is shown in Fig. B-5. Thus, the net offset of the electron beam from the confocal circuit's axis is $\Delta r \sim 1$mm. This can be accounted for by a tilt at the tapered clamp and nose connection of $\Delta\theta \sim 0.25$ deg. The mechanical alignment internal to the vacuum chamber is important, and the witness measurement suggests that the mechanical design can be improved to insure alignment.

The ring of damage furthermore suggests that the current emission of the VUW-8140 may not be uniform. The increased damage along one arc of the ring indicates a hot spot in the cathode surface's emission. For a qualitative comparison, a witness plate measurement from 2001 is shown in Fig. B-6.

The qualitative comparison of the two witness plate measurements motivated a second beam interception test to be conducted on the present-day VUW-8140. A redesign of the copper plate's internal support simplified the mechanical structure and includes an axial compression force to insure that the tapered clamp and nose

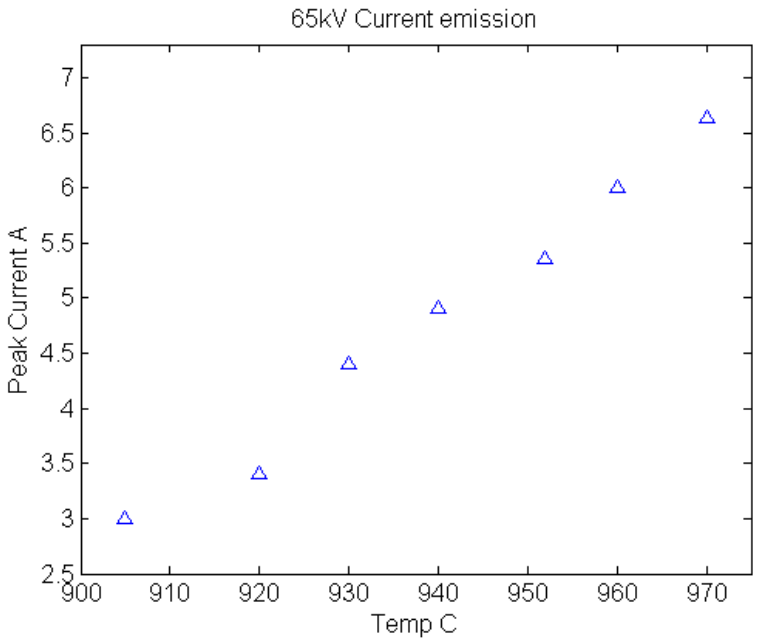

Figure B-3: Total current emission as a function of increasing cathode temperature.

assembly is reliably aligned. This new design for the second witness plate measurement is shown in Fig. B-7. The result of the second beam test is shown in Fig. B-8. Whilst the witness plate measurements are useful tests, the damage inflicted on the copper may be nonlinear with current. Thus, although these measurements do reveal asymmetry, the absolute extent of the current distribution may be difficult to determine.

B.2 Emission versus applied voltage

Studies of emitted current versus an applied voltage are useful for quantifying the material properties of the emitter surface. The surface work function of the emitter should be peaked about a known value, ϕ_o. Any spread in the work function about ϕ_o will mean that electrons born on the surface experience locally-different potentials. The consequence is that there is a temperature to the electron beam - a velocity spread will exist. Qualitatively, a larger spread in the work function will result in a larger velocity spread. Current versus voltage was measured for several heater settings using the VUW-8140 electron gun. The following is a discussion of both emission theory

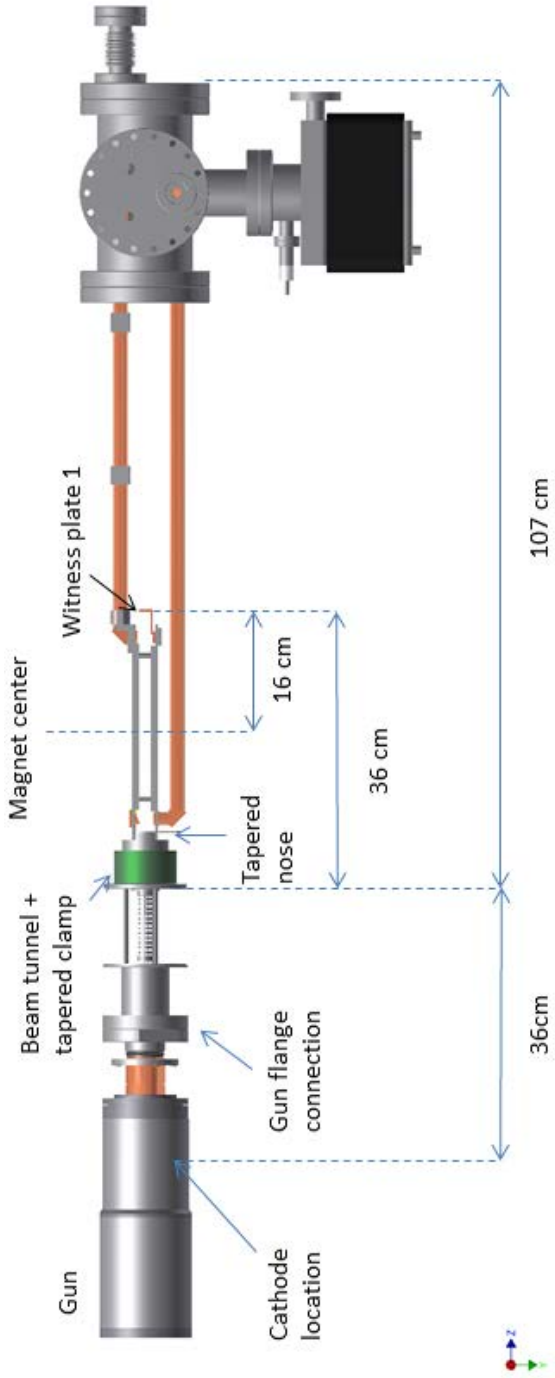

Figure B-4: Schematic showing the location of the witness plate. The plate is 72cm from the cathode and 16cm from the magnetic center.

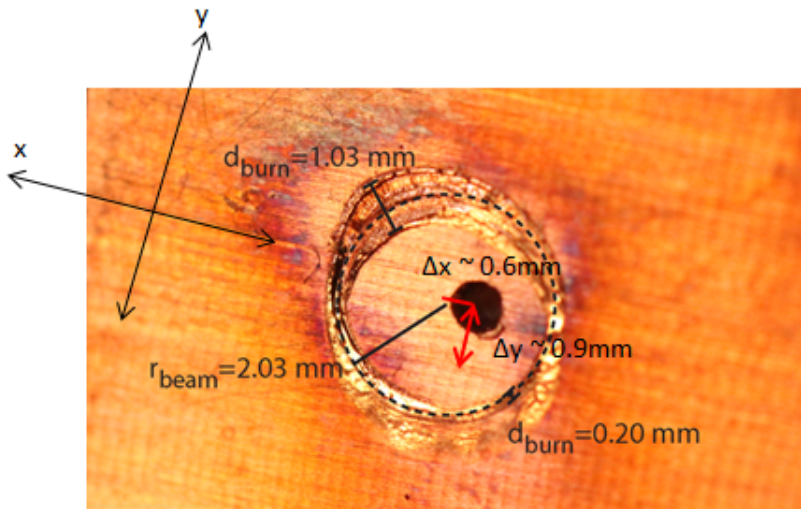

Figure B-5: Damage profile on copper witness plate. Asymmetric damage is seen, as well as an offset from the mechanical axis.

and a presentation of the I-V data from the emission study on the VUW-8140.

B.2.1 Emission theory

Cathode emission as a function of applied voltage (I-V curves) may be used to extract characteristic parameters that describe the emitter material. Information about the emitter material is contained in the shape of the I-V curve. At lower voltages, emission from the cathode is dominated by space-charge effects, and has the functional form

$$J_{sc} = \kappa V^{(3/2)} \tag{B.1}$$

where κ is the perveance and V is the applied voltage. The perveance, with units of $[amps/cm^2 volts^{(3/2)}]$, relates the current to voltage for the space charge effect. At higher voltages, emission becomes dominated by temperature limiting behavior:

$$J_{tl} = A_o T^2 \exp\Big[-\frac{e}{kT}(\phi_o - \sqrt{\frac{eE}{4\pi\epsilon_o}})\Big]. \tag{B.2}$$

In Eq. B.2, A_o is a constant that relates current to temperature with units of A/[cm^2]/[deg^2],ϕ_o is the work function of the emitter material, and E is the local electric field. In the case of an emitter material with a work function of a single

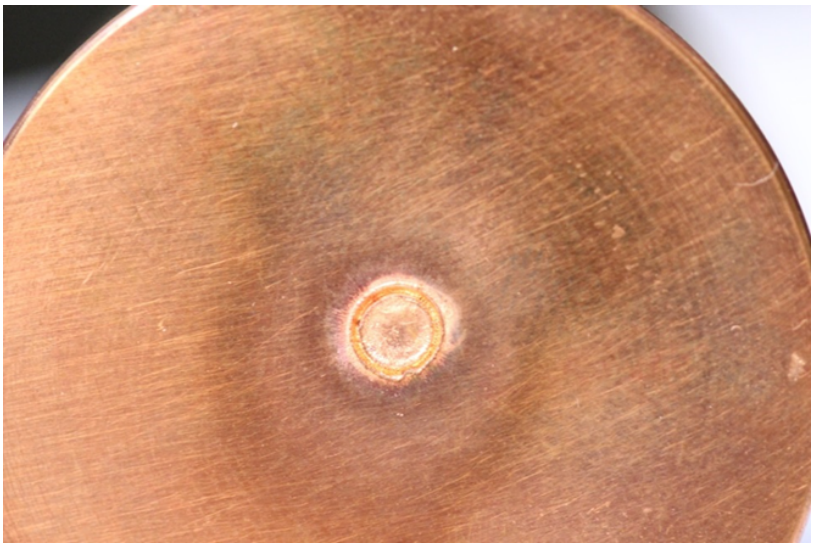

Figure B-6: Damage profile of a beam interception test from 2001. The radius of the ring is 2mm.

value, the emission behavior of the cathode would be entirely dominated by Eq. B.1 until some transitional voltage V_T, at which point the emission is governed by Eq. B.2. A real material actually has some nominal spread in the work function, σ. Assuming a Gaussian distribution in work function,

$$D(\phi) = \sqrt{\frac{1}{2\pi}}\frac{1}{\sigma}\exp\left[\frac{-(\phi-\phi_o)^2}{2\sigma^2}\right] \tag{B.3}$$

will introduce a voltage range in which the emission is a mixture of both space-charge and temperature limiting behaviors. The result of assuming a Gaussian distribution is an emission theory modelled as

$$\begin{aligned} J_V =& \frac{\kappa V^{(3/2)}}{2}\left[1+\operatorname{erf}\left(\frac{\phi_V-\phi_o}{\sqrt{2}\sigma}\right)\right] \\ &+ \frac{A_o T^2}{2}\left[1-\operatorname{erf}\left(\frac{\phi_V-\phi_o+\frac{e\sigma^2}{kT}}{\sigma\sqrt{2}}\right)\right] \\ &\times \exp\left[\frac{-e}{kT}\left(\phi_o-\sqrt{\frac{eE}{4\pi\epsilon_o}}-\frac{e\sigma^2}{2kT}\right)\right] \end{aligned} \tag{B.4}$$

Here, ϕ_V is a transitional work function, which is dependent on the voltage, temperature, and other physical constants:

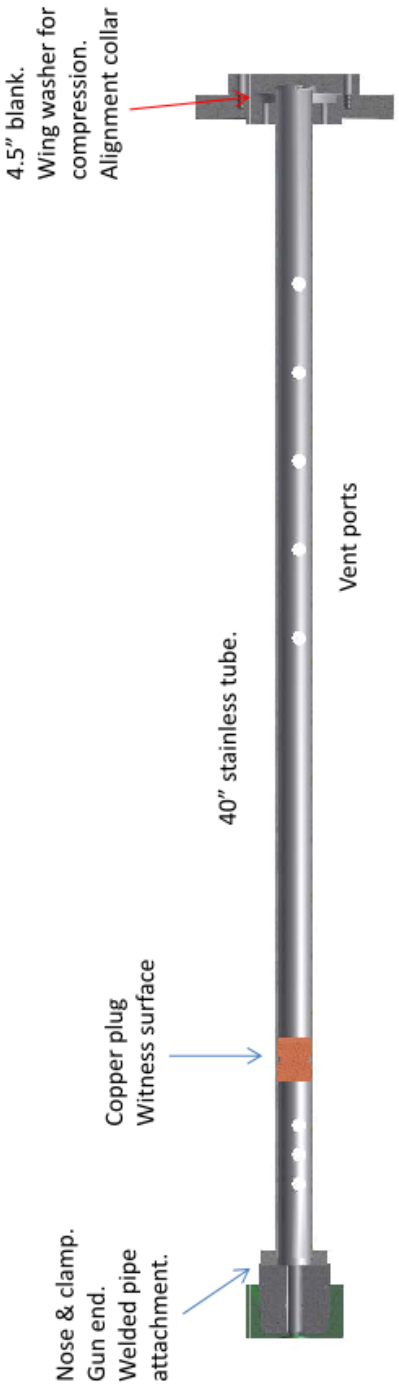

Figure B-7: The second witness plate test is supported by a simplified structure.

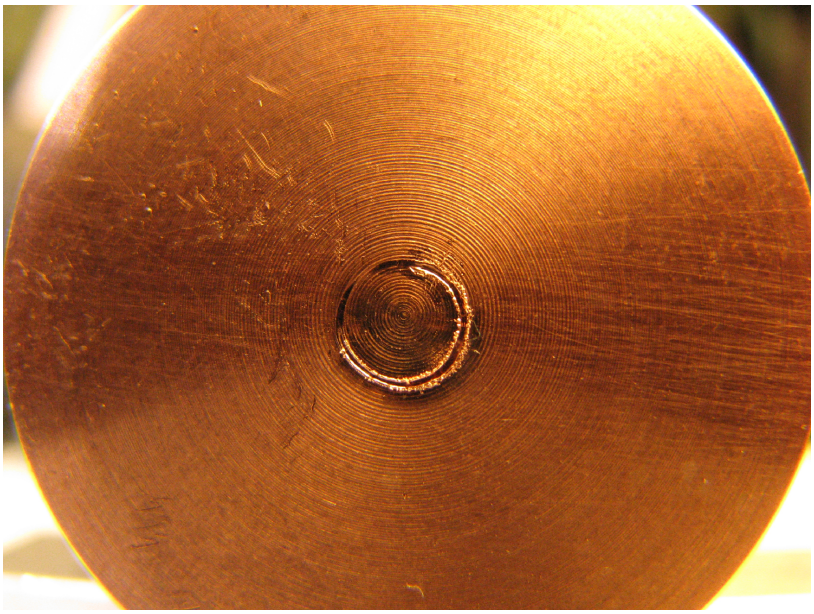

Figure B-8: Damage profile as seen on the second copper witness plate following the beam interception test. The same asymmetric damage is seen as in the first measurement.

$$\phi_V = \sqrt{\frac{eE}{4\pi\epsilon_o}} - \frac{kT}{e}\ln\left(\frac{\kappa V^{(3/2)}}{A_o T^2}\right). \tag{B.5}$$

Eq. B.4 can be used to fit to emission versus voltage data. The nominal fitting parameters become ϕ_o and σ, both of which describe the physical properties of the emitter material. Comparing the fitted value of the work function to the known value can provide some insight into the quality of the emitter material itself; a large deviation from the chemistry literature value may indicate a degradation of the surface material. Additionally, a large spread in the work function, σ, would further indicate that the cathode emitter has degraded over its lifetime. A large spread in the work function implies that electrons leaving the surface have a broader spread in temperature; thus, a large σ is a strong indication that velocity spread in the beam may be greater than the value determined purely from the optical model used by numerical codes. A theoretical I-V curve is shown in Fig. B-9. Here, the work function is fixed at $\phi_o = 1.90$ eV and the temperature at 965 C. This example shows that with a larger work function spread the rollover to temperature limited behavior takes place over a wider range of voltages. Likewise, the knee in the emission profile is not as sharp as

it is for lower values of work function spread.

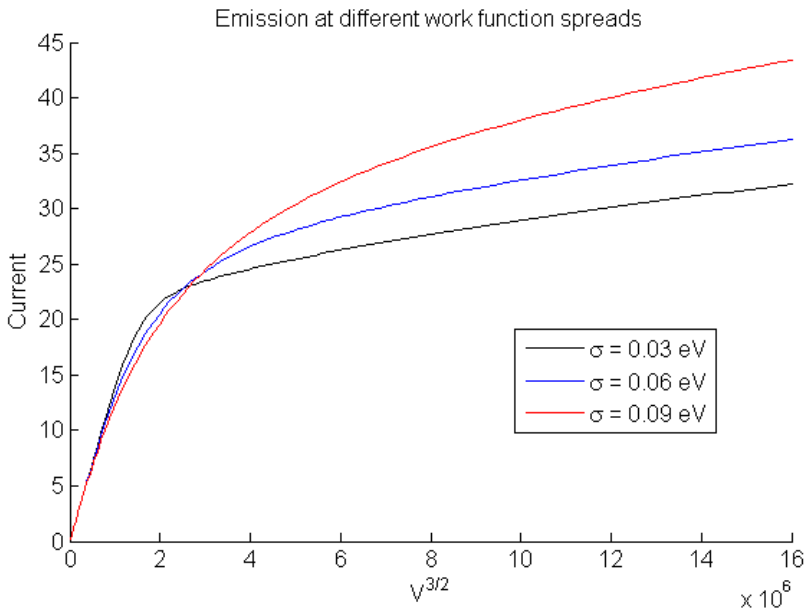

Figure B-9: Theoretical emission for various values of work function spread σ. The shape of the rollover in the current versus voltage data determines the numerical value of σ in a fit.

An important consideration is the constant A_o, which relates the emission to temperature of the material. Although theoretically computed to be $A_o = 120$ [amps/cm^2/deg^2], in general A_o is variable and material-dependent. Consequently, A_o is relegated to be a fitting parameter in Eq. B.4. During a numerical analysis using Eq. B.4, it was found that there is a degeneracy in the fitting parameter pair of ϕ_o and A_o. For a given I-V dataset, an infinite number of specific (ϕ_o, A_o) pairs generated the same emission curve. This would be the case if the argument of the error functions in Eq. B.4 were numerically independent of (ϕ_o, A_o). A second criteria is that the numerical value of $A_o \exp\big(-\frac{e\phi_o}{kT}\big)$ remained independent of the (ϕ_o, A_o) choice. Mathematically, these two criteria can be expressed as

$$\phi_{V1} - \phi_1 = \phi_{V2} - \phi_2 \tag{B.6}$$

and

$$A_1 \exp\big(-\frac{e\phi_1}{kT}\big) = A_2 \exp\big(-\frac{e\phi_2}{kT}\big)$$

for two pairs (ϕ_1, A_1) and (ϕ_2, A_2). Provided that the functional forms in Eq. B.6 that relate ϕ_o to A_o are identical between the two criteria, then there is a degeneracy in solutions for (ϕ_o, A_o). Referring to Eq. B.5, we rearrange to find the dependence of ϕ_V on A_o:

$$\phi_V \rightarrow \frac{kT}{e} \ln\left(A_o\right) \tag{B.7}$$

Using this relationship and applying it to the criteria in Eq. B.6, we find that

$$\phi_{V1} - \phi_1 = \phi_{V2} - \phi_2 \Rightarrow \frac{kT}{e} \ln\left(A_1\right) - \phi_1 = \frac{kT}{e} \ln\left(A_2\right) - \phi_2 \tag{B.8}$$

and

$$A_1 \exp\big(-\frac{e\phi_1}{kT}\big) = A_2 \exp\big(-\frac{e\phi_2}{kT}\big)$$

It is seen that, when taking the natural log of the second expression, we return the functional form of the former. Thus, the numerical values of ϕ_o and A_o in a fit of I-V data to Eq. B.4 are not unique for a given dataset; a change in the value of ϕ_o is numerically compensated by a change in the value of A_o by an analytical expression. The value of the theoretical emission is unchanged. Additionally, the value of the spread σ is determined independently of the degenerate (ϕ_o, A_o) pairs, and thus a unique value is found for a given dataset. Using emission data taken with the 110 GHz experiment's SpectraMat osmium-coated cathode, the solved numerical and analytical relationship between ϕ_o and A_o is seen in Fig. B-10. For each dataset (specified by temperature), any pair of ϕ_o and A_o obeying the analytical curves is a valid numerical solution.

Although the degeneracy in (ϕ_o, A_o) pairs exists, it is still possible to perform a numerical fit to emission data. It is clear that although infinite (ϕ_o, A_o) pairs exist for an emission data set, in reality a small range of (ϕ_o, A_o) values are representative of the physical system. In order to obtain a (ϕ_o, A_o) pair that is physically-reasonable, Eq. B.2 is fit to the high voltage emission data. In this high voltage limit, the local

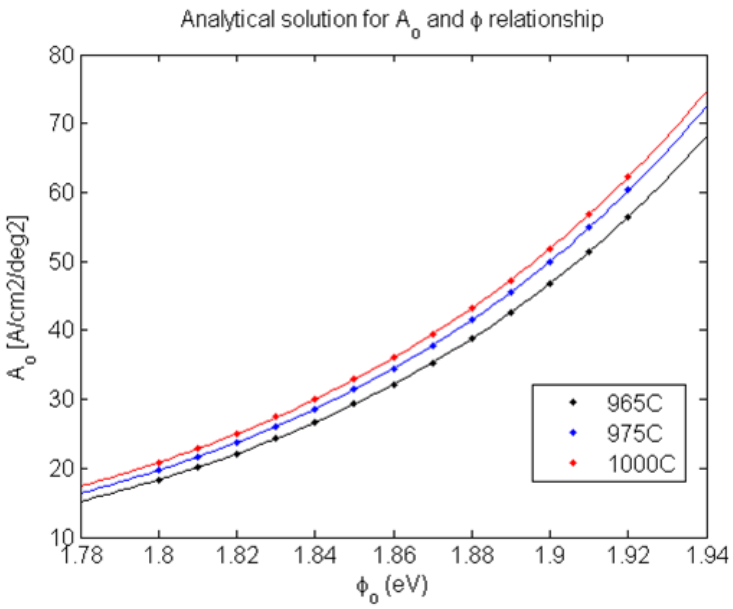

Figure B-10: Numerical fits (dots) and analytical relationship (lines) show that ϕ_o and A_o pairs are a degenerate solution to the emission theory.

electric field, E, is well-approximated by $E \sim V/d$, where d is the anode-cathode gap. For the VUW-8140, $d = 8.2mm$. This term causes a slight slope in the high voltage emission behavior and is known as the Schottky effect. Rewriting Eq. B.2 in the limit $V \to 0$,

$$J_{tl} = A_o T^2 \exp\big(-\frac{e\phi_o}{kT}\big). \tag{B.9}$$

Taking the natural logarithm of Eq. B.9,

$$\ln\big(\frac{J_{tl}}{A_o T^2}\big) = -\frac{e\phi_o}{kT}. \tag{B.10}$$

Assuming that A_o is a constant with varying temperatures, the slope of $\ln(J_{tl}/T)$ versus $-e/kT$ is the work function (in the temperature limit model). This extrapolates the work function value ϕ_o, which in turn can be used in Eq. B.2 to fit the high voltage data with A_o as the fitting parameter. This technique provides an initial value for a (ϕ_o, A_o) pair that can be used in fitting the emission model Eq. B.4 for the full emission data set.

B.2.2 VUW-8140 emission versus voltage study

A study of cathode emission versus voltage was performed on the VUW-8140 at voltages up to >30 kV. Using the calibration data for cathode temperature versus power, emission was studied over a range of $\sim 880 - 950$ degrees centigrade, the higher temperature being the upper limit during typical operation. At each cathode temperature setting, the emission was allowed to stabilize between high voltage pulses before the voltage and current traces were saved. By comparing values of voltage and current during the voltage pulse rise, emission data is collected at every temperature value. The data sets are shown in Fig. B-11.

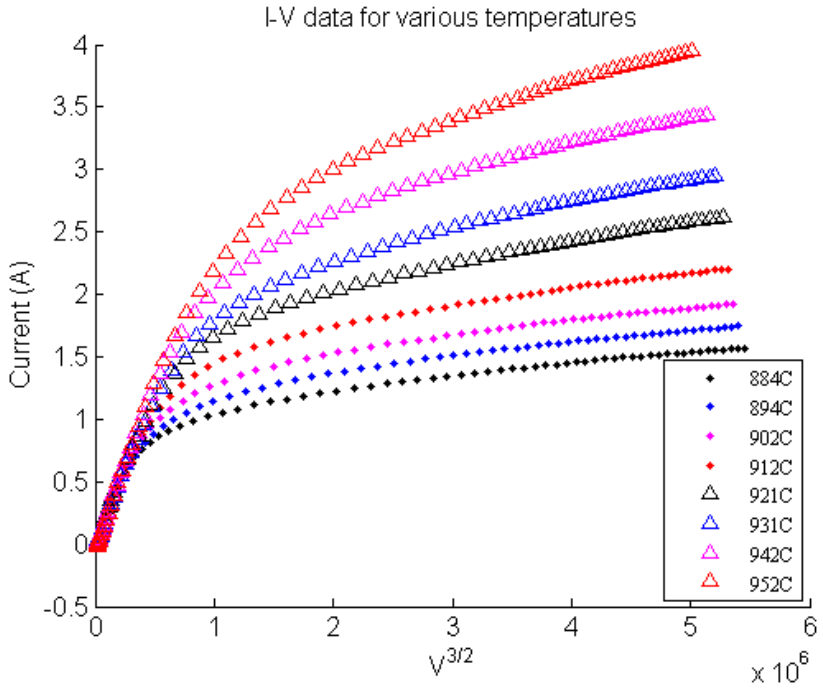

Figure B-11: The cathode emission of the VUW-8140 electron gun as a function of applied voltage. The anode-cathode gap is 8.2 mm and the emitter surface area is 2.5 cm^2.

The perveance is fit for the linear behavior at low voltages. The perveance-area constant, $K = \kappa \times$ area, was found to be $K = 2.7 \times 10^{-6}$ [$A/V^{3/2}$], with good agreement across the temperatures studied. The fitted values for perveance K, as well as the linear slope with the relation $I = KV^{3/2}$, are shown in Figs. B-12 and B-13.

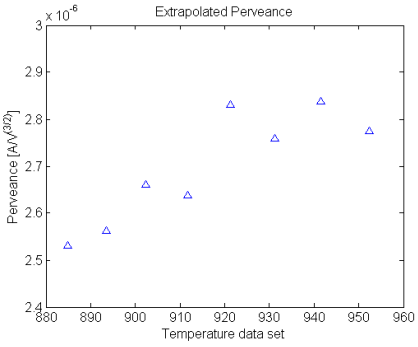

Figure B-12: Computed perveance K from different temperature data sets.

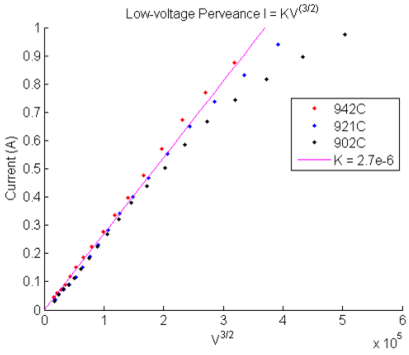

Figure B-13: Plot of linearized relation $I = KV^{3/2}$ using the average value of $K = 2.7 \times 10^{-6}$ [A/V$^{3/2}$].

It is seen that with a perveance $K = 2.7 \times 10^{-6}$ [A/V$^{3/2}$] that the space charge behavior in the low-voltage regime, Eq. B.1, models the emission well. In order to fit for work function and work function spread, the degeneracy of (ϕ_o, A_o) pairs needs to be addressed as described at the end of Section B.2.1. The Schottky effect is extrapolated to zero voltage. Using the slope of $\ln(J_{tl}/T)$ versus $-e/kT$, an approximate work function may be found. This calculation is shown in Fig. B-14. An illustration of extrapolating the Schottky effect to zero voltage is shown in Fig. B-15.

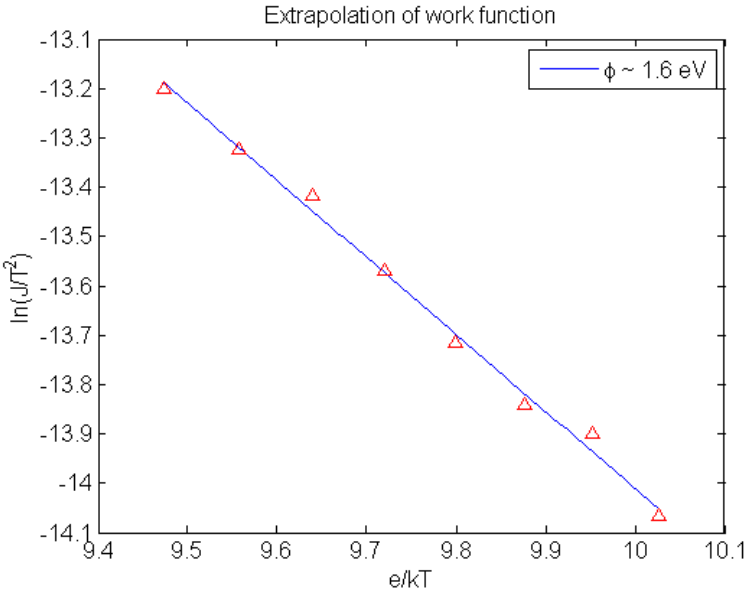

Figure B-14: The slope of $\ln(J_{tl}/T)$ versus $-e/kT$, showing a good agreement with a fit of $\phi_o \sim 1.6$ eV.

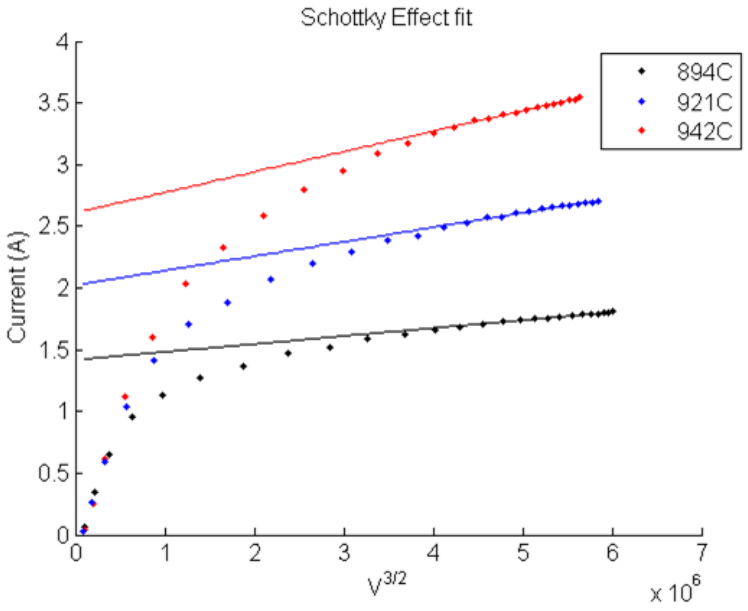

Figure B-15: Schottky effect extrapolated to 0 V.

The work function was found to be $\phi_o \sim 1.6$ eV, a value lower than a typical physical material of a BaO-doped cathode. Using 1.6 eV as a nominal work function value, the high voltage data was fit to Eq. B.2, the temperature limited behavior, in order to extract values for A_o. As may be physically expected, the value of A_o does not vary significantly as a function of temperature, as shown in Fig. B-16, and it's nominal mean of 3.7 [amps/cm^2/deg^2] may be used to fit the full emission theory. Although the theoretical value of A_o is approximately 120 [amps/cm^2/deg^2], in practice the values for this constant are typically lower. Additionally, the non-uniformity seen in the witness plate beam interception test may introduce errors to this method of calculating A_o, since this process assumes a uniform beam. Local values for all three parameters - A_o, ϕ_o, and σ - may vary around the emitter surface.

Eq. B.4 is used to fit the full cathode emission data. The results of the numerical fit with parameters for the work function, ϕ_o, and the spread in the work function, σ, is given in Table B.2. The numerical fit is plotted for various temperatures in Fig. B-17.

Two observations may be mentioned regarding the complete fit to the full emission theory. First, using Eq. B.4 in conjunction to the complete data set does not signifi-

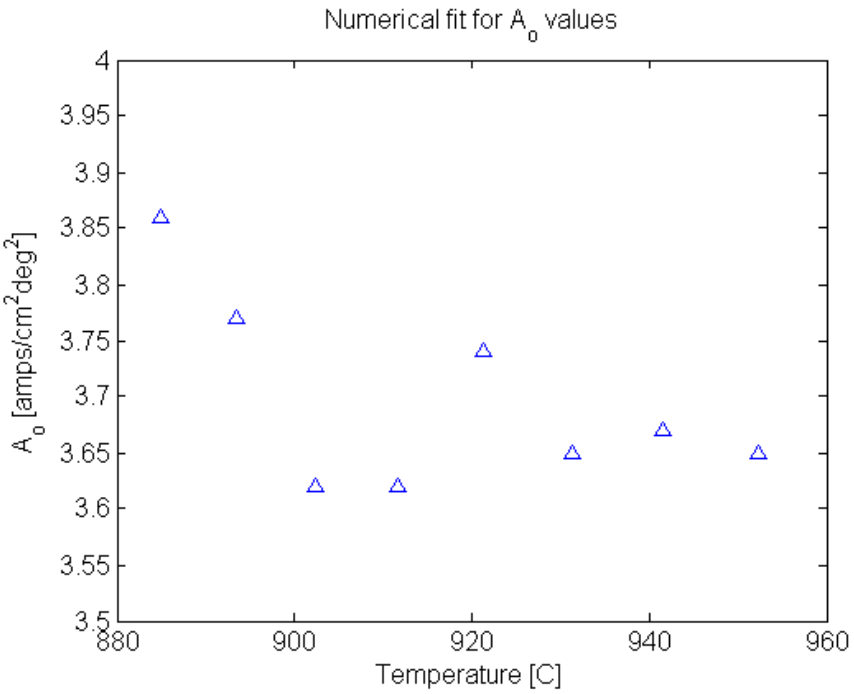

Figure B-16: The value of A_o extracted when fitting high voltage data with an assumed work function of 1.6 eV. The value of A_o varies little with temperature.

cantly alter the values for A_o and ϕ_o. It was demonstrated mathematically that there is a degeneracy in the pair of these parameters. Consequently, the value for the work function as determined by the Richardson plot approach is not necessarily expected to change significantly once the full emission theory and data set are used. Second, it is important to note that the value for the spread in the work function, σ, is fit independently of both A_o and ϕ_o; thus, its numerical value is determined uniquely by the full data set. Values of ~ 0.07 eV are larger than desired, qualitatively; however, this experimental and numerical approach assumed uniform emission. As discussed, the non-uniformity seen in the electron beam interception test motivates the possibility that σ varies greatly around the emission surface, a measurement not determined by this method.

Temperature [C]	ϕ_o [eV]	σ [eV]
884	1.66	0.072
893	1.67	0.072
902	1.67	0.072
911	1.67	0.073
921	1.67	0.078
931	1.68	0.077
942	1.67	0.076
952	1.67	0.074

Table B.2: ϕ_o and σ values for various temperature data sets.

B.3 VUW-8140 conclusion

Because electron beam quality is an important factor in a successful amplifier experiment, the studies performed on the VUW-8140 provide information to be considered in a future gyro-amplifier design. Namely, the azimuthal symmetry of the electron beam needs to be accounted for, and this may be approached by selecting an interaction cavity that supports azimuthally-symmetric modes. Such a selection will insure that electron beam and microwave mode overlap regardless of any beam asymmetry. The second conclusion reached by analyzing emission data is that the emitter material quality itself needs to be understood. Whether the emitter surface is qualitatively good only on certain sections or whether the aggregate itself is of reliable quality may affect the electron beam directly.

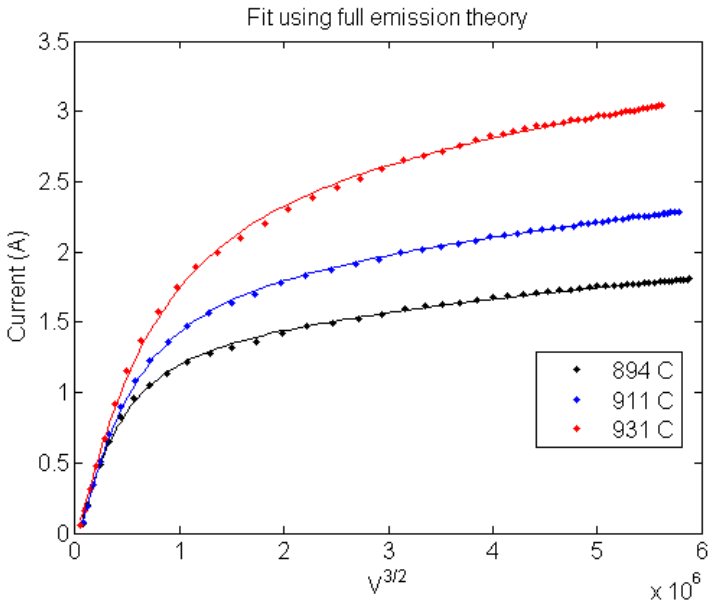

Figure B-17: A fit to the full data set using the complete emission theory of Eq. B.4 shows good agreement.

Bibliography

[1] G. S. Nusinovich. *Introduction to the Physics of Gyrotrons.* The Johns Hopkins University Press, 2004.

[2] M. V. Kartikeyan, E. Borie, M. K. A. Thumm. *Gyrotrons.* Springer-Verlag, 2004.

[3] A. S. Gilmour, Jr. *Klystrons, Traveling Wave Tubes, Magnetrons, Crossed-Field Amplifiers, and Gyrotrons.* Artech Library, 2011.

[4] S. E. Tsimring. *Electron Beams and Microwave Vacuum Electronics.* Wiley, 2006.

[5] C. Edgecombe. *Gyrotron Oscillators.* CRC Press, 1993.

[6] W. L. Menninger, D. C. Eze, R. S. Hollister, and R. H. Martin. High-efficiency, 200-W Ku-band traveling-wave tubes for satellite communications downlinks. In *2013 IEEE 14th International Vacuum Electronics Conference (IVEC)*, pages 1–2, May 2013.

[7] H. Fukui T. Machida, T. Kanamoto and K. Tsutaki. Development of Ka-band 250 W peak power helix TWT. In *Third IEEE International Vacuum Electronics Conference (IEEE Cat. No.02EX524)*, pages 355–356, April 2002.

[8] M. A. Kempkes, T. J. Hawkey, M. P. J. Gaudreau, and R. A. Phillips. W-band transmitter upgrade for the Haystack ultrawideband satellite imaging radar (HUSIR). In *2006 IEEE International Vacuum Electronics Conference held Jointly with 2006 IEEE International Vacuum Electron Sources*, pages 551–552, 2006.

[9] D. M. Sheen, D. L. McMakin, and T. E. Hall. Three-dimensional millimeter-wave imaging for concealed weapon detection. *IEEE Transactions on Microwave Theory and Techniques*, 49(9):1581–1592, Sep 2001.

[10] R. Appleby and H. B. Wallace. Standoff detection of weapons and contraband in the 100 ghz to 1 thz region. *IEEE Transactions on Antennas and Propagation*, 55(11):2944–2956, Nov 2007.

[11] M. K. Choi, K. Taylor, A. Bettermann, and D. W. van der Weide. Broadband 10 to 300 GHz stimulus-response sensing for chemical and biological entities. *Physics in Medicine and Biology*, 47(21):3777, 2002.

[12] K. L. Felch, B. G. Danly, H. R. Jory, et al. Characteristics and applications of fast-wave gyrodevices. *Proceedings of the IEEE*, 87(5):752–781, May 1999.

[13] F. Bloch, W. W. Hansen, and M. Packard. Nuclear induction. *Phys. Rev.*, 69:127, Feb 1946.

[14] E. M. Purcell, H. C. Torrey, and R. V. Pound. Resonance absorption by nuclear magnetic moments in a solid. *Phys. Rev.*, 69:37–38, Jan 1946.

[15] A. W. Overhauser. Polarization of nuclei in metals. *Phys. Rev.*, 92:411–415, Oct 1953.

[16] A. Abragam and M. Goldman. Principles of dynamic nuclear polarisation. *Reports on Progress in Physics*, 41(3):395, 1978.

[17] T. R. Carver and C. P. Slichter. Polarization of nuclear spins in metals. *Phys. Rev.*, 92:212–213, Oct 1953.

[18] T. Maly, G. T. Debelouchina, V. S. Bajaj, K. Hu, C. Joo, M. L. Mak-Jurkauskas, J. R. Sirigiri, P. C. A. van der Wel, J. Herzfeld, R. J. Temkin, R. G. Griffin. Dynamic nuclear polarization at high magnetic fields. *The Journal of Chemical Physics*, 128(5):052211, 2008.

[19] D. Rovnyak, J. C. Hoch, A. S. Stern, and G. Wagner. Resolution and sensitivity of high field nuclear magnetic resonance spectroscopy. *Journal of Biomolecular NMR*, 30(1):1–10, 2004.

[20] J. H. Ardenkjær-Larsen, B. Fridlund, A. Gram, G. Hansson, L. Hansson, M. H. Lerche, R. Servin, M. Thaning, and K. Golman. Increase in signal-to-noise ratio of $>$ 10,000 times in liquid-state NMR. 100(18):10158–10163, 2003.

[21] L. R. Becerra, G. J. Gerfen, R. J. Temkin, D. J. Singel, and R. G. Griffin. Dynamic nuclear polarization with a cyclotron resonance maser at 5 T. *Phys. Rev. Lett.*, 71:3561–3564, Nov 1993.

[22] V. S. Bajaj, M. K. Hornstein, K. E. Kreischer, J. R. Sirigiri, P. P. Woskov, M. L. Mak-Jurkauskas, J. Herzfeld, R. J. Temkin, and R. G. Griffin. 250 GHz CW gyrotron oscillator for dynamic nuclear polarization in biological solid state NMR. *Journal of Magnetic Resonance*, 189(2):251–279, 2007.

[23] S. Jawla, M. Reese, C. George, C. Yang, M. Shapiro, R. G. Griffin, and R. J. Temkin. 330 GHz / 500 MHz dynamic nuclear polarization-NMR spectrometer. In *2016 IEEE International Vacuum Electronics Conference (IVEC)*, pages 1–2, April 2016.

[24] A. B. Barnes, E. Markhasin, E. Daviso, et al. Dynamic nuclear polarization at 700MHz/460GHz. *Journal of Magnetic Resonance*, 224:1 – 7, 2012.

[25] M. K. Hornstein, V. S. Bajaj, R. G. Griffin, K. E. Kreischer, I. Mastovsky, M. A. Shapiro, J. R. Sirigiri, and R. J. Temkin. Second harmonic operation at 460 GHz and broadband continuous frequency tuning of a gyrotron oscillator. *IEEE Transactions on Electron Devices*, 52(5):798–807, May 2005.

[26] S. Jawla, M. A. Shapiro, W. Guss, and R. J. Temkin. 527 GHz gyrotron for DNP-NMR spectroscopy. In *IVEC 2012*, pages 205–206, April 2012.

[27] D. E. M. Hoff, B. J. Albert, E. P. Saliba, F. J. Scott, E. J. Choi, M. Mardini, and A. B. Barnes. Frequency swept microwaves for hyperfine decoupling and time domain dynamic nuclear polarization. *Solid State Nuclear Magnetic Resonance*, 72:79 – 89, 2015. Honor Issue for Jake Schaefer.

[28] M. Blank, P. Borchard, S. Cauffman, K. Felch, M. Rosay, and L. Tometich. High-frequency CW gyrotrons for NMR/DNP applications. In *IVEC 2012*, pages 327–328, April 2012.

[29] Y. Matsuki, H. Takahashi, K. Ueda, T. Idehara, I. Ogawa, M. Toda, H. Akutsu, and T. Fujiwara. Dynamic nuclear polarization experiments at 14.1 T for solid-state NMR. *Phys. Chem. Chem. Phys.*, 12:5799–5803, 2010.

[30] E. A. Nanni, S. M. Lewis, M. A. Shapiro, R. G. Griffin, and R. J. Temkin. Photonic-band-gap traveling-wave gyrotron amplifier. *Phys. Rev. Lett.*, 111:235101, Dec 2013.

[31] A. Henstra, P. Dirksen, and W. T. Wenckebach. Enhanced dynamic nuclear polarization by the integrated solid effect. *Physics Letters A*, 134(2):134 – 136, 1988.

[32] T. V. Can, R. T. Weber, J. J. Walish, T. M. Swager, and R. G. Griffin. Ramped-amplitude novel. *The Journal of Chemical Physics*, 146(15):154204, 2017.

[33] V. Weis, M. Bennati, M. Rosay, and R. G. Griffin. Solid effect in the electron spin dressed state: A new approach for dynamic nuclear polarization. *The Journal of Chemical Physics*, 113(16):6795–6802, 2000.

[34] G. W. Morley, J. van Tol, A. Ardavan, K. Porfyrakis, J. Y. Zhang, and G. A. D. Briggs. Efficient dynamic nuclear polarization at high magnetic fields. *Phys. Rev. Lett.*, 98:220501, May 2007.

[35] N. Khaneja. Switched control of electron nuclear spin systems. *Phys. Rev. A*, 76:032326, Sep 2007.

[36] T. V. Can, R. T. Weber, J. J. Walish, and T. M. Swager. Frequency-swept integrated solid effect. *Angewandte Chemie International Edition*, 56(24):6744–6748, 2017.

[37] T. V. Can, J. J. Walish, T. M. Swager, and R. G. Griffin. Time domain DNP with the NOVEL sequence. *The Journal of Chemical Physics*, 143(5):054201, 2015.

[38] N. Bloembergen and P. P. Sorokin. Nuclear magnetic resonance in the cesium halides. *Phys. Rev.*, 110:865–875, May 1958.

[39] T.V. Can, Q.Z. Ni, and R.G. Griffin. Mechanisms of dynamic nuclear polarization in insulating solids. *Journal of Magnetic Resonance*, 253:23 – 35, 2015. Special Issue: Recent Achievements and New Directions in Biomolecular Solid State NMR.

[40] A. Henstra, P. Dirksen, J. Schmidt, and W. Th. Wenckebach. Nuclear spin orientation via electron spin locking (NOVEL). *Journal of Magnetic Resonance*, 77(2):389 – 393, 1988.

[41] V. L. Granatstein, R. K. Parker, and C. M. Armstrong. Vacuum electronics at the dawn of the twenty-first century. *Proceedings of the IEEE*, 87(5):702–716, May 1999.

[42] R. Q. Twiss. Radiation transfer and the possibility of negative absorption in radio astronomy. *Australian Journal of Physics*, 11:564–579, 1958.

[43] Schneider. Stimulated emission of radiation by relativistic electrons in a magnetic field. *Phys. Rev. Lett.*, 2:504–505, Jun 1959.

[44] A. V. Gaponov. *Izv. VUZ. Radiofizika*, 2:450–462, 1959.

[45] J. M. Baird and W. Lawson. Magnetron injection gun (MIG) design for gyrotron applications. *International Journal of Electronics*, 61(6):953–967, 1986.

[46] L. M. Field. Some slow-wave structures for traveling-wave tubes. *Proceedings of the IRE*, 37(1):34–40, Jan 1949.

[47] R. J. Temkin and K. E. Kreischer. High power gyrotrons. *MRS Proceedings*, 347, 1994.

[48] K. E. Kreischer, B. G. Danly, J. B. Schutkeker, and R. J. Temkin. The design of megawatt gyrotrons. *IEEE Transactions on Plasma Science*, 13(6):364–373, Dec 1985.

[49] T. A. Spencer, C. E. Davis, K. J. Hendricks, F. J. Agee, and R. M. Gilgenbach. Results from gyrotron backward wave oscillator experiments utilizing a high-current high-voltage annular electron beam. *IEEE Transactions on Plasma Science*, 24(3):630–635, Jun 1996.

[50] K. Felch, M. Blank, P. Borchard, T. S. Chu, J. Feinstein, H. R. Jory, J. A. Lorbeck, C. M. Loring, Y. M. Mizuhara, J. M. Neilson, R. Schumacher, and R. J. Temkin. Long-pulse and CW tests of a 110-GHz gyrotron with an internal,

quasi-optical converter. *IEEE Transactions on Plasma Science*, 24(3):558–569, Jun 1996.

[51] J. M. Neilson and P. Borchard. Design of an internal coupler to corrugated waveguide for high power gyrotrons. In *2010 IEEE International Vacuum Electronics Conference (IVEC)*, pages 315–316, May 2010.

[52] N. I. Zaytsev, T. B. Pankratova, M. I. Petelin, and V. A. Flyagin. Millimeter and submillimeter-wave gyrotrons. *Radio Eng. Electron. Phys.*, 19(5):103-107, 1974.

[53] R. J. Temkin, K. E. Kreischer, W. J. Mulligan, S. MacCabe, and H. R. Fetterman. A 100 kW, 140 GHz pulsed gyrotron. *International Journal of Infrared and Millimeter Waves*, 3(4):427–437, Jul 1982.

[54] Y. Yamaguchi, T. Saito, Y. Tatematsu, S. Ikeuchi, V. N. Manuilov, J. Kasa, M. Kotera, T. Idehara, S. Kubo, and T. Shimozuma. High-power pulsed gyrotron for 300 GHz-band collective thomson scattering diagnostics in the Large Helical Device. *Nuclear Fusion*, 55(1):013002, 2015.

[55] K. E. Kreischer, J. B. Schutkeker, B. G. Danly, W. J. Mulligan, and R. J. Temkin. High efficiency operation of a 140 GHz pulsed gyrotron. *International Journal of Electronics*, 57(6):835–850, 1984.

[56] N. I. Zaitsev, N. A. Zavolsky, V. E. Zapevalov, E. V. Ilyakov, I. S. Kulagin, V. K. Lygin, M. A. Moiseev, V. E. Nechaev, M. I. Petelin, and R. M. Rozenthal. Ten-megawatt pulsed gyrotron with a 1-cm wavelength and a 50% efficiency. *Radiophysics and Quantum Electronics*, 46(10):816–819, Oct 2003.

[57] R. J. Temkin, K. Kreischer, S. M. Wolfe, D. R. Cohn, and B. Lax. High frequency gyrotrons and their application to tokamak plasma heating. *Journal of Magnetism and Magnetic Materials*, 11(1):368 – 371, 1979.

[58] A. A. Bogdashov, A. V. Chirkov, G. G. Denisov, A. N. Kuftin, V. K. Lygin, M. A. Moiseev, and V. E. Zapevalov. Development of the step tunable 140/110 GHz 1 MW gyrotron for fusion. In *25th International Conference on Infrared and Millimeter Waves*, pages 21–22, Sept 2000.

[59] D. S. Tax, B. Y. Rock, B. J. Fox, S. K. Jawla, S. C. Schaub, M. A. Shapiro, R. J. Temkin, and R. J. Vernon. Experimental results for a pulsed 110/124.5-GHz megawatt gyrotron. *IEEE Transactions on Plasma Science*, 42(5):1128–1134, May 2014.

[60] K. Kajiwara, Y. Oda, A. Kasugai, K. Takahashi, and K. Sakamoto. Development of dual-frequency gyrotron with triode magnetron injection gun. *Applied Physics Express*, 4(12):126001, 2011.

[61] M. Thumm. Progress on gyrotrons for ITER and future thermonuclear fusion reactors. *IEEE Transactions on Plasma Science*, 39(4):971–979, April 2011.

[62] L. R. Barnett, J. M. Baird, Y. Y. Lau, K. R. Chu, and V. L. Granatstein. A high gain single stage gyrotron traveling-wave amplifier. In *1980 International Electron Devices Meeting*, volume 26, pages 314–317, 1980.

[63] R. S. Symons, H. R. Jory, S. J. Hegji, and P. E. Ferguson. An experimental gyro-TWT. *IEEE Transactions on Microwave Theory and Techniques*, 29(3):181–184, Mar 1981.

[64] D. S. Furuno, D. B. McDermott, C. S. Kou, N. C. Luhmann, Jr., and P. Vitello. Theoretical and experimental investigation of a high-harmonic gyro-traveling-wave-tube amplifier. *Phys. Rev. Lett.*, 62:1314–1317, Mar 1989.

[65] L. R. Barnett, W. C. Tsai, H. L. Hsu, N. C. Luhmann, C. C. Chiu, K. F. Pao, and K. R. Chu. 140 kw w-band TE01 ultra high gain gyro-TWT amplifier. In *2006 IEEE International Vacuum Electronics Conference held Jointly with 2006 IEEE International Vacuum Electron Sources*, pages 461–462, 2006.

[66] K. R. Chu, H. Y. Chen, C. L. Hung, T. H. Chang, L. R. Barnett, S. H. Chen, and T. T. Yang. Ultrahigh Gain Gyrotron Traveling Wave Amplifier. *Physical Review Letters*, 81:4760–4763, November 1998.

[67] G. G. Denisov, V. L. Bratman, A. D. R. Phelps, and S. V. Samsonov. Gyro-TWT with a helical operating waveguide: new possibilities to enhance efficiency and frequency bandwidth. *IEEE Transactions on Plasma Science*, 26(3):508–518, Jun 1998.

[68] M. Thottappan, S. Singh, and P. K. Jain. Gyro-TWT using a metal PBG waveguide as its RF circuit - Part I: Analysis and design. *IEEE Transactions on Electron Devices*, 63(5):2118–2124, May 2016.

[69] K. R. Chu, L. R. Barnett, H. Y. Chen, S. H. Chen, Ch. Wang, Y. S. Yeh, Y. C. Tsai, T. T. Yang, and T. Y. Dawn. Stabilization of absolute instabilities in the gyrotron traveling wave amplifier. *Phys. Rev. Lett.*, 74:1103–1106, Feb 1995.

[70] M. Garven, J. P. Calame, B. G. Danly, K. T. Nguyen, B. Levush, F. N. Wood, and D. E. Pershing. A gyrotron-traveling-wave tube amplifier experiment with a ceramic loaded interaction region. *IEEE Transactions on Plasma Science*, 30(3):885–893, Jun 2002.

[71] M. Blank, P. Borchard, S. Cauffman, and K. Felch. Development and demonstration of a broadband W-band gyro-TWT amplifier. In *2005 Joint 30th International Conference on Infrared and Millimeter Waves and 13th International Conference on Terahertz Electronics*, volume 2, pages 652–653, Sept 2005.

[72] J. P. Calame, M. Garven, B. G. Danly, B. Levush, and K. T. Nguyen. Gyrotron-traveling wave-tube circuits based on lossy ceramics. *IEEE Transactions on Electron Devices*, 49(8):1469–1477, Aug 2002.

[73] J. Y. Choe, H. S. Uhm, and S. Ahn. Analysis of the wide band gyrotron amplifier in a dielectric loaded waveguide. *Journal of Applied Physics*, 52(7):4508–4516, 1981.

[74] H. S. Uhm and J. Y. Choe. Gyrotron amplifier in a helix loaded waveguide. *Physics of Fluids*, 26(11):3418–3425, 1983.

[75] W. Hu, M. A. Shapiro, K. E. Kreischer, and R. J. Temkin. 140-GHz gyrotron experiments based on a confocal cavity. *IEEE Transactions on Plasma Science*, 26(3):366–374, Jun 1998.

[76] K. R. Chu, H. Y. Chen, C. L. Hung, T. H. Chang, L. R. Barnett, S. H. Chen, and T. T. Yang. Ultrahigh gain gyrotron traveling wave amplifier. *Phys. Rev. Lett.*, 81:4760–4763, Nov. 1998.

[77] K. R. Chu, H. Y. Chen, C. L. Hung, et al. Theory and experiment of ultrahigh-gain gyrotron traveling wave amplifier. *IEEE Transactions on Plasma Science*, 27(2):391–404, April 1999.

[78] V. L. Bratman, G. G. Denisov, S. V. Samsonov, A. W. Cross, A. D. R. Phelps, and W. Xe. High-efficiency wideband gyro-TWTs and gyro-BWOs with helically corrugated waveguides. *Radiophysics and Quantum Electronics*, 50(2):95–107, 2007.

[79] Y. Yang, S. Yu, T. Z. Zhang, Y. Zhang, and Q. Zhao. Study of beam-wave interaction in a 170-GHz confocal gyrotron traveling-wave tube. *IEEE Transactions on Plasma Science*, 43(3):791–795, March 2015.

[80] Y. Yang, S. Yu, Y. Liu, T. Zhang, Y. Zhang, and Q. Zhao. Efficiency enhancement of a 170 GHz confocal gyrotron traveling wave tube. *Journal of Fusion Energy*, 34(4):721–726, 2015.

[81] G. S. Nusinovich, S. Chainani, and V. L. Granatstein. Effect of the transverse nonuniformity of the radiofrequency field on the start current and efficiency of gyrodevices with confocal mirrors. *Physics of Plasmas*, 15, 103106, 2008.

[82] W. Fu, X. Guan, Xiaotong, and Y. Yan. High harmonic terahertz confocal gyrotron with nonuniform electron beam. *Physics of Plasmas*, 23, 013301, 2016.

[83] H. A. Haus. *Waves and Fields in Optoelectronics*. CBLS, 2004.

[84] L. A. Weinstein. *Open Resonators and Open Waveguides*. Boulder, CO: The Golem Press, 1969.

[85] T. Nakahara and N. Kurauchi. Guided beam waves between parallel concave reflectors. *IEEE Transactions on Microwave Theory and Techniques*, 15(2):66–71, Feb. 1967.

[86] G. Goubau and F. Schwering. On the guided propagation of electromagnetic wave beams. *IRE Transactions on Antennas and Propagation*, 9(3):248–256, May 1961.

[87] C. D. Joye, M. A. Shapiro, J. R. Sirigiri, and R. J. Temkin. Demonstration of a 140-GHz 1-kW confocal gyro-traveling-wave amplifier. *IEEE Transactions on Electron Devices*, 56(5):818–827, May 2009.

[88] J. A. Stratton, P. M. Morse, J. D. C. Little, and F. J. Corbató. *Spheroidal Wave Functions, Including Tables of Separation Constants and Coefficients*. New York: Wiley, 1956.

[89] G. S. Nusinovich and H. Li. Theory of gyro-travelling-wave tubes at cyclotron harmonics. *International Journal of Electronics*, 72(5-6):895–907, 1992.

[90] M. Botton, T. M. Antonsen, B. Levush, K. T. Nguyen, and A. N. Vlasov. MAGY: a time-dependent code for simulation of slow and fast microwave sources. *IEEE Transactions on Plasma Science*, 26(3):882–892, June 1998.

[91] O. V. Sinitsyn, G. S. Nusinovich, K. T. Nguyen, and V. L. Granatstein. Nonlinear theory of the gyro-TWT: Comparison of analytical method and numerical code data for the NRL gyro-TWT. *IEEE Transactions on Plasma Science*, 30(3):915–921, June 2002.

[92] G. S. Nusinovich and H. Li. Large-signal theory of gyro traveling wave tubes at cyclotron harmonics. *IEEE Transactions on Plasma Science*, 20(3):170–175, June 1992.

[93] S. E. Tsimring. Gyrotron electron beams: Velocity and energy spread and beam instabilities. *International Journal of Infrared and Millimeter Waves*, 22(10):1433–1468, Oct 2001.

[94] E. G. Avdoshin, L. V. Nikolaev, I. N. Platonov, S. E. Tsimring. Experimental investigation of the velocity spread in helical electron beams. *Radiophysics and Quantum Electronics*, 16(4):461–466, Apr 1973.

[95] S. E. Tsimring. On the spread of velocities in helical electron beams. *Radiophysics and Quantum Electronics*, 15:952–961, 1972.

[96] N. A. Zavolsky, V. E. Zapevalov, M. A. Moiseev. Influence of the energy and velocity spread in the electron beam on the starting conditions and efficiency of a gyrotron. *Radiophysics and Quantum Electronics*, 49(2):108–119, Feb 2006.

[97] J. Petillo, K. Eppley, D. Panago, E. Nelson, N. Dionne, J. DeFord, B. Held, L. Chemyakova, X. Zhai, K. Nguyen, and B. Levush. Applications of the michelle 2D/3D electron gun and collector code. In *IEEE Conference Record - Abstracts. 2005 IEEE International Conference on Plasma Science*, pages 267–267, June 2005.

[98] J. M. Baird and W. Lawson. Magnetron injection gun (MIG) design for gyrotron applications. *International Journal of Electronics*, 61(6):953–967, 1986.

[99] J. P. Anderson, S. E. Korbly, R. J. Temkin, M. A. Shapiro, K. L. Felch, and S. Cauffman. Design and emission uniformity studies of a 1.5-mw gyrotron electron gun. *IEEE Transactions on Plasma Science*, 30(6):2117–2123, Dec 2002.

[100] S. N. Vlasov, L. I. Zagryadskaya, and M. I. Petelin. Transformation of a whispering gallery mode, propagating in a circular waveguide, into a beam of waves. *Radiotekhnika i Elektronika*, 20:2026–2030, October 1975.